ELASTO-VISCOPLASTIC CONSTITUTIVE MODELING FOR CLAY AND DEFORMATION ANALYSIS OF SOFT CLAY FOUNDATION

By

Mamoru Mimura

April 1991

ELASTO-VISCOPLASTIC CONSTITUTIVE MODELING FOR CLAY AND DEFORMATION ANALYSIS OF SOFT CLAY FOUNDATION

By

Mamoru Mimura

April 1991

TABLE OF CONTENTS

PART 2

NUMERICAL INVESTIGATION ON STRESS-DEFORMATION CHARACTERISTICS OF SOFT CLAY FOUNDATION

Elasto-Viscoplastic Constitutive Modeling for Clay and Deformation Analysis of Soft Clay Foundation

by

Mamoru Mimura

Summary

The material properties are characterized by its stress-strain time behavior. In soil mechanics or geotechnical engineering, we must deal with the rate-sensitive, non-elastic materials with dilatancy. In order to describe these complicated behavior of geotechnical materials mathematically, elasto-viscoplastic constitutive equations have been proposed and studied. In Part 1 of this dissertation, the theoretical structure of the elasto-viscoplastic constitutive equations are investigated in detail. Discussion will be focused on the description of undrained creep rupture by the viscid-type constitutive models. Two different elasto-viscoplastic constitutive models are exemplified, that is the overstress model and the non-stationary flow surface model. The intrinsic structures of the constitutive equations are clearly reflected on the calculated performance. First of all, the problems, that the overstress model cannot describe the undrained creep rupture, will be overcome. After proving mathematically why it cannot describe the undrained creep rupture, the model is improved by introducing the effect of deterioration of clay structure, or the concept of the non-stationary flow surface. Secondly, the stress rate effect will be discussed. The difference in the structures of the above mentioned two type models exist on this point. The effect of the stress rate term is, however, little on the calculated performances, because the overstress term, that both models commonly have, is much more influential.

Detailed discussion on the theoretical structure of the constitutive equations is a matter of great academic interest to be sure, but, we should pay attention to the fact that the practical geotechnical events are

usually managed under K_0 condition. In Part 2, various geotechnical problems of clay foundations will be numerically investigated by the elasto-viscoplastic finite element analysis. The constitutive model used in Part 2, the capability of evaluation of the initial stress at rest, in terms of K_0, had been much improved, comparing with the previous models. Firstly, Assessment of lateral ground movement will be discussed. A new index, soil volume ratio, is proposed. Then, it is shown that the quantitative evaluation of lateral ground movement can be performed, with a due consideration of the local geological condition. Secondly, deformation analysis of the marine foundation will be performed, subjected to reclamation or breakwater construction. Emphasis is placed on the following factors for numerical analysis; the exact modeling of the foundation geometry, reasonable determination of the parameters for the materials and the exact modeling of construction sequence. The calculated performance will accurately estimate the *in situ* ground deformation and excess pore water pressure generation-dissipation process when these three factors could be satisfied. The validity of the elasto-viscoplastic algorithm stated in this dissertation is confirmed from a strong support of the comparison with the monitored performances.

ACKNOWLEDGEMENTS

This research was initiated when the author was a master's student of the Faculty of Engineering of Kyoto University.

Author would like to express his sincere gratitude to Professor Toru Shibata, supervisor, Department of Civil Engineering, Kyoto University, for his insightful guidance and continuous encouragement throughout the course of this research.

Grateful acknowledgements are also extended to Professor Toshihisa Adachi, Department of Transportation Engineering, Kyoto University, for guiding the author in the field of 'constitutive laws for geotechnical materials', and a large portion of Part 1 of this dissertation were due to his critical advice and useful discussions.

Author is particularly indebted to Associate Professor Hideo Sekiguchi, Disaster Prevention Research Institute, Kyoto University, for his critical and insightful discussions, especially, the deformation analysis in terms of the elasto-viscoplastic finite element method. I sincerely express my gratitude to him for his extensive support.

Thanks are also extended to Professor Fusao Oka, Department of Civil Engineering, Gifu University for his significant advice and helpful discussions.

I learned many things, academic and non-academic, from Associate Professor, Masayoshi Shimizu, Department of Civil Engineering, Tottori University and Associate Professor Atsushi Yashima, Department of Civil Engineering, Gifu University. These Professors were my seniors in Kyoto University. I appreciate their useful suggestions and critical discussions.

My sincere appreciation is extended to Associate Professor Tej Bhakta Singh Pradhan, Department of Civil Engineering, Yokohama National University; Mr. Ikuo Sano, Lecturer, Department of Civil Engineering, Osaka Industrial University; Dr. Kazuyoshi Tateyama, Lecturer, Department of Civil Engineering, Kyoto University; Dr. Atsushi Iizuka, Lecturer, Department of Civil Engineering, Kanazawa University and; Mr. Makoto Kimura, Instructor, Department of Transportation Engineering, Kyoto University. Earnest discussions with them on various problems in Soil Mechanics led to a better understanding and helped the author in the

development of various parts of this dissertation. I attribute this dissertation to their continuous support.

Thanks are also extended to Mr. Hiroki Shimizu, Technical Officer of the Disaster Prevention Research Institute, Kyoto University, for his cooperation in experimental work and drawing up the diagrams.

During the course of this research, many people contributed in many different ways, either as researchers or students, while at Kyoto University. It is difficult to name all of them, however, few names stand out, Shinya Nakano (Mie Prefecture Government Office), Satoshi Nakajima (Hazama Co. Ltd.), San-Hyon No (Foreign Student from Korea), Tetsuji Kubo (Hokuriku Electric Power Co. Ltd.), Tsutomu Namikawa (Takenaka Co. Ltd.), Katsuji Sumikura (Suntory Co. Ltd.), Akiyoshi Azechi (Fukazawa Co. Ltd.), Hirohisa Yamaguchi, Mitsuo Nozu (Fudo Construction Co. Ltd.), and staff of Hanshin Expressway Public Corporation and National Research Institute of Fisheries Engineering, Fisheries Agency.

Author would like to thanks Abhay Kumar Shrivastava, doctoral candidate, Department of Civil Engineering, Kyoto University, for proofreading part of this dissertation.

Last, but not least, I would like to express my sincere gratitude to my wife, Yuko, who has given me continuous support in-and out of my academic activities. Without her understanding, and devoted encouragement, this monumental work would not have taken the present shape. Finally, I would like to thanks my parents for their continuous support and belief.

CHAPTER 1

Introduction

1-1. General Description

Soil mechanics and geotechnical engineering are significantly entrusted with an important role that quantitative evaluation and prediction should be performed for various geotechnical problems. Attention must be paid to the fact that comparing with other materials, the physical response of a geotechnical material is more influenced by the way of loading, the rate of loading and the history of loading, because of the intrinsic characteristics of soils, that is, isotropic compression, dilatancy or mobilization of frictional shear resistance. Therefore, deformation characteristics of soils are clearly distinguished from those of metals, polymers and so forth. In order to describe these complicated deformation characteristics of the geotechnical materials mathematically, various constitutive equations (stress-strain relations) have been proposed since 1950's. These constitutive equations for the geotechnical materials are discussed in the framework of continuum mechanics, assuming that soil is a continuum although it is true soil is fundamentally a granular material.

For continuum mechanics, we have the general physical laws to describe deformation and flow of a continuum body, namely, conservation of mass and conservation of momentum that a continuum body must implicitly follow. The relations derived from the physical laws stated above are called *'field equations'*.

The mass contained in a domain V at a time t is expressed as follows:

$$m = \int_v \rho \, dV \tag{1-1}$$

where $\rho = \rho(x,t)$ is the density of the continuum at the location x at time t. Conservation of mass requires that $Dm/Dt=0$. After a little calculation, we obtain the following form of the law of conservation of mass that is equivalent to the *equation of continuity* in continuum mechanics.

$$\frac{\partial \rho}{\partial t} + \frac{\partial}{\partial x_j}(\rho v_j) = 0 \tag{1-2}$$

Here, x_j denotes a Cartesian coodinate and v_j represents a velocity vector component.

Then, Newton's laws of motion state that in an inertial frame of reference the material rate of change of linear momentum of a body is equal to resultant of applied forces, that are defined by the sum of surface traction and body force per unit volume. From this equilibrium of linear momentum, we obtain the celebrated *Eulerian equation of motion* of a continuum as follows :

$$\rho \frac{\partial v_j}{\partial t} = \frac{\partial \sigma_{ij}}{\partial x_j} + F_i \tag{1-3}$$

Here, s_{ij} denotes stress tensor, F_i is body force component. In *Eq.(1-3)*, by setting all verosity components v_i equal to zero, we can obtain the the equation of static equilibrium.

Application of the law of balabce of angular momentum to the particular case of static equilibrium leads to that stress tensors are symmetric tensors as shown below :

$$\sigma_{ij} = \sigma_{ji} \tag{1-4}$$

Deformation of a continuum body is governed by the *Eq. (1-2), (1-3) and (1-4)* stated above. We have thirteen unknowns to be derived, that is, the density, r, three componebts of verosity, v_j (equivalent to those of displacement, u_i) and nine components of stress, σ_{ij}. By considering the stress symmetry, $\sigma_{ij}=\sigma_{ji}$, the unkowns for stress are reduced to six

independent components. Since we have four field equations as shown by *Eq.(1-2)* and *Eq.(1-3)* for ten independent unknowns, more six equations are needed to determine deformation of a continuum body. Constitutive equations are the equations governing stress strain relations of a material uniquely with six components of stress and strain. Therfore, deformation of a continuum body is completely prescribed by the field equations and constitutive equations.

In Part 1 of the dissertation, the theoretical structures of the constitutive equations are investigated in detail. Discussion will be focused on the elasto-viscoplastic models which can describe the rate-sensitive behaviors such as the strain-rate dependency of strength, secondary compresasion, creep and stress relaxation, as well as the plastic behavior with dilatancy. The calculated performances of the constitutive models are compared with the laboratory experimantal results, that is, undrained triaxial compression tests with the constant rate of strain or undrained creep tests with the constant sustained load. Based on these data, accuracy of the predicted performances by the constitutive models is critically discussed. Then, the theoretical structures of the elasto-viscoplastic models are explained, in conjunction with their effect on the calculated performance. The modified overstress elasto-viscoplastic constitutive model is proposed by introducing the stress-state dependency of the viscoplastic parameter in order to describe the acceleration creep and creep rupture phenomena. Furthermore, the rate sensitive behavior of clay mass is investigated, in terms of elasto-viscoplastic finite element method. Applicability of the constitutive models to the actual geotechnical problems will be discussed, with a detailed investigation of stress-strain characteristics of clay elements and water migration effect in the clay foundation.

1-2. Previous Studies on Constitutive Models for Clay

In this section, critical review will be done for the previous studies on the constitutive models for clay.

1-2-1. Rate-Dependent Models

Murayama and Shibata (1956) proposed '*rheological model*' based on the rate-process theory, which is the leading study in the field of constitutive equations for viscid soil materials. Christensen and Wu (1964) also proposed another rheological model, and the validity of the model has been confirmed by creep and stress relaxation tests performed. Singh and Mitchell (1968), Shibata and Karube (1969) showed empirical equations governing the creep characteristics of clay. Murayama *et al.* (1971) showed an empirical equation describing the reduction of stress during stress relaxation process.

1-2-2. Inviscid Models (Critical State Energy Theory)

Roscoe *et al.* (1963), Roscoe and Poorooshasb (1963) proposed Cam clay model for remoulded normally consolidated clay based on Drucker's postulate (1960) assuming that clay is a work-hardening elasto-plastic body. The model has been derived by introducing the concept of '*critical state*' where shear deformation takes place without any volumetric variation and the assumption for equilibrium of energy dissipation (critical state energy theory). Burland (1965), Roscoe and Burland (1968) proposed modified Cam clay model with the different assumption for energy dissipation. Critical state energy theory (Cambridge model) has been significant reference for following studies on constitutive equations.

1-2-3. Development after 1970's

Akai *et al.* (1975) experimentally showed the existence of unique stress - strain - time relation based on the assumption that clay is a rate-sensitive elasto-viscoplastic material with dilatancy. Adachi and Okano (1974) proposed an elasto-viscoplastic constitutive model based on the critical state energy theory and the theory of viscoplasticity presented by Perzyna (1963). By taking this model into account, Adachi and Oka (1982) proposed an elasto-viscoplastic constitutive model on the basis of the rate dependency of shear stress. Sekiguchi (1977) proposed an elasto-viscoplastic constitutive model based on the concept of non-stationary flow

surface. These elasto-viscoplastic constitutive models can describe the rate-sensitive properties of clay, such as the rate dependency of shear stress, creep, secondary compression and stress relaxation. Pender (1977) proposed an elasto-plastic constitutive model for overconsolidated clay by assuming a plastic potential function and a yield function separately, and stress strain relation is governed by non-associated flow rule for the model. After extended to describe cyclic behavior (1977), the final version has been developed to describe whole behavior of normally consolidated clay as well as overconsolidated clay. Mroz *et al.* (1978 (a), (b)) proposed an elasto-plastic constitutive model based on the concept of *'field of work-hardening moduli"* (Mroz, 1967). The model is so-called two-surface model, the original multi-surface model. Consolidation surface and yield surface are separately defined, and hardening rule is prescribed by controlling the transition of the yield surface mathematically. Development of the aforementioned studies on constitutive equations were summarized in the state-of-the-art report (JSSMFE, 1985).

1-3. Scope of the Study

In chapter 2, the calculated performances of the existing five constitutive models are compared with the experimental results for undrained shear under the condition of the constant rate of strain. The selected models are the Cam clay model, the modified Cam clay model, Pender model, Adachi and Oka model and Sekiguchi model. The former three are the inviscid models and the latter two are the viscoplastic models. Descriptive accuracy of these models is also discussed in this chapter.

Chapter 3 deals with the investigation of the theoretical structures of the elasto-viscoplastic constitutive models. The traditional overstress model is mathematically proved that it does not describe the acceleration creep and the subsequent creep rupture due to its theoretical structures. Two trials are performed for the overstress model to describe the creep rupture. The first one is introduction of the stress state dependency of the viscoplastic parameter, based on the experimental findings for the undrained creep tests. Then, the modified model is proposed. The second

one is introduction of the concept of non-stationary flow surface. By ignoring the stress rate effect from the non-stationary flow surface model, the adapted overstress model is proved to be derived. It is proved that both derived overstress models can clearly describe the acceleration creep and creep rupture phenomena.

In chapter 4, the behavior of a rate-sensitive, saturated clay under strip loading is analyzed using the finite element method, with emphasis on assessing the rate effects on the bearing capacity of such a clay foundation. The potential undrained creep rupture of a clay mass is discussed, considering the shear stress reduction due to stress redistribution in the clay foundation, and it is also shown that the partial drainage occurring even in the loading stage exerts the profound effect on the mobilization of bearing capacity of the clay foundation.

In chapter 5, the major conclusions obtained from the present study have been summarized in items.

REFERENCES

(1) Adachi, T. and F. Oka (1982) : Constitutive Equations for Normally Consolidated Clay Based on Elasto-Plasticity, Soils and Foundations, Vol.22, No.4, pp.57-70.

(2) Adachi, T. and M. Okano (1974) : A Constitutive Equations for Normally Consolidated Clay, Soils and Foundations, Vol.14, No.4, pp.55-73.

(3) Akai, K., T. Adachi. and N. Ando (1975) : Existance of a Unique Stress-Strain-Time Relation of Clays, Soils and Foundations Vol.15, No.1, pp.1-16.

(4) Burland, J.B. (1965) : The Yielding and Dilation of Clay, Correspondance, Geotechnique, Vol.15, pp.211-214.

(5) Christensen, R.W. and T.H. Wu (1964) : Analysis of Clay Deformation as a Rate Process, Proc. ASCE. Vol.90, No.SM6, pp.125-157.

(6) JSSMFE (1985) : Report of ISSMFE Subcomitte on Constitutive Laws of Soils and Proc. of Discussion Session 1A XI ICSMFE, San Fransisco.

(7) Ladd, C.C., Foott, R., Ishihara, K., Schlosser, F., and Poulos, H.G. (1977) : Stress-Deformation and Strength Characteristics, Proc. 9th ICSMFE Tokyo, Vol.2, pp.421-494.

(8) Lo, K.Y. (1969) : The Pore Pressure-Strain Relationship of Normally Consolidated Undisturbed Clays, Canadian Geotechnical Journal, Vol.6, pp.383-394.

(9) Mesri, G. and P.M. Godlewski (1977) : Time and Stress-Compressibility Interrelationship, Proc. ASCE, Vol.103, No.GT5, pp.417-430.

(10) Mroz, Z. (1967) : On the Description of Anisotropic Hardening Journal Mech. Phys. Solids, Vol.15, pp.163-175.

(11) Mroz, Z., V.A. Norris, and O.C. Zeinkiewicz (1978) : An Anisotropic Hardening Model for Soils and its Application to Cyclic Loading, International Journal, for Numerical and Analytical Methods in Geomechanics, Vol.2, pp.203-221.

(12) Mroz, Z., V.A. Norris, and O.C. Zienkiewicz (1979) : Application of an Anisotropic Hardening Model in the Analysis of Elasto-Plastic Deformation of Soils, Geotechnique, 29, No.1, pp.1-34.

(13) Naghdi, P.M. (1960) : Stress-Strain Relations in Plasticity and Thermoplasticity, Proc. 2nd Symp. on Naval Structural Mechanics, Pergamon Press, pp.121-169.

(14) Oka, F. (1979) : Constitutive Theory for Solid-Fluid Mixture and its Application to Stress Wave Propagation through Cohesive Soil, Proc. of JSCE, No.272, pp.117-130.

(15) Pender, M.J. (1977) : A Unified Model for Soil Stress-Strain Behavior, Proc. Speciality Session 9, 9th ICSMFE, pp.213-222.

(16) Pender, M.J. (1977) : Modelling Soil Behavior under Cyclic Loading, Proc. 9th ICSMFE, Vol.2, pp.325-331.

(17) Pender, M.J. : A Model for the Behavior of Overconsolidated Soil Geotechnique, Vol.28, No.1, pp.1-25.

(18) Perzyna, P (1963) : The Constitutive Equations for Workhardening and Rate Sensitive Plastic Materials, Proc. of Vibrational Problems, Warsaw, Vol.4, No.3, pp.281-290.

(19) Roscoe, K.H., A.N. Schofield. and C.P. Wroth (1958) : On the Yielding of Soils, Geotechnique, Vol.8, pp.22-53.

(20) Roscoe, K.H., A.N. Schofield. and A. Thurairajah (1963) : Yielding of Clays in States Wetter than Critical, Geotechnique, Vol.13, No.3, pp.211-240.

(21) Roscoe, K.H. and H.B. Poorooshasb (1963) : A Theoretical and Experimental Study of Strains in Triaxial Compression Test on Normally Consolidated Clays, Geotechnique, Vol.13, pp.12-38.

(22) Roscoe, K.H. and J.B. Burland (1968) : On the Generalized Stress-Strain Behavior of Wet Clay, Engineering Plasticity Cambridge Univ. Press, pp.535-609.

(23) Schofield, A.N. and C.P. Wroth (1968) : Critical State Soil Mechanics., McGraw-Hill.

(24) Sekiguchi, H (1977) : Rheological Characteristics of Clays, Proc. 9th ICSMFE Tokyo, Vol.2, pp.289-292.

(25) Sekiguchi, H. and M. Toriihara (1976) : Theory of One-Dimensional Consolidation of Clays with Consideration of their Rheological Properties, Soils and Foundations, Vol.16, No.1, pp.27-44.

(26) Singh, A. and J.K. Mitchell (1968) : General Stress-Strain-Time Function for Soils, Proc. ASCE. Vol.94, No.SM1, pp.21-46.

(27) Skempton, A.N. (1954) : The Pore Pressure Coefficients A and B, Geotechnique, Vol.4, pp.143-147.

(28) Shibata, T. and D. Karube (1969) : Creep Rate and Creep Strength of Clay, Proc. 7th ICSMFE. Vol.1, pp.361-367.

CHAPTER 2

Effects of Strain Rate on Undrained Stress-strain Behavior of a Normally Consolidated Clay

2-1. Introduction

Various constitutive models have been proposed to describe the mechanical behavior of clays. Roscoe et al.(1963), Roscoe and Schofield (1963) proposed a constitutive model called Cam clay model. In their derivation of the model, a dissipative energy equation was postulated based on the critical state concept. Burland (1965), and Roscoe and Burland (1968) proposed the modified Cam clay model from another estimation of the dissipative energy. The associated flow rule was used in the derivation of above two models.

Because clays are regarded as strain-hardening plastic, rate-sensitive materials with dilatancy, the constitutive model must be able to describe behavior produced by those properties. Adachi and Okano (1974) extended Cam clay model to explain time-dependent behavior of normally consolidated clay by using Perzyna's viscoplastic theory (1963). They assumed that clays reached their static equilibrium state at the end of primary consolidation. According to the experimental findings, however, normally consolidated clay never reaches the static equilibrium state at the end of primary consolidation. Taking into account these results, Oka (1981) and Adachi and Oka (1982) generalized Adachi and Okano model so that it could explain not only dynamic behavior such as creep, stress relaxation and strain rate effect of shear strength but secondary consolidation as well. On the other hand, Sekiguchi (1977) proposed an elasto-viscoplastic model for normally consolidated clay based on the theory of non-stationary flow surface (Olszak and Perzyna, 1961).

Pender (1977) proposed an elasto-plastic model for overconsolidated clay in the basis of Cam clay model, while using the non-associated flow

rule. After then, he extended his model so that it can describe not only the behavior under monotonic loading but also those under cyclic loading of normally consolidated as well as overconsolidated clay.

It is very important to show clearly how a constitutive model can describe the behavior of soils accurately, however, the evaluation of model has been usually so vague as pointing out only the resemblance between the calculated stress-strain curves and the experimental results. In this chapter, we selected the five existing models, *i.e.*, Cam clay model, modified Cam clay model, Pender model, Adachi & Oka model and Sekiguchi model, and examine their descriptive accuracy for soil behavior in comparison of calculated and experimental results. For the purpose, standard oedometer tests and undrained triaxial compression tests under different shear strain rates were conducted. For simplicity, however, the discussion is limited to the behavior of isotropically consolidated clay under monotonic loading condition.

2-2. Models and Parameters

2-2-1. Cam Clay Model

Roscoe *et al.* (1963) postulated a relation of external energy dissipation and internal energy dissipation. The external energy dissipation is defined as follows:

$$dW_{ex} = \sigma_{ij}\, d\varepsilon_{ij}^{p} = \sigma_{m}'\, dv^{p} + s_{ij}\, de_{ij}^{p} \tag{2-1}$$

in which, σ_{ij} is the stress tensor, $d\varepsilon_{ij}^{p}$ is the plastic strain increment, σ_{m}' is the mean effective stress, s_{ij} is the deviatoric stress tensor, dv^{p} is the plastic volumetric strain increment and de_{ij}^{p} is the plastic deviatoric stress increment. The internal energy dissipation was assumed to be given as

$$dW_{in} = M^{*}\, \sigma_{m}'\, d\sqrt{2I_{2}^{p}} \tag{2-2}$$

in which, M^* is the stress $\sqrt{2J_2}/\sigma'_m$ at critical state, $J_2 = s_{ij}\, s_{ij}/2$ is the second invariant of deviatoric stress and $I_2^p = e_{ij}\, e_{ij}/2$ is the second invariant of plastic deviatoric strain. From *Eqs.(2-1)* and *(2-2)*, the next relation is obtained.

$$dv^p/d\sqrt{2I_2^p} = M^* - \sqrt{2J_2}/\sigma'_m \tag{2-3}$$

Assuming that the yield function is independent of both of the third invariant of stress and strain, the normality rule is expressed by

$$dv^p/d\sqrt{2I_2^p} = -\sqrt{2J_2}/d\sigma'_m \tag{2-4}$$

From *Eqs.(2-3)* and *(2-4)*, the next differential equation is given.

$$d\sqrt{2J_2}/d\sigma'_m - \sqrt{2J_2}/\sigma'_m + M^* = 0 \tag{2-5}$$

Integrating this equation, the yielding function is obtained as follows:

$$f = \sigma'_m \, exp\, [\sqrt{2J_2}/M^*\sigma'_m] = \sigma'_{my} \tag{2-6}$$

Applying this yield function to the associated flow rule gives the following stress-strain relations

$$d\varepsilon_{ij}^p = \frac{\lambda - \kappa}{M^*(1 + e_0)} \left[\frac{d\sqrt{2J_2}}{M^*\sigma'_m - \sqrt{2J_2}} + \frac{d\sigma'_m}{\sigma'_m}\right] \cdot \left[s_{ij}/\sqrt{2J_2} + (M^* - \sqrt{2J_2}/\sigma'_m)\, \delta_{ij}/3\right] \tag{2-7}$$

in which, e_0 is the initial void ratio, Cc is the compression index, Cs is the swelling index. To complete this constitutive model, four parameters, e_0, Cc, Cs and $M^*$are necessary to be given.

2-2-2. Modeified Cam Clay Model

Burland (1965) and Burland and Roscoe (1968) proposed a modified Cam clay model based on another estimation of energy dissipation. The

internal energy dissipation was defined for the isotropic consolidation process as follows:

$$dW_{in} = \sigma_m' \, dv^p \tag{2-8}$$

while for shear process, it was assumed to be by

$$dW_{in} = M^* \, \sigma_m' \, de_{ij}^p \tag{2-9}$$

Generally, the internal energy dissipation was postulated in the following equation.

$$dW_{in} = \sigma_m' \sqrt{(dv^p)^2 + (M^* \, de_{ij}^p)^2} \tag{2-10}$$

In the same way as Cam clay model, the stress-strain relation is obtained as follows:

$$d\varepsilon_{ij}^p = \frac{\lambda - \kappa}{1 + e_0} \left[\frac{s_{ij} s_{ij}/M^{*2} - (\sigma_m' - \sigma_{my}'/2) \, d\sigma_m'}{(\sigma_m' - \sigma_{my}'/2) \, \sigma_{my}'^2} \right] \cdot \left[s_{ij}/M^{*2} - (\sigma_m' - \sigma_{my}'/2) \, \sigma_{my}'^2 \, \delta_{ij}/3 \right] \tag{2-11}$$

in which σ_{my}' is the preconsolidation pressure. The modified Cam clay model has also four material parameters as well as Cam clay model, *i.e.*, e_0, Cc, Cs and M^*. These parameters are easily obtained from standard oedometer and undrained triaxial compression tests.

2-2-3. Pender Model

Pender (1977) extended Cam clay model based on the non-associated flow rule so that it can describe the behavior not only of overconsolidated but also of normally consolidated clay. Assuming that plastic yielding occurs only when the stress ratio changes, the yield was defined as follows:

$$f = \sqrt{2J_2} - \eta_i \cdot \sigma_m' \tag{2-12}$$

in which, η_i is the initial value of stress ratio, $\sqrt{2J_2}/\sigma'_m$. He assumed that the plastic potential function was given by a relation of plastic strain increment ratio and stress ratio, and the undrained effective stress path was parabolic shape. On the basis of above mentioned assumptions, the stress-strain relation was obtained. In addition to the material parameters of Cam clay model, this model needs a parameter p_{cs} (a mean effective stress measure at the critical state). He originally assumed that the value of p_{cs} was a function of the initial void ratio, e_0.

2-2-4. Adachi and Oka Model

Adachi and Oka (1982) proposed the following constitutive model for normally consolidated clay by extending Cam clay model to explain the time dependent behavior based on the theory of elasto-viscoplasticity (Perzyna,1963).

$$\dot{\varepsilon}_{ij} = \frac{\dot{s}_{ij}}{2G} + \frac{\kappa}{1+e_0}\frac{\dot{\sigma}'_m}{\sigma'_m}\delta_{ij} + \frac{1}{M^*\sigma'_m}\Phi(F)\frac{s_{ij}}{\sqrt{2J_2}} + \frac{1}{3M^*\sigma'_m}\Phi(F)\cdot\left[M^* - \frac{\sqrt{2J_2}}{\sigma'_m}\right]\delta_{ij} \tag{2-13}$$

$$\Phi(F) = c_0 \cdot exp\left[m' \ln\left(\sigma'_{my}/\sigma'^{(s)}_{my}\right)\right] \tag{2-14}$$

in which, G is the elastic shear modulus, $\sigma_{my}{}'^{(s)}$ is the strain hardening parameter and c_0 and m' are the material constants relating to the time-dependent properties of clay. There are eight parameters in the model *i.e.*, Cc, Cs, e_0, M, G, c_0, m' and $\sigma_{my}{}'^{(s)}$. Of these, $\sigma_{my}{}'^{(s)}$ is determined by Cc, Cs and $\sigma_{myi}{}'^{(s)}$ which is the the initial value of $\sigma_{my}{}'^{(s)}$.

In addition to Cc, Cs, e_0 and M, four parameters, G, c_0, m' and $\sigma_{myi}{}'^{(s)}$, are required to determine. G can be determined from triaxial compression tests. In the case of axisymmetric triaxial compression, the next relation is obtained from the model by taking into account the difference of two strain rates, $\dot{\varepsilon}_{11}^{(1)}$ and $\dot{\varepsilon}_{11}^{(2)}$.

$$ln\left\{\frac{\dot{\varepsilon}_{11}^{(1)}}{\dot{\varepsilon}_{11}^{(2)}}\right\} = \frac{m'}{M}\left[\frac{q^{(1)}}{\sigma_m'} - \frac{q^{(2)}}{\sigma_m'}\right] \tag{2-15}$$

Here, $q^{(1)}$ and $q^{(2)}$ denote the deviatoric stress, $\sigma_1' - \sigma_3'$ for the corresponding strain rate, $\dot{\varepsilon}_{11}^{(1)}$ and $\dot{\varepsilon}_{11}^{(2)}$. *Fig. 1* is an experimental result to evaluate *Eq.(2-15)* and shows that a linear relation between the logarithm of strain rate, $\dot{\varepsilon}_{11}$ and stress ratio $(\sigma_1 - \sigma_3) / \sigma_m'$ is valid as an equi-mean effective stress line. The parameter m' can be determined from the slope of straight lines, provided M value is given. To determine the remaining parameters c_0 and $\sigma_{myi}'^{(s)}$, the following relation are used.

$$\dot{\varepsilon}_{11} = \frac{2}{3} exp\left[m'\left\{\frac{q}{M\,\sigma_m'} - \frac{\lambda(1+e_0)}{\kappa(\lambda-\kappa)}v^p\right\}\right] \tag{2-16}$$

$$C = \frac{c_0}{M^*\,\sigma_m'} exp\left[-m'\,ln\left(\frac{\sigma_{myi}'^{(s)}}{\sigma_{me}'}\right)\right] \tag{2-17}$$

Namely, it is sufficient to know the parameter, C instead of obtaining individual values of c_0 and $\sigma_{myi}'^{(s)}$. The all parameters for the constitutive model can be determined from the results of consolidation, swelling and strain-rate controlled undrained triaxial compression tests.

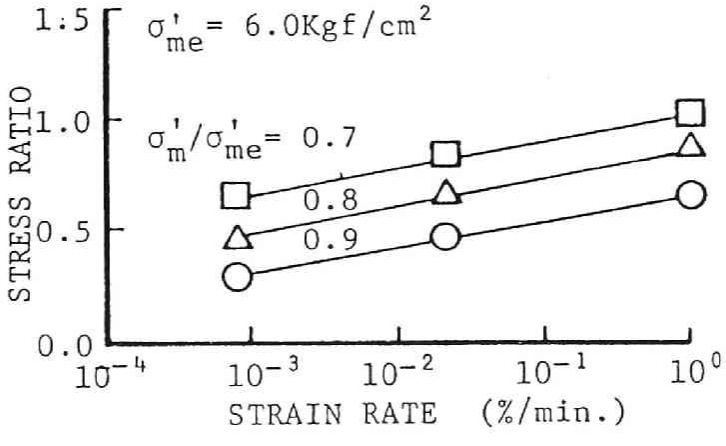

Fig. 1 Relation between Stress Ratio and Logarithm of Strain Rate

2-2-5. Sekiguchi Model

Sekiguchi (1977) proposed an elasto-viscoplastic constitutive model which can describe the rheological behavior of normally consolidated clay by estimating the volumetric strain due to mean effective stress, dilatancy and secondary compression. The viscoplastic flow rule for the model is generally expressed as follows:

$$\dot{\varepsilon}_{ij}^{p} = \Lambda \frac{\partial F}{\partial \sigma_{ij}'} \tag{2-18}$$

in which, F is the viscoplastic potential, Λ is the proportional constant. The viscoplastic potential, F is defined as follows:

$$F = \alpha \cdot \ln \left[1 + \frac{\dot{v}_0 \cdot t}{\alpha} \exp\left(\frac{f}{\alpha}\right)\right] = v^p \tag{2-19}$$

in which α is a secondary compression index, $\dot{v}_0$ is a reference volumetric strain rate, t is the elapsed time and v^p represents viscoplastic volumetric strain. f is a scalar function of p and q expressed as follows :

$$f = \frac{\lambda - \kappa}{1 + e_0} ln \left(\frac{p}{p_0}\right) + D \left(\frac{q}{p} - \frac{q_0}{p_0}\right) \tag{2-20}$$

here, D is the coefficient of dilatancy originally proposed by Shibata (1963).

2-3. Undrained Triaxial Compression Tests under the Condition of Constant Rate of Strain

To evaluate the five constitutive models, a series of undrained triaxial compression tests was conducted by using undisturbed Osaka alluvial clay. To determine the parameters, Cc and Cs, consolidation-swelling tests were conducted with an everyday loading, while to obtain the secondary compression index, α, consolidation test was carried out with an interval loading of one week. The obtained void ratio, e and logarithm of

of pressure, p curves are given in *Fig. 2* and the axial displacement - elapsed time curves are shown in *Fig. 3*. From these figures, Cc, Cs and α

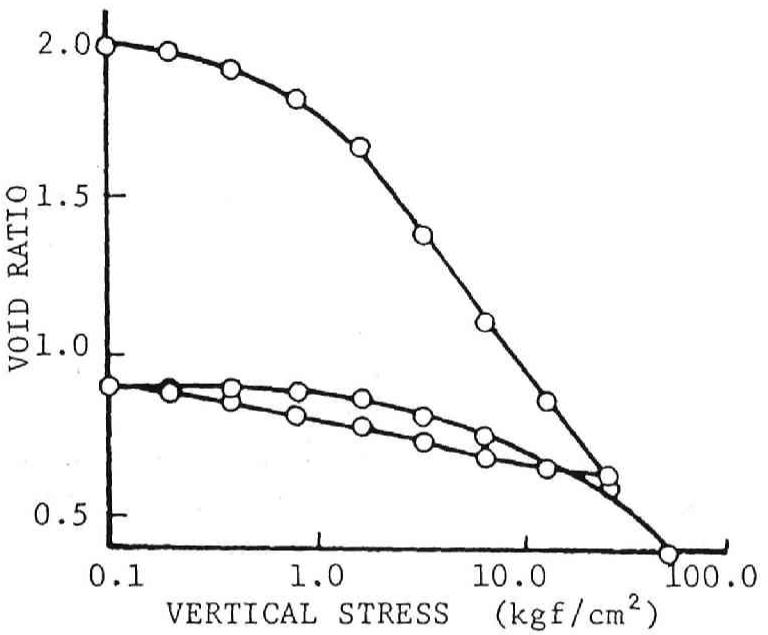

Fig. 2 Consolidation and Swelling Test Result (Oedometer)

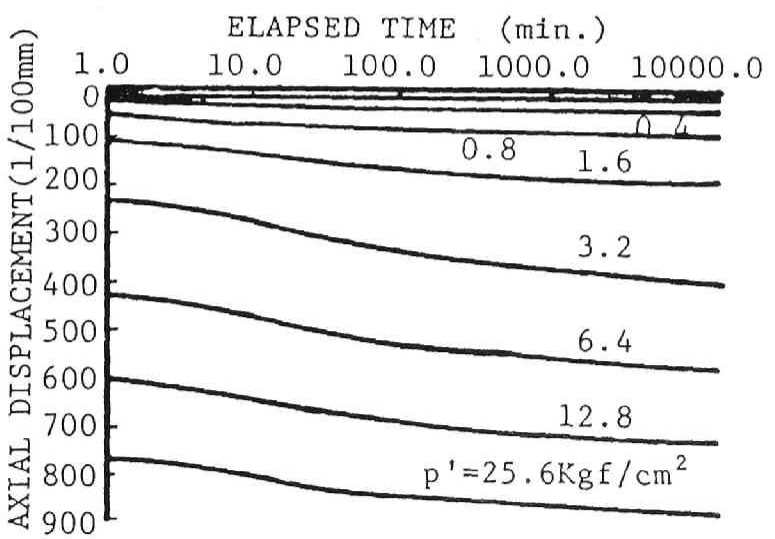

Fig. 3 Axial Strain with Time (Oedometer)

were determined. To determine the remaining parameters, G, M, p_{cs}, m' and C, another series of tests, *i.e.*, undrained constant strain rate compression tests were conducted under three different constant strain rate of 1.0, 2.1 x 10^{-2} and 7.8 x 10^{-4} %/min.

The obtained stress-strain curves, pore pressure - strain curves and effective stress paths are given in *Figs. 4, 5,* and *6*. From these test results, remarkable time-dependent behavior of clay can be seen. The elastic shear modulus G was determined by the slope of initial portion of stress-strain curve in *Fig. 4*. It does not so much depend on the strain rate, but strongly on the confining pressure. The stress ratio at critical state, M was obtained from the results in *Fig. 6*. The parameter, p_{cs} of Pender model was determined as the value of mean effective stress at the critical state, which was given by using the test results with the smallest strain rate of 7.8 x 10^{-4} %/min.. The parameters relating to time-dependent properties of clay, m' and C were determined from *Fig. 1*. The material parameters determined are listed in *Table-1*.

Table-1 Material Properties of Osaka Alluvial Clay

Cc	Cs	M	D	e_0
0.856	0.124	1.28	0.109	1.28
α	$\dot{v}_0$	G	m'	C
0.0044	3.5×10^{-6}	132.1	21.5	4.5×10^{-8}

Obtained from the result of
σ'_{me} = 6.0 kgf/cm^2

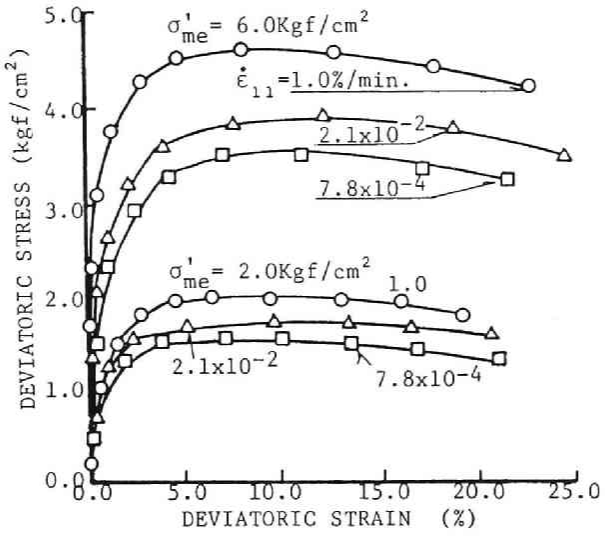

Fig. 4 Experimental Results of Stress-Strain Relations

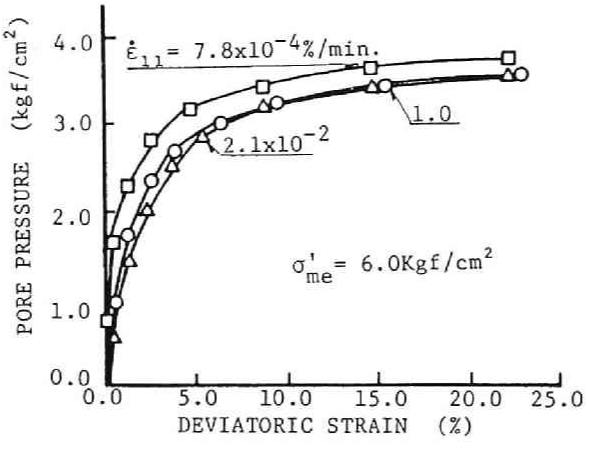

Fig. 5 Experimental Results of Excess Pore Water Pressure Generation with Strain

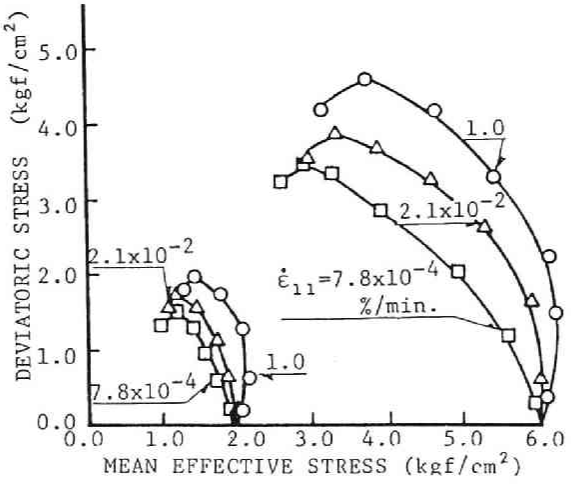

Fig. 6 Experimental Results of Effective Stress Paths

2-4. Evaluation of Performances by the Constitutive Model

Calculated curves, *i.e.*, the stress-strain, pore pressure-strain and effective stress paths, for Cam clay model, modified Cam clay model, Pender model are given by comparing with the experimental results with the smallest strain rate of 7.8 x 10^{-4} %/min. in *Fig. 7*. Because the deformation of clay shows such remarkable time-dependent behavior, in general, it is natural that these elasto-inviscid plastic models cannot describe the time-dependent behavior of clay. Here, we assume that the behavior under the strain rate of 7.8 x 10^{-4} %/min. is almost equivalent to that for static equilibrium. Comparing the calculated performance with experimental results performed in the strain rate of 7.8 x 10^{-4} %/min., the modified Cam clay model may not be suitable for the undrained behavior of clay. While Pender model is superior to describe the behavior than Cam clay model or modified Cam clay model. This is because Pender model was derived based on the non-associated flow rule and having one more parameter, p_{cs} in addition to those of other two models.

As already mentioned, an elasto-inviscid plastic model cannot describe the time-dependent behavior of clay. Clay shows, however, remarkable time-dependent behavior even under undrained condition. The calculated curves derived by the elasto-viscoplastic constitutive model, Adachi and Oka model and Sekiguchi model are shown *Figs. 8* and *9* together with the experimental results. Both models can explain the time-dependent behavior of clay under undrained condition. As seen in *Eq.(2-15)* and *Fig. 1*, the parameters, m' and C can be determined by the undrained triaxial test results obtained by conducting under at least two different strain rates. The parameter m' was found to be independent of confining pressure as well as the viscoplastic parameter C.

As reference, the stress ratio q/σ_m' and strain relations are compared in *Fig. 10*. Pender model can well describe the experimental results conducted under the smallest strain rate of 7.8 x 10^{-4} %/min.

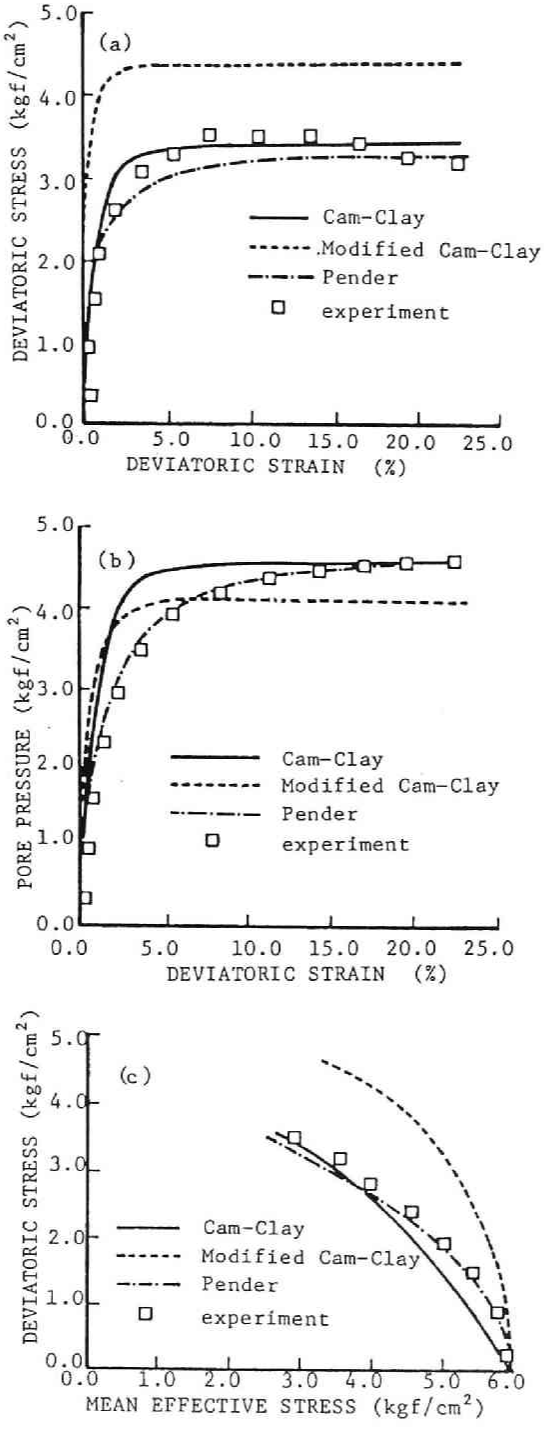

Fig. 7 Comparison of Calculated Performance by the Elasto-Plastic Models with the Experimental Results; (a) : Stress-Strain Relations, (b) : Excess Pore Water Pressure Generation, (c) : Effective Stress Path

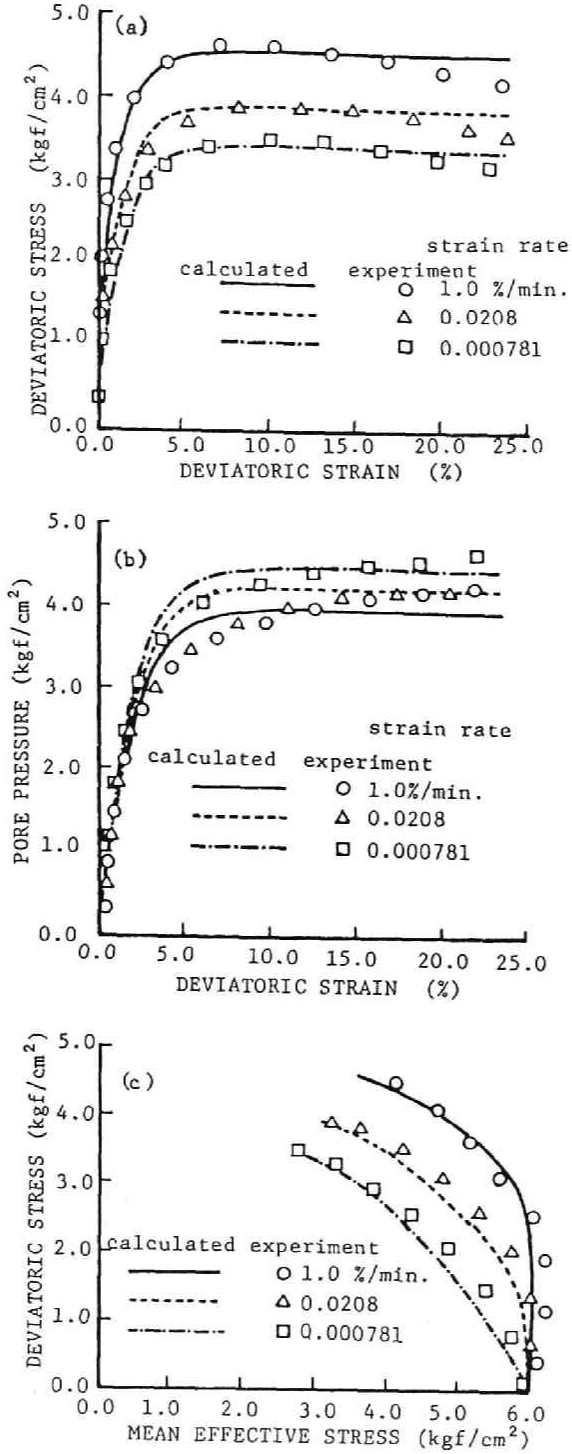

Fig. 8 Comparison of Calculated Performance by Adachi and Oka Model with the Experimental Results; (a) : Stress-Strain Relations, (b) : Excess Pore Water Pressure Generation, (c) : Effective Stress Path

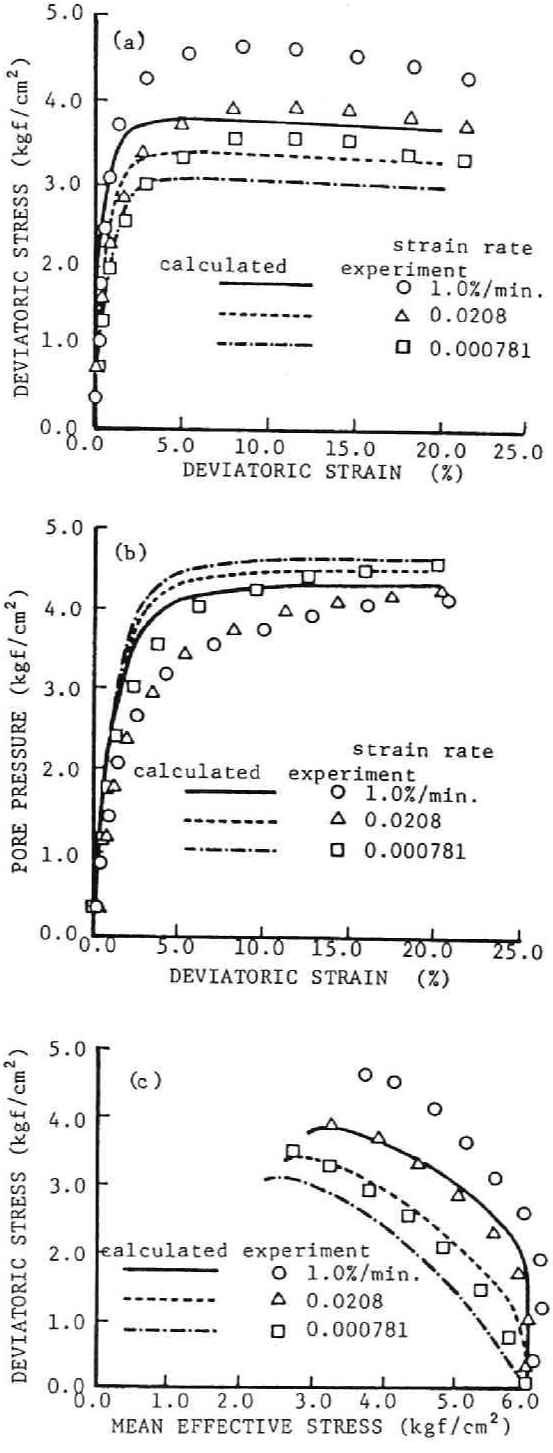

Fig.9 Comparison of Calculated Performance by Sekiguchi Model with the Experimental Results; (a) : Stress-Strain Relations, (b) : Excess Pore Water Pressure Generation, (c) : Effective Stress Path

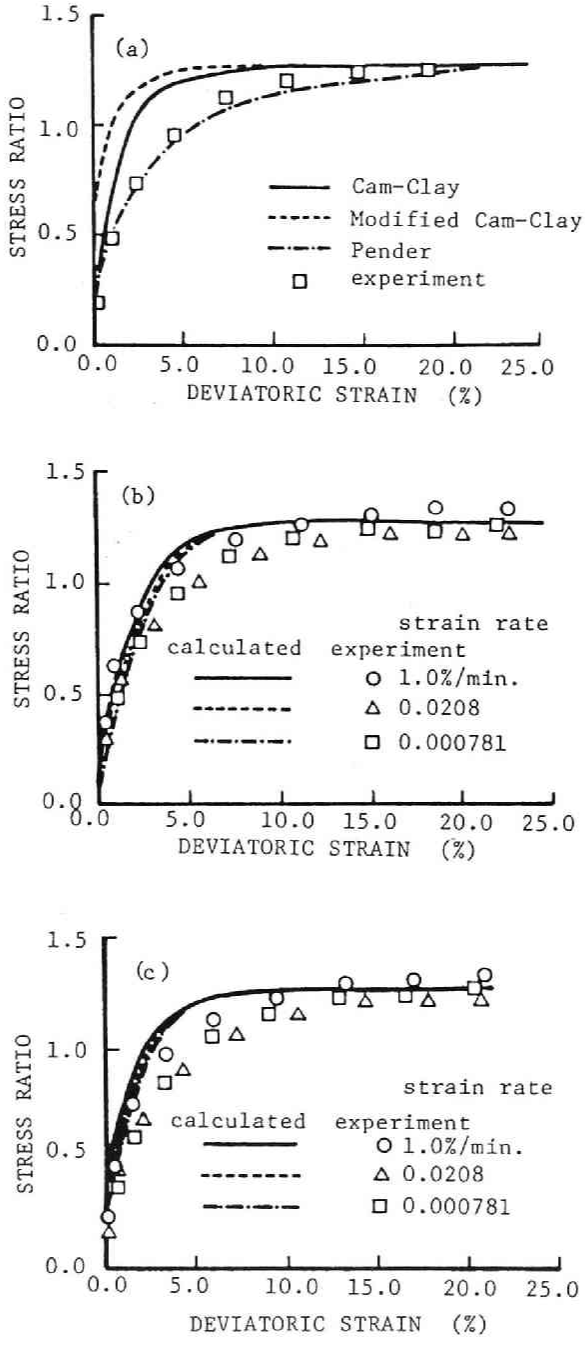

Fig. 10 Comparison of Calculated Performance with the Experimental Results for Stress Ratio - Strain Relations; (a) : Inviscid Models (b) : Adachi and Oka Model, (c) : Sekiguchi Model

To show the descriptive accuracy of the five constitutive models quantitatively, comparison between the calculated and experimental results was made in *Figs. 11* and *12*. Here, q_{cal} and q_{exp} denote the calculated and experimental deviatoric stress, u_{cal} and u_{exp} denote calculated and experimental excess pore water pressure respectively. As $(q_{cal} - q_{exp})/q_{exp}$ and $(u_{cal} - u_{exp})/u_{exp}$ represent the descriptive accuracy of constitutive models. Three elasto-plastic models overestimate the shear stress especially in the initial stage of shearing process, while the elasto-viscoplastic model, that is, Adachi and Oka model and Sekiguchi model can well describe the stress-strain behavior under undrained condition. On the other hand, no model can precisely describe the pore water pressure change especially in the initial stage of shearing.

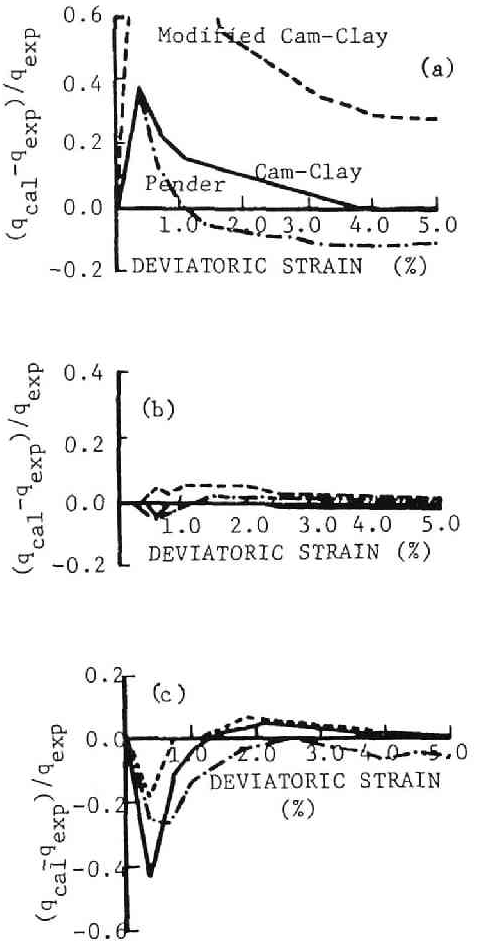

Fig. 11 Descriptive Accuracy of Stress-Strain Curves;
(a) : Inviscid Models, (b) : Adachi and Oka Model,
(c) : Sekiguchi Model

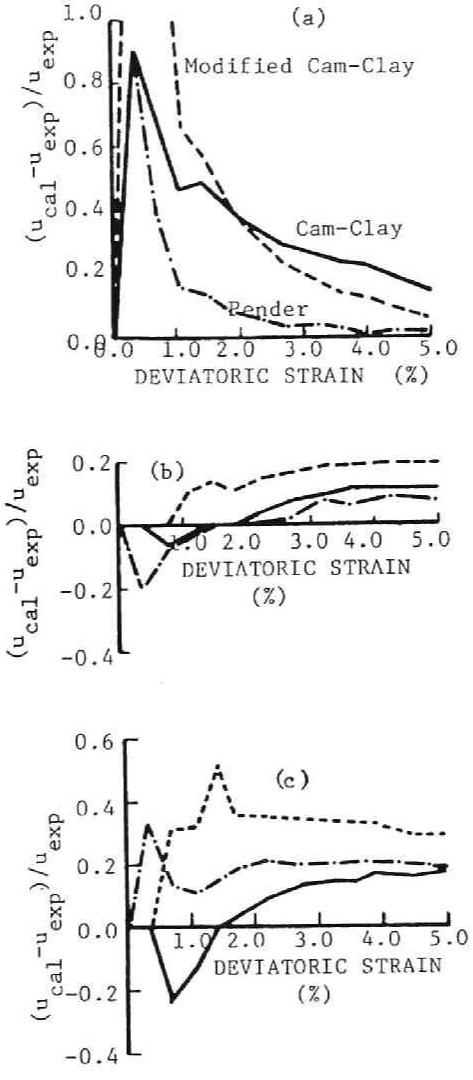

Fig. 12 Descriptive Accuracy of Excess Pore Water Pressure Generation Process; (a) : Inviscid Models, (b) : Adachi and Oka Model, (c) : Sekiguchi Model

2-5. Conclusions

Through this study, the following conclusions may be drawn.

(1) Undrained triaxial compression behavior of clay under the smallest strain rate of 7.8 x 10^{-4} %/min can be described by Cam clay model and Pender model to some extent.

(2) Modified Cam clay model overestimates the shear strength of this particular clay.

(3) Elasto-viscoplastic models can well describe the time-dependent behavior of normally consolidated clay.

(4) To evaluate the descriptive accuracy of each model quantitatively, new indices, *i.e.*, $(q_{cal}-q_{exp})/q_{exp}$ for stress-strain relation and $(u_{cal}-u_{exp})/u_{exp}$ for excess pore water pressure-strain relation were introduced. It makes clear that those constitutive models obtained on the basis of Cam clay model underestimate the deviatoric strain under undrained triaxial compression.

REFERENCES

(1) Adachi, T. and F. Oka (1982) : Constitutive Equations for Normally Consolidated Clay based on Elasto-viscoplasticity, Soils and Foundations, Vol.22, No.4, pp. 57-70.

(2) Adachi, T. and M. Okano (1974) : A Constitutive Equation for Normally Consolidated Clay, Soils and Foundations, Vol.14, No.4, pp. 55-73.

(3) Burland, J.B. (1965) : The Yielding and Dilation of Clay, Correspondence, Geotechnique, Vol.15, No.3, pp. 211-214.

(4) Oka, F. (1981) : Prediction of Time-dependent Behavior of Clay, Proc. 10th ICSMFE, Vol.1, pp. 215-218.

(5) Pender, M.J. (1977) : A Unified Model for Soil Stress-strain Behavior, Proc. Speciality Session 9, 9th ICSMFE, pp. 213-222.

(6) Perzyna, P. (1963) : The Constitutive Equations for Work Hardening and Rate Sensitive Plastic Materials, Proc. of Vibrational Problems, Warsaw, Vol.4, No.3, pp. 281-290.

(7) Roscoe, K.H. and J.B. Burland (1968) : On the Generalized Stress-strain Behavior of Wet Clay., Engineering Plasticity, Cambrigde University Press, pp. 535-609.

(8) Roscoe, K.H. and H.B. Poorooshasb (1963) : A Theoretical and Experimental Study of Strains in Triaxial Compression Test on Normally Consolidated Clays, Geotechnique, Vol.13, No.1, pp. 12-38.

(9) Roscoe, K.H., A.N. Schofield and A. Thurairajah (1963) : Yielding of Clays in States Wetter than Critical, Geotechnique, Vol.13, No.3, pp. 211-240.

(10) Sekiguchi, H. (1977) : Rheological Characteristics of Clays, Proc. 9th ICSNFE, Vol.2, pp. 289-292.

(11) Shibata, T. (1963) : On the Volume Changes of Normally - consolidated Clays, Annuals, Disaster Prevention Research Institute, Kyoto Univ., No. 6, pp.128-134 (in Japanese).

CHAPTER 3

Performance of Undrained Creep Rupture in Triaxial Compression

3-1. Introduction

Clay is a strain hardening, rate sensitive material that has remarkable characteristics such as rate sensitivity of strength, secondary compression, creep and stress relaxation. Various elasto-viscoplastic constitutive models have been proposed to describe the rheological behavior of clay. Murayama and Shibata (1956) proposed a rheology model based on the rate process theory, the leading study in this field. Adachi and Okano (1974) proposed an elasto-viscoplastic constitutive model that extends the critical state energy theory (Roscoe et al., 1958, Schofield et al., 1968). For this model, Perzyna's theory of an elasto-viscoplastic continuum (1963) was introduced to describe the rate sensitive behavior of normally consolidated clay. Adachi and Oka (1982) generalized Adachi and Okano model following the theory of Oka (1981), in which it is assumed that normally consolidated clay never reaches the static equilibrium state even at the end of primary consolidation. Sekiguchi (1977) proposed an elasto-viscoplastic constitutive model for normally consolidated clay based on a non-stationary flow surface. Viscoplastic potential has now been introduced so that this model can describe universally rate sensitive behavior of clay, such as creep rupture. Most elasto-viscoplastic constitutive models can be classified as overstress models or non-stationary flow surface models (Matsui et al., 1984). The Adachi and Okano model, Adachi and Oka model, Dafalias model (1982) and Katona model (1984) belong to the former, whereas, Sekiguchi model, Dragon and Mroz model (1979), Nova model (1982) and the Matsui and Abe model (1985) belong to the latter class.

Almost all the possible elasto-viscoplastic models for clay are thought to have been proposed. Recently, however, there has been strong indications that such models should be applied to the practical problems, conscious of their characteristics by clarifying the theoretical structure of

the models. Many researchers have pointed out that overstress models cannot describe the acceleration creep process nor the creep rupture of normally consolidated clay. Generally, in order to overcome this defect for creep description, the following trials can be thought. (1) introduction of structural deterioration effect and (2) Introduction of the non-stationary flow surface model.

In this chapter, we clarify the theoretical structures for the Adachi and Oka model, a typical overstress model, and discuss the effect of structural characteristics of the model on the performances of undrained creep rupture. In addition, we modified the overstress model by introducing the structural deterioration effect (trial (1)) so that it can describe the acceleration creep process and undrained creep rupture without changing the framework of the constitutive model. Furthermore, an adapted model introduced from the non-stationary flow surface model (trial (2)) will be discussed, with emphasis on the description of undrained creep rupture. Then, we will discuss the effect of the theoretical structures of models on the performance of undrained creep rupture in triaxial compression.

3-2. Theoretical Structure of the Elasto-Viscoplastic Model

3-2-1. General Remarks on the Adachi and Oka Model

The viscoplastic flow rule for an overstress type elasto-viscoplastic constitutive model is generally expressed as

$$\dot{\varepsilon}_{ij}^{p} = \gamma \cdot \Phi \left[f(\sigma_{ij}) - k(\varepsilon_{ij}^{p}) \right] \frac{\partial f}{\partial \sigma_{ij}} \tag{3-1}$$

in which, γ is the coefficient of viscosity, k the static hardening parameter, f the static yield function, ε_{ij}^{p} and $\dot{\varepsilon}_{ij}^{p}$ the viscoplastic strain and strain rate, and Φ the functional of overstress, $f(\sigma_{ij}) - k(\varepsilon_{ij}^{p})$. The functional Φ is monotonic increasing for overstress; $f(\sigma_{ij}) - k(\varepsilon_{ij}^{p})$. The Adachi and Oka

model being a typical overstress model, as shown by *Eq.(3-1)*, the stress strain relation is

$$\dot{\varepsilon}_{ij} = \dot{\varepsilon}_{ij}^{e} + \dot{\varepsilon}_{ij}^{p} = \frac{1}{2G}\dot{s}_{ij} + \frac{\kappa}{3(1+e_0)}\cdot\frac{\dot{\sigma}_m'}{\sigma_m'}\delta_{ij} + \frac{1}{M^*\sigma_m'}\cdot\Phi(F)\frac{s_{ij}}{\sqrt{2J_2}} + \frac{1}{3M^*\sigma_m'}\cdot\Phi(F)\left[M^* - \frac{\sqrt{2J_2}}{\sigma_m'}\right]\delta_{ij} \tag{3-2}$$

$$\Phi(F) = C\cdot M^*\cdot\sigma_m'\cdot exp\left[m'\left\{\frac{\sqrt{2J_2}}{M^*\sigma_m'} + ln\frac{\sigma_m'}{\sigma_{me}'} - \frac{1+e_0}{\lambda-\kappa}v^p\right\}\right]$$

Here, s_{ij} and $2J_2$ are the deviatoric stress tensor and the second invariant of deviatoric stress, δ_{ij} is Kronecker's delta, σ_m' the mean effective stress, σ_{me}' the mean effective stress at the end of consolidation, G the elastic shear modulus and M^* the effective stress ratio in the critical state. The superscripts, e and p denote the elastic and viscoplastic components. There are six parameters for this model: the compression and swelling (recompression) indices, λ and κ, the critical stress ratio, M^*, the elastic shear modulus, G, the parameter that estimates the secondary compression, m', and the viscoplastic parameter, C. The parameters λ, κ, M^* and G can be determined by empirical methods, by consolidation swelling tests and by strain rate-controlled undrained compression tests. Let us here determine m' and C. These parameters can be found from results of undrained triaxial compression tests for at least two different constant rates of strain. First, we determine m' from data on Osaka alluvial clay. Undrained triaxial compression tests were carried out in different constant rates of strain. The effective stress paths for these tests are shown in *Fig. 1*. Note the equi-mean effective stress, $p'=p^*$ given in the figure. The following relation is obtained from the constitutive model by taking into account the rate dependency of normally consolidated clay,

$$ln\left\{\frac{\dot{\varepsilon}_{11}^{(1)}}{\dot{\varepsilon}_{11}^{(2)}}\right\} = \frac{m'}{M}\left\{\frac{q^{(1)}}{p^*} - \frac{q^{(2)}}{p^*}\right\} \tag{3-3}$$

There is a valid linear relation in *Fig. 2* between the logarithm of the strain rate and the effective stress ratio as verified by *Eq.(3-3)*. The parameter m'

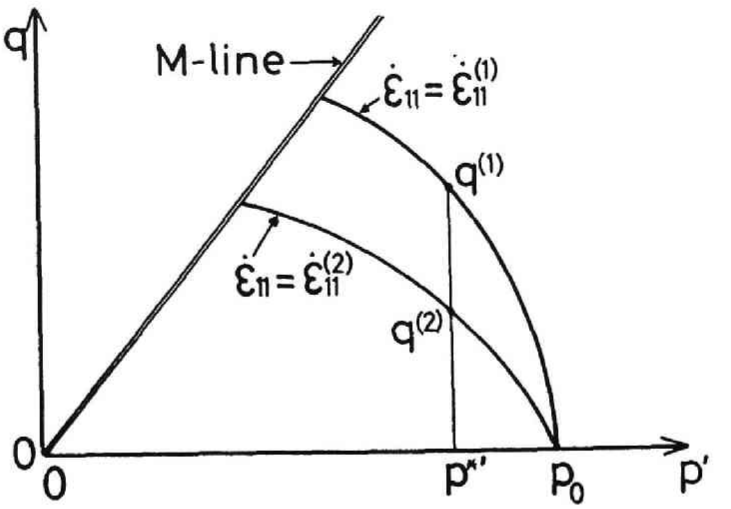

Fig. 1 Typical Effective Stress Paths for Normally Consolidated Clay under Undrained Condition

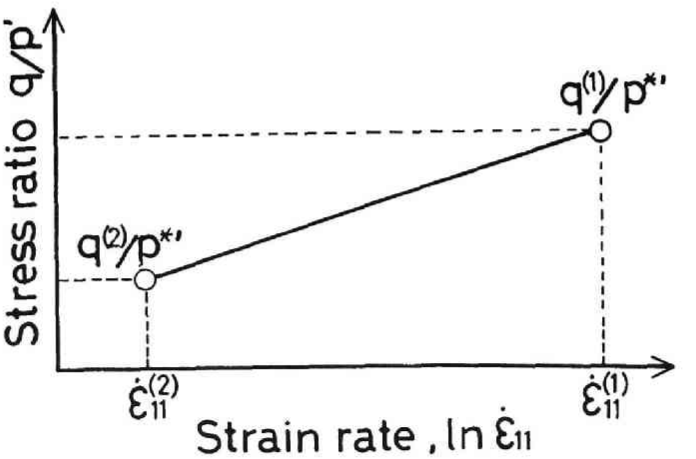

Fig. 2 Determination of the Viscoplastic Parameter, m'

can be determined from the slopes of the straight lines in this figure provided the $M(=(3/2)M^*)$ value is given.

Next, the determination of the viscoplastic parameter C. Originally, C has been introduced as

$$C = \frac{c_0}{M^* \sigma_m'} exp[-m' \ln \frac{\sigma_{myi}'^{(s)}}{\sigma_{me}'}] \tag{3-4}$$

in which, σ_{myi}' is the initial static hardening parameter and c_0 the material parameter, but, the static equilibrium state cannot be found experimentally. Because it is so difficult to identify the values of σ_{myi}' and c_0, knowledge of parameter C from the relation expressed by *Eq.(3-4)* explained later is sufficient. Thus, all the parameters can be determined from the experimental results.

3-2-2. Description of Undrained Creep by Adachi and Oka Model

Katona (1984), Oka (1985), Mimura and Sekiguchi (1985) have shown that because of its theoretical structure, the overstress type model cannot describe the acceleration creep process. We here prove this phenomenon mathematically.

Three characteristic phases, the primary, steady and acceleration creep phases appear in the undrained creep process (*Fig. 3*). At the same time, there are relations between the creep strain rate and the time elapsed shown schematically in *Fig. 4*. Clearly, when there is creep rupture, the creep strain rate, $\dot{\varepsilon}_{11}^p$, diverges to infinite just after its minimum stage. In other words, the condition necessary for the onset of acceleration creep is that there be a solution for the equation, $\ddot{\varepsilon}_{11}^p=0$, as has been pointed out by Sekiguchi (1984). The stress strain relation for the Adachi and Oka model is

$$\dot{\varepsilon}_{11}^p = \sqrt{\frac{2}{3}} C \cdot exp\ [m' \{\frac{q}{Mp'} + \frac{\lambda}{\lambda - \kappa} \ln \frac{p'}{p_0}\}] \tag{3-5}$$

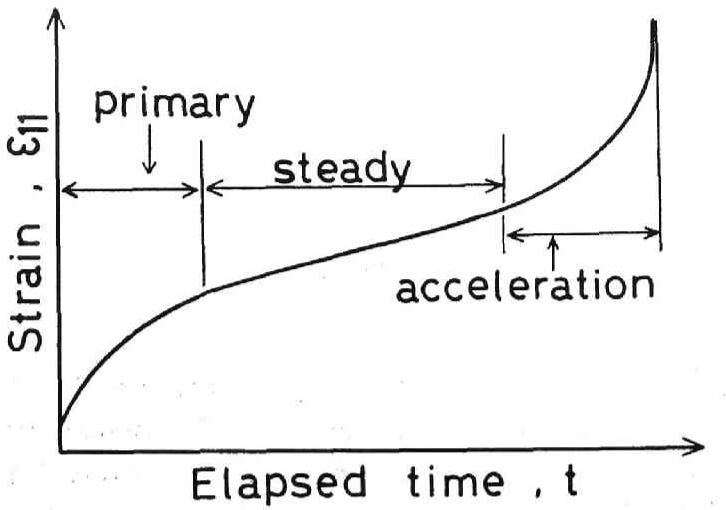

Fig. 3 Typical Creep Curves for Normally Consolidated Clay; Transient, Steady and Acceleration Creep Phases

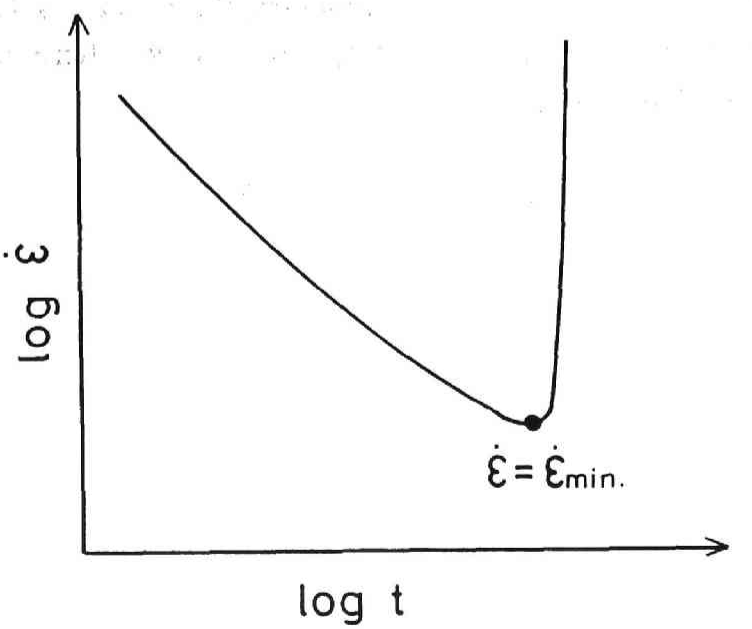

Fig. 4 Schematic Creep Strain Rate against the Elapsed Time for Undrained Creep

By differentiating *Eq.(3-5)* under the condition of undrained creep ; *q=constant,* the next relation can be derived.

$$\ddot{\varepsilon}_{11}^{p} = -\left(M - \frac{q}{p'} \right) \cdot \{\dot{\varepsilon}_{11}^{p}\}^2 \frac{m'(1 + e_0)}{(\lambda - \kappa)} \qquad (3\text{-}6)$$

Here, $\{\dot{\varepsilon}_{11}^{p}\}^2 > 0$, $m'(1+e_0)/(\lambda-\kappa)$ is the positive definite, therefore, the variation in $\ddot{\varepsilon}_{11}^{p}$ depend only on the value of $(M-q/p')$. Because $(M-q/p')$ is a monotonic decreasing, positive function through the shearing process, $\ddot{\varepsilon}_{11}^{p}$ is always negative and the condition for $\ddot{\varepsilon}_{11}^{p}=0$ is satisfied only at failure, $(q/p'=M)$. Thus, the Adachi and Oka model is proved to have the characteristics of the creep strain rate decreasing gradually in the undrained creep process that converges to a certain value at creep rupture. As many researchers have pointed out, this is mathematical proof that an overstress type elasto-viscoplastic constitutive model cannot describe the acceleration creep process.

3-3. Description of Creep Rupture by the Modified Model

Because the overstress type model cannot describe the undrained creep rupture phenomenon that follows the acceleration creep process, we have modified the constitutive model to describe undrained creep rupture, without changing the structure of the theoretical framework of the model.

3-3-1. Interrelation of Undrained Strength and the Viscoplastic Parameter

First, we introduce the theoretical solution for undrained strength, q_f and discuss the background for the modification of the constitutive model by clarifying the interrelation of the strain rate with the viscoplastic parameter. The following relation is derived from the basic equation for the model,

$$\dot{q} = 3G \left[\ddot{\varepsilon}_{11} - C \cdot \exp\left\{ m' \left(\frac{q}{Mp'} + \ln\frac{p'}{p_0} - \frac{1+e_0}{\lambda - \kappa} v^p \right) \right\} \sqrt{\frac{2}{3}} \right] \qquad (3\text{-}7)$$

Taking into account the undrained condition, $v^p = -v^e = -k / (1+e_0)$ $ln(p'/p_0)$ and $q=0$, $q=q_f=M\,p_f$ at failure, *Eq.(3-7)* can be expressed as

$$\dot{\varepsilon}_{11} = \sqrt{\frac{2}{3}}\, C \cdot exp\, [m'\{1 + ln\, \frac{q_f}{Mp_0}(1 + \frac{\lambda}{\lambda - \kappa})\}] \tag{3-8}$$

After some calculations, the next derived relation is

$$\frac{\dot{\varepsilon}_{11}}{\sqrt{2/3}\, C} = exp\, (m') \cdot [\frac{q_f}{Mp_0}]^{\frac{\lambda - \kappa}{m'\lambda}} \tag{3-9}$$

Therefore, the undrained strength, q_f can be introduced as

$$q_f = Mp_0\, [exp\{-(1 - \frac{\kappa}{\lambda})\}] \cdot [\frac{\dot{\varepsilon}_{11}}{\sqrt{2/3}C}]^{\frac{\lambda - \kappa}{m'\lambda}} \tag{3-10}$$

Because $M\,p_0\, \exp\{-(1-\kappa/\lambda)\}$ denotes the undrained strength for the Cam clay model in *Eq.(3-10)*, the undrained strength for the Adachi and Oka model depends on the strain rate as in the Cam clay model. q_f also being a monotonic function for the term $(\dot{\varepsilon}_{11}/\sqrt{2/3}C)$, there being such relations as $\lim \dot{\varepsilon}_{11} \to 0$, $q_f \to 0$ and $\lim \dot{\varepsilon}_{11} \to \infty$, $q_f \to \infty$ .The relation derived as the analytical solution (*Eq.(3-10)*) is shown in *Fig. 5* The material parameters used were determined for Osaka alluvial clay (Adachi *et al.*, 1985). Experimental data also are plotted in *Fig. 5* for comparison. Clearly, calculations made with the model predict the experimental data accurately.

As is evident from *Eq.(3-10)*, the effects of the strain rate, $\dot{\varepsilon}_{11}$, and the viscoplastic parameter, C, on the undrained strength, q_f, are equivalent, the increase in the strain rate corresponds to the decrease of the viscoplastic parameter, and the decrease in the strain rate is equivalent to the increase of viscoplastic parameter. Taking into account all the characteristics given above, the overstress type constitutive model can be modified to describe undrained creep rupture.

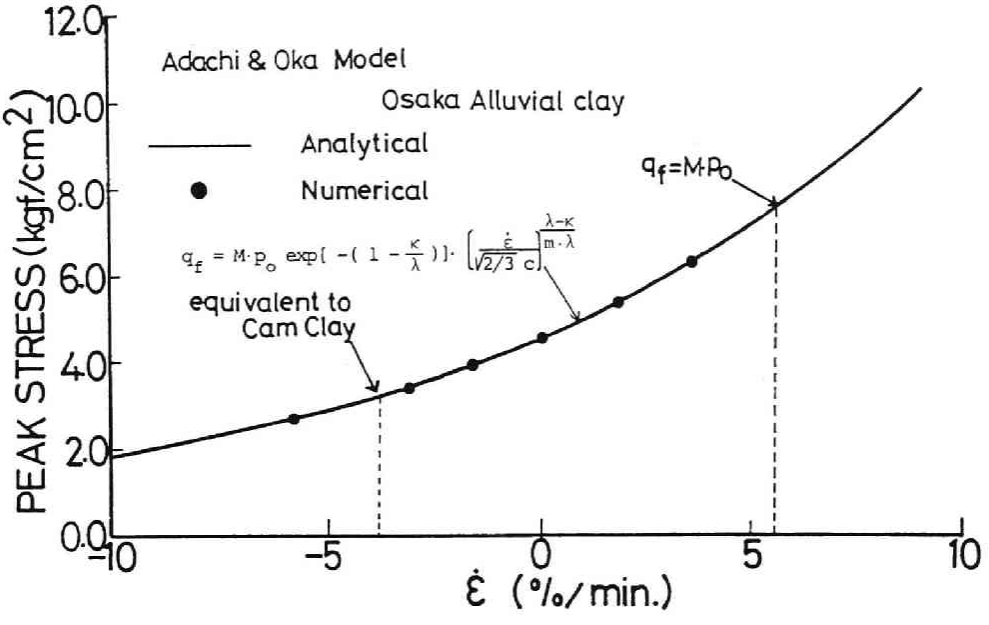

Fig. 5 Theoretical Solution of Undrained Strength for the Adachi and Oka Model

3-3-2. Variation in the Viscoplastic Parameter

As stated earlier, the Adachi and Oka model accurately predicts the undrained strength for shear under a constant rate of strain assuming that viscoplastic parameter C is constant. But because viscoplastic parameter C contains uncertain factors, closer consideration must be given for this parameter. We here discuss the variation in this viscoplastic parameter C during the undrained creep process, by comparing its values with those of the experimental results.

The strain rate varies under constant creep stress during the undrained creep process. A decrease in the mean effective stress caused by excess pore water pressure generation contributes decisively to the undrained creep rupture of normally consolidated clay. Therefore, we checked the relation between the strain rate, $\dot{\varepsilon}_{11}$, and the viscoplastic parameter, C, by estimating the effective stress state, $(M-q/p')$. Sekiguchi (1984) showed that undrained creep behavior, including the creep rupture

of normally consolidated clay, can be explained universally by the non-stationary flow surface type elasto-viscoplastic constitutive model he proposed. Therefore, the characteristics of viscoplastic parameter, C will be considered based on the experimental data for Umeda clay reported in reference (Sekiguchi, 1984).

A *lnC - (M-q/p')* relation for some creep stress levels is shown in *Fig. 6*. Whereas the value of viscoplastic parameter C increases slightly in the early stage of the undrained creep process, independent of the creep stress, as the critical state draws near, it increases explosively and diverges

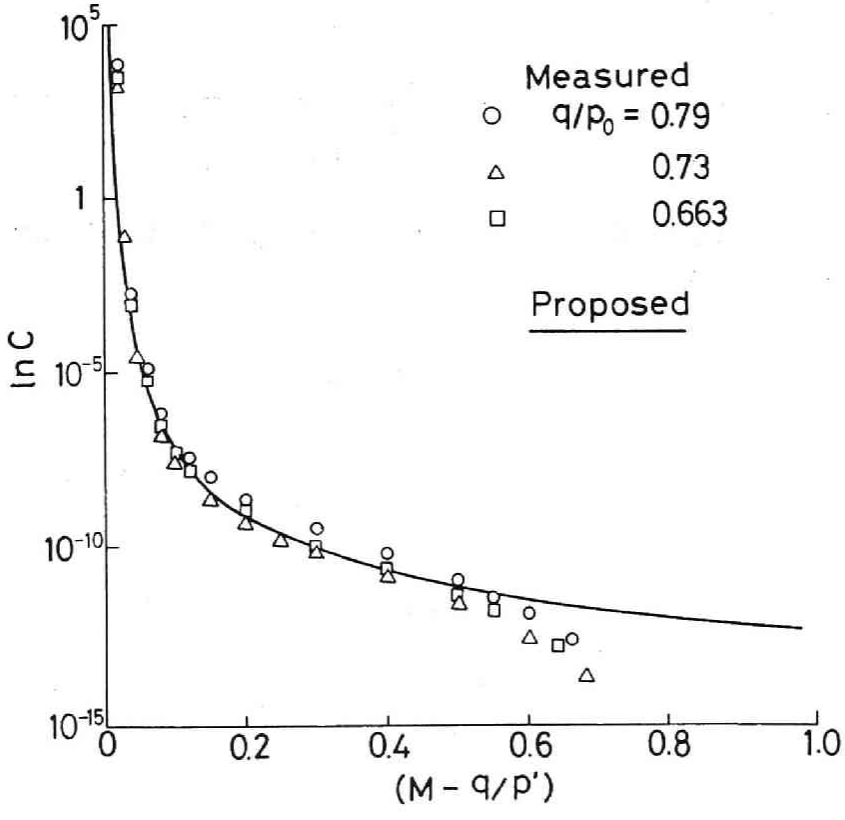

Fig. 6 Variation in the Viscoplastic Parameter, C with the Effective Stress State, $(M-q/p')$

to infinite. It is evident from *Eq.(3-10)*, that the strain rate implicitly contributes to this relation. *Fig.7* shows the $\dot{\varepsilon}_{11}/C$ - $\dot{\varepsilon}_{11}$ relations, a unique relation exists between $\dot{\varepsilon}_{11}/C$ and $\dot{\varepsilon}_{11}$ except in the acceleration creep stage in which viscoplastic flow occurs. Although the relation is slightly convex,

it can be regarded as almost linear in the range of the strain rate normally used for undrained triaxial compression tests. Therefore, it is natural that the C value determined from strain-controlled undrained triaxial compression tests should be constant. But, in cases such as the acceleration creep process, in which the strain rate changes drastically, the value of viscoplastic parameter C also changes greatly.

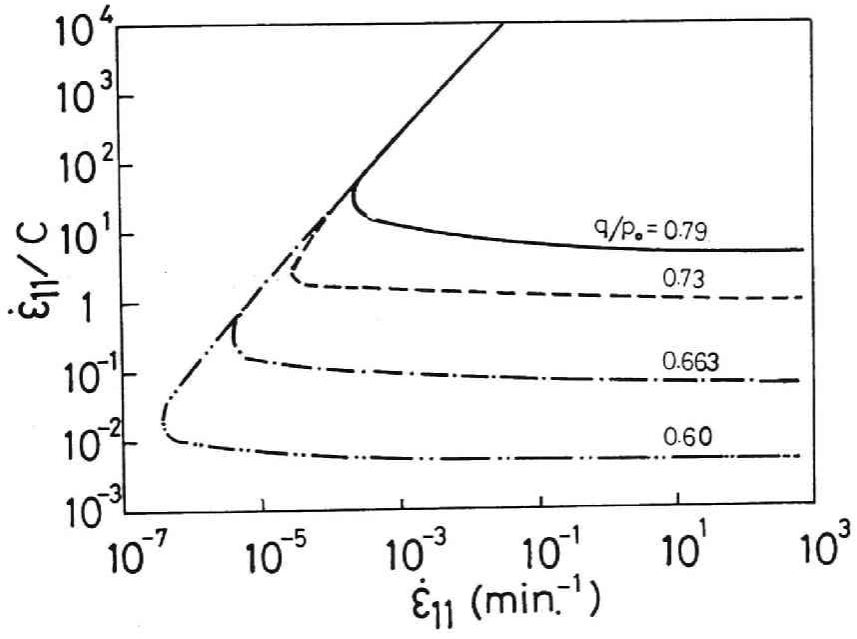

Fig. 7 Relation between Creep Strain Rate and the Viscoplastic Parameter, C

3-3-3. Formulation Taking into Account Variation in the Viscoplastic Parameter

Viscoplastic parameter C has been shown to vary under constant creep stress (*Figs. 6* and *7*). Here, the change of the viscoplastic parameter, C with the stress state is calculated by solving *Eq.(3-4)* with C. The proposed curve shown in *Fig. 6* is so determined from the experimental data by using the method of least squares. In the undrained creep process, the effective stress is reduced because of the generation of excess pore water pressure. Because the clay structure deteriorates with the decrease in

effective stress, the variation in viscoplastic parameter,C can be considered equivalent to this deterioration of the clay structure during undrained creep. From Sekiguchi's experimental results, the relation between the viscoplastic parameter, C and the stress ratio $(M-q/p')$ is

$$C = exp\left[\frac{\delta}{(M - q/p')} - \xi\right] \tag{3-11}$$

in which, δ and ξ are material constants determined experimentally. When the sustained load is prescribed, viscoplastic parameter C is determined by *Eq.(3-11)*, and the strain rate, $\dot{\varepsilon}_{11}$ is calculated as the function of the viscoplastic parameter and the mean effective stress. In the case of strain-controlled undrained shear, first the strain rate is prescribed, and once this strain rate is determined to be constant, the value of the viscoplastic parameter must remain constant throughout the process of shearing because of the relation shown in *Fig. 7*. Therefore, the framework of the Adachi and Oka model for strain rate-controlled undrained shear does not change. Undrained creep rupture as well as strain-controlled undrained triaxial compression can be simulated by applying the constitutive model according to the flowchart shown in *Fig. 8*.

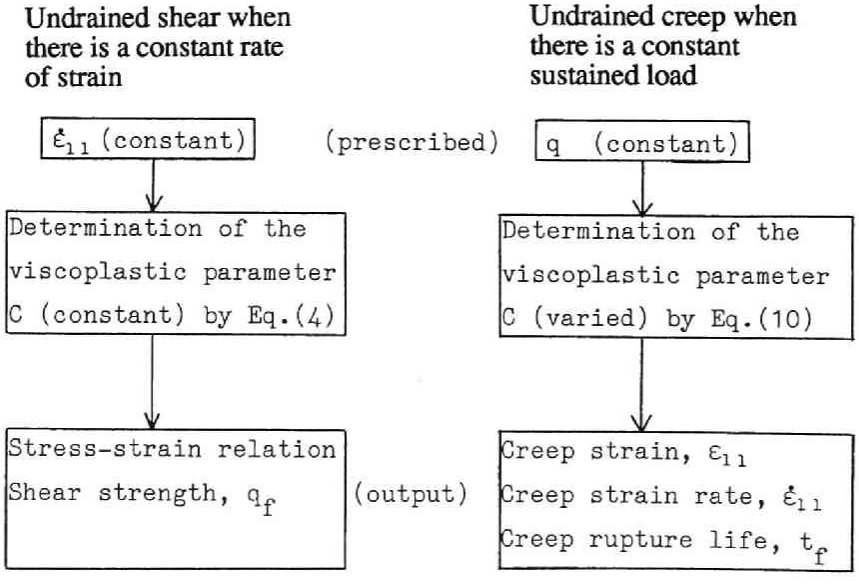

Fig. 8 The Flowchart of Calculations for Undrained Creep and Strain Rate-Controlled Undrained Shear

The modified stress strain relation for undrained condition is formulated as

$$\dot{\varepsilon}_{11} = \dot{\varepsilon}_{11}^{e} + \dot{\varepsilon}_{11}^{p} = \frac{\dot{q}}{3G} + \sqrt{\frac{2}{3}}\, C(\delta,\xi)\cdot exp\ \{m'(\frac{q}{Mp'} + \frac{\lambda}{\lambda - \kappa} ln \frac{p'}{p_0})\} \qquad (3\text{-}12)$$

3-3-4. Undrained Creep - Acceleration Creep Process-

Calculations for undrained creep were made with the modified overstress elasto-viscoplastic constitutive model defined by *Eq.(3-11)*. The material constants used are those for Umeda clay reported by Sekiguchi (1984). Two more material constants in *Eq.(3-11)*, *i.e.*, δ and ξ which are required to describe the proposed relation between the viscoplastic parameter, C and the stress state, $(M-q/p')$ were determined as *0.3* and *13.0* from the experimental results shown in *Fig. 6* by using the method of least squares. The creep strain - elapsed time relations are shown in *Fig. 9*. The calculated values show that remarkable undrained creep rupture follows acceleration creep independent of the magnitude of the creep stress. The values for calculated creep rupture life, t_f, are shown in *Table. 1* along with the experimental values. Calculated creep rupture life is known to be extremely sensitive to the sustained load, therefore, no estimation of the model's ability to predict undrained creep rupture life is possible with the limited amount of data available. But, we did ascertain that the modified overstress type model can describe the process of acceleration creep and can predict creep rupture life to some extent. The calculated creep strain

Table-1. Comparison of Creep Rupture Life

Creep stress (q/p_o)	t_f (min.) Calculated	t_f (min.) Measured
0.790	2.53×10^2	1.54×10^2
0.730	1.84×10^3	2.21×10^3
0.663	2.07×10^4	1.80×10^4

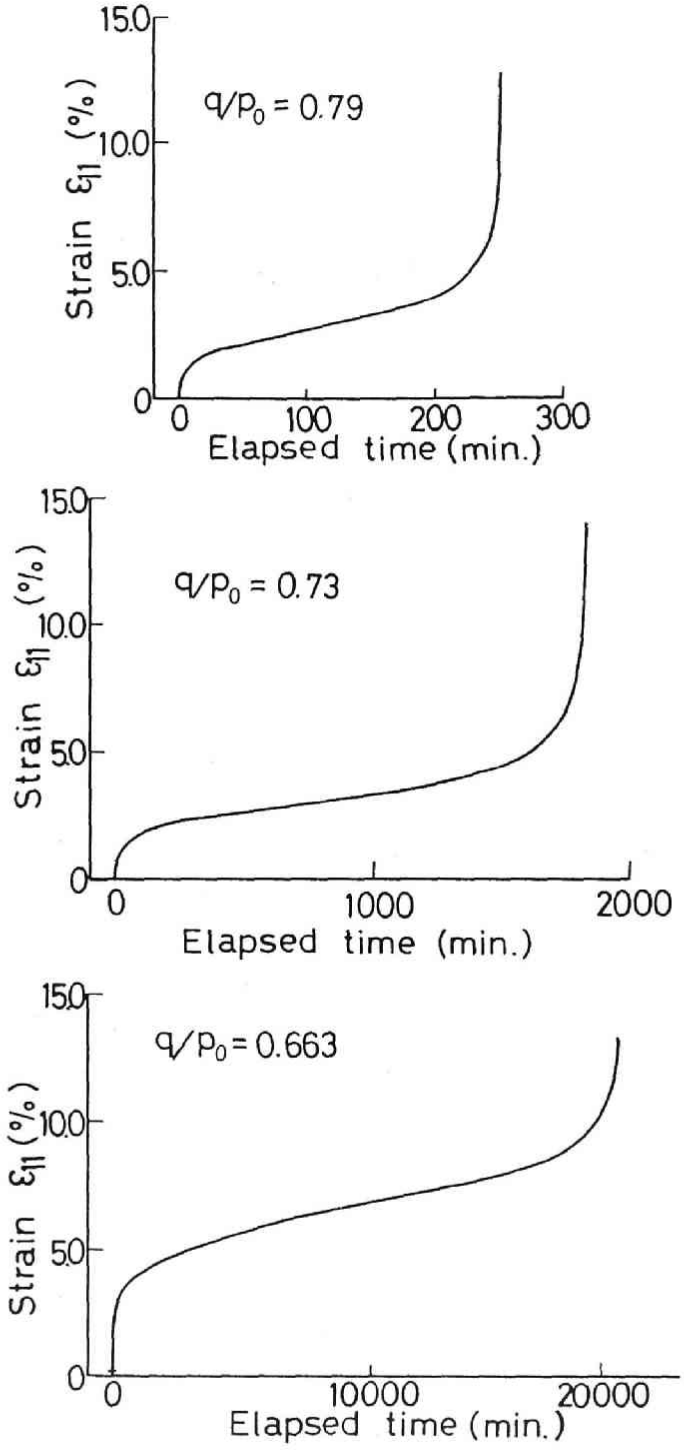

Fig. 9 Calculated Performance of Creep Strain with Elapsed Time for the modified Model

rate - elapsed time relations are shown in *Fig. 10*. This rate decreases in the primary stage and, after the minimum rate, it diverges to infinite, independent of creep stress. The modified constitutive model based on the assumption that viscoplastic parameter C varies with the function of the stress ratio $(M-q/p')$ thus has been adapted so that it can describes the undrained creep process, including acceleration creep and creep rupture.

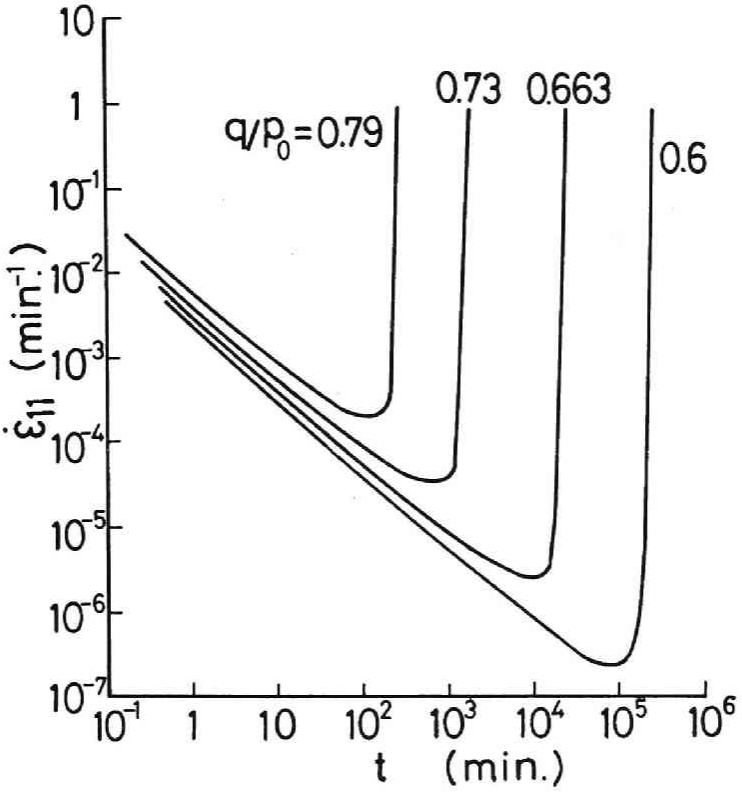

Fig. 10 Calculated Performance of Creep Strain Rate against Elapsed Time for the Modified Model

3-4. Introduction of Non-stationary Flow Surface Model

In this section, the concept of non-stationary flow surface is introduced in order to describe the undrained creep rupture by the overstress model.

3-4-1. Non-stationary Flow Surface Model and Adapted Overstress Model

Sekiguchi (1977) proposed an elasto-viscoplastic constitutive model based on the theory of non-stationary flow surface in order to describe the rate-dependent behavior of clay, such as time-dependency of strength, creep, stress relaxation etc. The viscoplastic flow rule is expressed in the following form:

$$\dot{\varepsilon}_{ij}^{p} = \Lambda \frac{\partial F}{\partial \sigma_{ij}'} \tag{3-13}$$

where Λ is a proportional coefficient and σ_{ij}', $\dot{\varepsilon}_{ij}^{p}$ are the effective stress tensor and the viscoplastic component of the strain rate respectively. F is the viscoplastic potential defined as follows:

$$F = \alpha \cdot \ln \left[1 + \frac{\dot{v}_0 \cdot t}{\alpha} \exp\left(\frac{f}{\alpha}\right)\right] = v^p \tag{3-14}$$

Here α is the secondary compression index, $\dot{v}_0$ is the reference volumetric strain rate, t is the elapsed time, f is a scalar function in terms of the mean effective stress, p' and the deviatoric stress, q and v^p is the viscoplastic volumetric strain. The function f is expressed as follows:

$$f = \frac{\lambda - \kappa}{1 + e_0} ln \left(\frac{p'}{p_0'}\right) + D \left(\frac{q}{p'} - \frac{q_0}{p_0'}\right) \tag{3-15}$$

where λ is the compression index, κ is the swelling index and D is the coefficient of dilatancy originally introduced by Shibata (1963). By introducing the condition for continued viscoplastic flow;

$$\dot{F} = \frac{\partial F}{\partial \sigma_{kl}'} \dot{\sigma}_{kl}' + \frac{\partial F}{\partial t} = \dot{v}^p \tag{3-16}$$

a proportional coefficient Λ can be determined. After a little calculation, the stress strain relation for the model is finally derived as follows:

$$\dot{\varepsilon}_{ij}^{p} = \frac{\partial f/\partial \sigma_{ij}'}{\partial f/\partial p}\cdot[\{1 - exp\ (-\frac{v^p}{\alpha})\}\dot{f} + \dot{v}_0 \cdot exp\ (\frac{f - v^p}{\alpha})] \qquad (3\text{-}17)$$

Let us here put $A=1-exp\ (-v^p/\alpha)$. In *Eq.(3-17)*, the first term of the bracket, $A\dot{f}$ is a stress rate term (f is a function of stress, p' and q) and the second term is an overstress term. Contribution of the stress rate term $A\cdot\dot{f}$ is one of the characteristics for this non-stationary flow surface model. By assuming here that $A=0$ in *Eq.(3-17)*, we can derive an overstress elasto-viscoplastic constitutive model expressed in the following form:

$$\dot{\varepsilon}_{ij}^{p} = \frac{\partial f/\partial \sigma_{ij}'}{\partial f/\partial p}\cdot[\dot{v}_0 \cdot exp\ (\frac{f - v^p}{\alpha})] \qquad (3\text{-}18)$$

In the next section, by comparing the performance of these two models, that is, the original non-stationary flow surface model and the adapted overstress model, with emphasis on the stress rate effect, difference in the theoretical structures of both models will be discussed in detail using the calculated performance of undrained creep and triaxial compression under the condition of the constant rate of strain.

3-4-2. Creep Equations for Both Models

Undrained creep equations for the original model and the adapted overstress model are summarized in *Table-2*. First of all, creep equation for the original model are explained briefly. The deviatoric strain, $\varepsilon(t)$ increases with the effective stress $p(t)$ under the condition of the constant creep stress, q *(Eq.(3-19))*. The change of the effective stress $p(t)$ with time can be analytically expressed by *Eq.(3-21)*. Here, $A(t)$ and $h(t)$ are time-dependent functions in terms of the mean effective stress $p(t)$. Considering the stress condition at failure, $p = p_f = q/M$ in *Eq.(3-21)*, creep rupture life, t_f can be analytically derived as shown by *Eq.(3-23)*. Furthermore, creep strain rate $\dot{\varepsilon}(t)$ and its derivative with time $\ddot{\varepsilon}(t)$ are shown by *Eq.(3-25)* and *(3-27)* respectively. Here, $B(t)$ is also a time-dependent function in terms of the mean effective stress $p(t)$.

Table-2 Undrained Creep Equations

Non-Stationary Flow Surface Model	Assumed Overstress Model
$\varepsilon(t)=\frac{(q-q_0)}{3G}+\frac{\kappa}{M(1+e_0)}\times\ln\left[\frac{M\cdot p_0-q}{M\cdot p(t)-q}\right]$ ····· (3-19)	$\varepsilon(t)=\frac{(q-q_0)}{3G}+\frac{\kappa}{M(1+e_0)}\times\ln\left[\frac{M\cdot p_0-q}{M\cdot p(t)-q}\right]$ ····· (3-20)
$\frac{\dot{v}_0\cdot t}{\alpha}=A(t)\cdot\exp\left\{-\frac{h(t)}{\alpha}\right\}$ ····· (3-21)	$\frac{\dot{p}}{p(t)}=\frac{(1+e_0)}{\kappa}\cdot\dot{v}_0\cdot\exp\left\{\frac{h(t)}{\alpha}\right\}$ ····· (3-22)
$t_f=\frac{\alpha}{\dot{v}_0}\cdot A(p_f)\cdot\exp\left[-\frac{h(p_f)}{\alpha}\right],\ p_f=\frac{q}{M}$ ····· (3-23)	$tf=\int_{p_0}^{p_f}\left(\frac{dt}{dp}\right)dp$ ····· (3-24)
$\dot{\varepsilon}(t)=\frac{\dot{v}_0\cdot\exp[h(t)/\alpha]}{[M-q/p(t)][1+A(t)\cdot B(t)]}$ ····· (3-25)	$\dot{\varepsilon}(t)=\frac{\dot{v}_0\cdot\exp[h(t)/\alpha]}{M-q/p(t)}$ ····· (3-26)
$\ddot{\varepsilon}(t)=\frac{M(\lambda-\kappa)}{\alpha\cdot\kappa}\cdot\frac{1+2A(t)\cdot B(t)}{1+A(t)\cdot B(t)}[\dot{\varepsilon}(t)]^2\cdot H(X,A)$ where $X=[q/p(t)]/M$ ····· (3-27)	$\ddot{\varepsilon}(t)=\frac{M(\lambda-\kappa)}{\alpha\cdot\kappa}\cdot[\dot{\varepsilon}(t)]^2\cdot H(X,0)$ where $X=[q/p(t)]/M$ ····· (3-28)
$H(X,A)=\frac{\alpha(1+e_0)}{\lambda-\kappa}X-\frac{(1-X)\left[\frac{\lambda}{\lambda-\kappa}-X\right]^2-(1-A(t))(1-X)^2}{\frac{\lambda}{\lambda-\kappa}+2A(t)\cdot(1-X)}$ ····· (3-29)	$H(X,0)=\frac{\alpha(1+e_0)}{\lambda-\kappa}X-(1-X)\left(\frac{2\lambda-\kappa}{\lambda-\kappa}-2X\right)$ ····· (3-30)
$A(t)=1-[p(t)/p_0]^{\kappa/\alpha(1+e_0)}$ ····· (3-31) $B(t)=\frac{\lambda-\kappa}{\kappa}\left[1-\frac{q}{M\cdot p(t)}\right]$ ····· (3-32)	$h(t)=\frac{\lambda}{1+e_0}\ln\left[\frac{p(t)}{p_0}\right]+\frac{\lambda-\kappa}{M(1+e_0)}\left[\frac{q}{p(t)}-\frac{q_0}{p_0}\right]$ ····· (3-33)

Secondly, the creep equations for the adapted overstress model are explained below. Creep strain is calculated by *Eq.(3-20)* which is completely same equation that for the original model (*Eq.(3-19)*). However, change of $p(t)$with time t must be derived by solving the differential equation *(3-22)* numerically. As far as creep rupture life, t_f is concerned, it must also be numerically calculated by *Eq.(3-24)*. Creep strain rate $\dot{\varepsilon}(t)$ and its derivative with time $\ddot{\varepsilon}(t)$ are shown by *Eq.(3-26)* and *(3-28)* respectively. In this chapter, Runge-Kutta-Gill method (*RKG*) is used for numerical calculation of t_f for the assumed overstress model. Here, accuracy of the numerical solution for t_f should be confirmed. Creep rupture life, t_f can fortunately be obtained analytically for the original model by *Eq.(3-23)*. The analytically derived t_f will be then compared with the numerically derived t_f by *RKG* for the original model (*Table-3*). For all given creep stress, the numerical solutions for t_f tend to overestimate the analytical ones with an error of 10 %.

Table-3 Analytical Creep Rupture Life and Errors due to Numerical Calculation (RKG)

Creep Stress (q/p_0)	Rupture Life (min)		
	analytical ①	R. K. G. ②	Error (②-①)/①
0. 6 0 0	2. 2 7 3 × 10^5	2. 4 9 0 × 10^5	0. 0 9 5
0. 6 6 3	1. 8 4 1 × 10^4	2. 0 2 0 × 10^4	0. 0 9 7
0. 7 0 0	4. 7 8 0 × 10^3	5. 2 8 0 × 10^3	0. 1 0 4
0. 7 9 0	2. 3 0 0 × 10^2	2. 5 2 0 × 10^2	0. 0 8 5

3-4-3. Condition of the Onset of the Acceleration Creep

It has been pointed out that acceleration creep and creep rupture, generally cannot be described by the overstress model. However, the adapted overstress model expressed by *Eq.(3-18)*, as well as the original

non-stationary flow surface model can describe these processes. In this section, then, the condition of the onset of the acceleration creep and its relation with the theoretical structure of the adapted overstress model will be discussed in detail.

Sekiguchi (1984) already afforded a theoretical proof that the original non-stationary flow surface model can describe the acceleration creep and creep rupture. Descriptive capability of the adapted overstress model is then discussed here. Creep rupture takes place with an infinite strain rate or deformation divergence just after reaching the state of the minimum strain rate, $\dot{\varepsilon}=\dot{\varepsilon}_{min}$, as schematically shown in *Fig. 4*. The existence of the minimum strain rate, $\dot{\varepsilon}_{min}$ ensures acceleration creep description by the constitutive model. In other words, it is necessary to confirm the condition that the time derivative of $\dot{\varepsilon}(t)$, $\ddot{\varepsilon}(t)$ is equal to zero. In *Eq.(3-28)*, the condition $\ddot{\varepsilon}(t)=0$ is satisfied only when the value of the function $H(X,0)$ is equal to zero because $(\dot{\varepsilon}(t))^2$ is always positive and $M(\lambda - \kappa)/\alpha\kappa$ is the positive definite. The concrete form of $H(X,0)$ is expressed by *Eq.(3-30)*. Let us prove the existence of the solution, $X=X_m$ for $H(X,0)=0$ graphically. The first term of *Eq.(3-30)* is expressed by Y_1:

$$Y_1 = \frac{\alpha(1+e_0)}{\lambda - \kappa} \cdot X$$

and the second term is expressed by Y_2:

$$Y_2 = (1 - X)\left(\frac{2\lambda - \kappa}{\lambda - \kappa}\right) - 2X$$

These equations are drawn on *Fig. 11*. The point of intersection of the aforementioned two functions will be the solutions for $H(X,0)=0$. As shown in *Fig. 11*, we have two solutions for *Eq.(3-30)*, however, since the stress state for normally consolidated clay is limited to $X \leq 1$ ($q/p' \leq M$), X_m should be the only solution with the physical meaning. Then, by being proved that strain rate $\dot{\varepsilon}(t)$ will become its minimum, $\dot{\varepsilon}_{min}$ at $X=X_m$, the assumed overstress model expressed by *Eq.(3-18)* is found to be able to describe the acceleration creep and creep rupture.

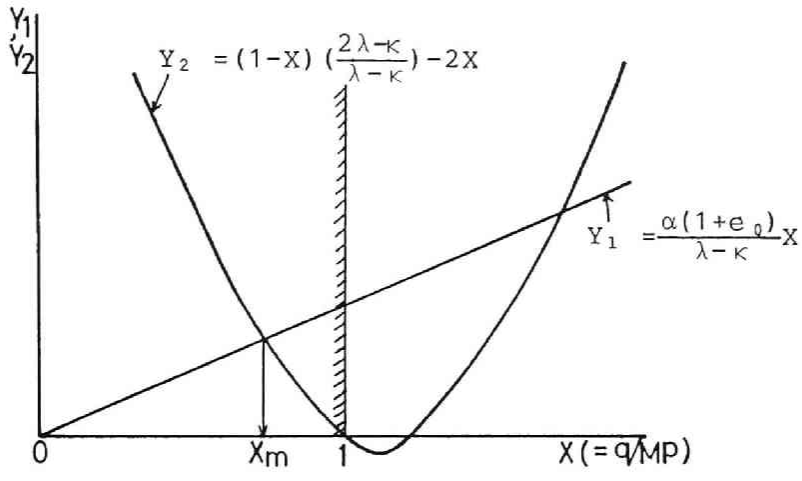

Fig. 11 Existence Condition of the Onset of the Acceleration Creep

Although many researchers have pointed out that the overstress model cannot describe acceleration creep and creep rupture caused by its theoretical structure, the assumed overstress model (*Eq.(3-18)*) is proved to describe these phenomena in this section.

3-4-4. Calculated Creep Strain - Elapsed Time Relations

Calculated undrained creep strain - elapsed time relations are shown in *Figs. 13*. The solid lines show the performance of the original non-stationary flow surface model and the hatched lines show the performance of the adapted overstress model. In all figures, q denotes the creep stress sustained, and p_0 represents the effective confining stress. Series of the calculated creep rupture life for both models are also shown in those figures, that is, $t_f^{(1)}$ and $t_f^{(2)}$ represent the creep rupture life for the original model (model 1) and the adapted model (model 2) respectively. Here, we must pay much attention to the fact that the adapted overstress model (model 2) can clearly describe the acceleration creep phase and the subsequent creep rupture, which has has been pointed out impossible to be described by a so-called overstress model.

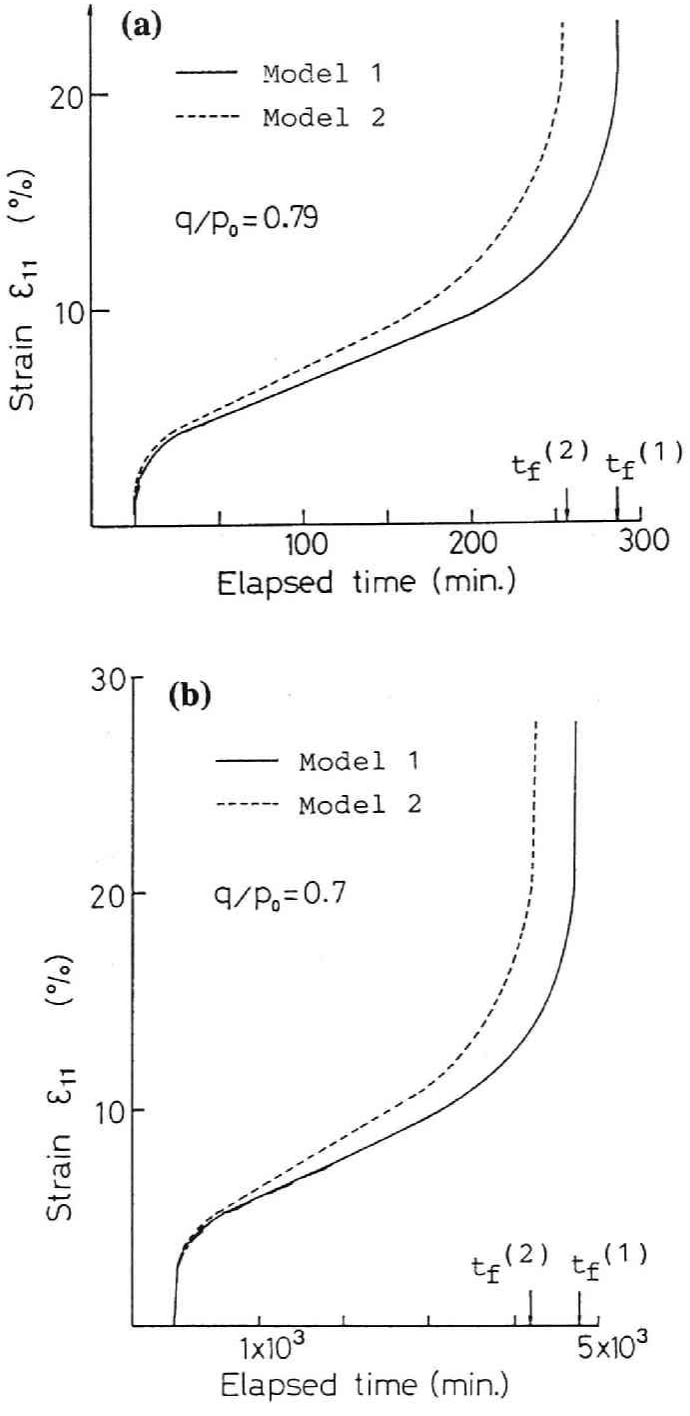

Fig. 12 Calculated Creep Strain with Elapsed Time by the Non-Stationary Flow Surface Model (Model 1) and the Adapted Overstress Model (Model 2); (a):q/p_0=0.790, (b):q/p_0=0.700

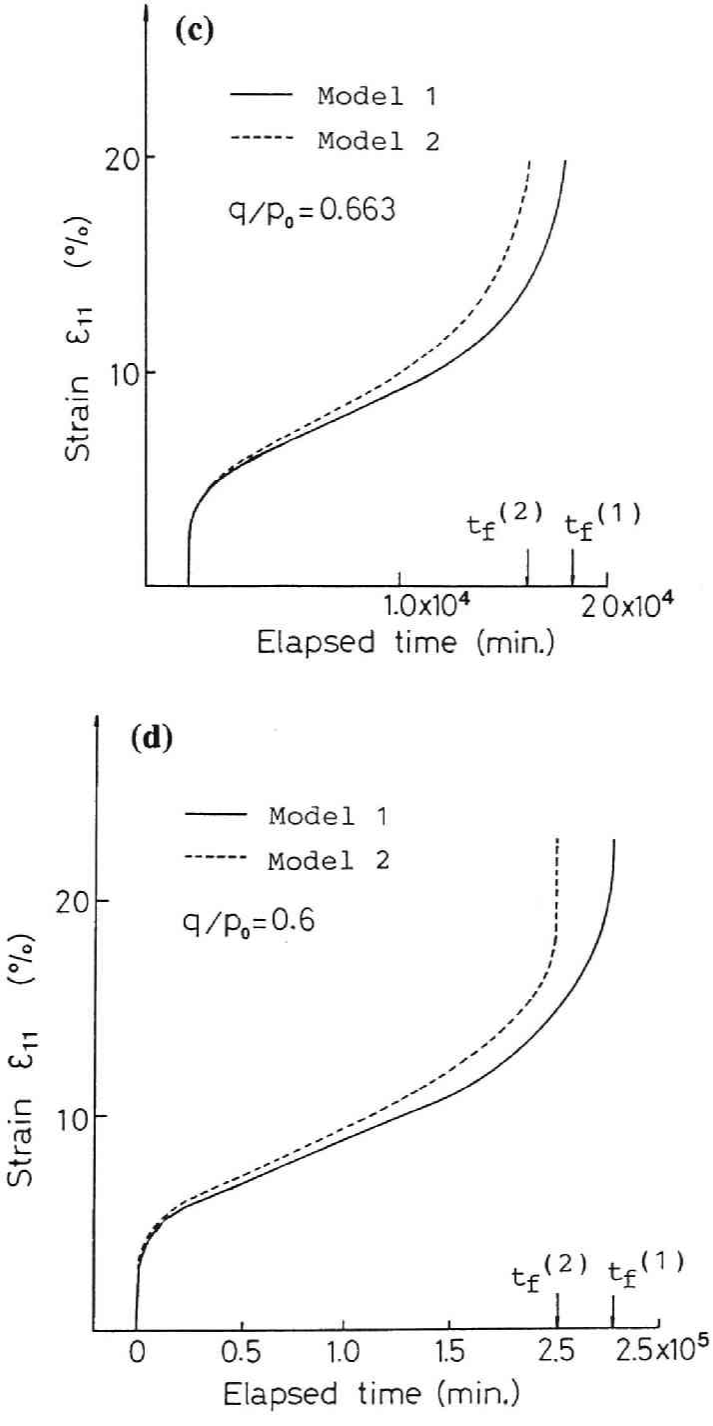

Fig. 12 Calculated Creep Strain with Elapsed Time by the Non-Stationary Flow Surface Model (Model 1) and the Adapted Overstress Model (Model 2); (c):q/p_0=0.663, (d):q/p_0=0.600

Series of the creep rupture life calculated by the adapted overstress model (model 2) that ignores the stress rate effect always underestimate those of the original model (model 1), independent of the creep stress level. Series of the creep rupture life, t_f calculated by these models are compared in *Table-4*. The values of t_f by the adapted overstress model (model 2) are 17 to 20 % smaller than those by the non-stationary flow surface model (model 1). With these results, the stress rate term, $A\dot{f}$ is found to prolong the moment of creep rupture occurrence in the framework of the elasto-viscoplastic model. Therefore, the original non-stationary flow surface model will always predict a little larger creep rupture life than the adapted overstress model due to stress rate effect.

Table-4 Comparison of Creep Rupture Life Calculated by the Non-Stationary Flow Surface model and the Adapted Overstress Model

q/p_0	$t_f^{(1)}$	$t_f^{(2)}$	$t_f^{(2)}/t_f^{(1)}$
0.790	2.30×10^{2}	1.86×10^{2}	0.81
0.700	4.78×10^{3}	3.99×10^{3}	0.83
0.663	5.87×10^{4}	4.90×10^{4}	0.83
0.600	2.27×10^{5}	1.90×10^{5}	0.84

3-5. Conclusions

Performance of undrained creep rupture in a triaxial compression is investigated. An overstress type elasto-viscoplastic constitutive model, has been modified so that it describes undrained creep phenomena, including acceleration creep and creep rupture. In summary:

(1) For the Adachi and Oka model, typical overstress model, a theoretical solution of undrained strength, q_f, has been introduced, in terms of strain rate and the viscoplastic parameter, C. The relation of the

strain rate to the viscoplastic parameter has been clarified through the analytical solution for undrained strength. Furthermore, variation in the stress ratio $(M-q/p')$ contributes to the viscoplastic parameter. Taking these factors into account, the relation between the stress ratio and the viscoplastic parameter has been formulated from experimental results.

(2) The overstress elasto-viscoplastic constitutive model has been proved capable of describing the acceleration creep process and undrained creep rupture by introducing the effect of structural deterioration, that is to say, the variations in the viscoplastic parameter shown as a function of the decrease in the mean effective stress and the variation in the creep strain rate.

(3) The overstress model can be introduced from the non-stationary flow surface model by ignoring the stress rate effect. This adapted overstress model is proved to be able to describe the acceleration creep and creep rupture under undrained triaxial condition, as well as the non-stationary flow surface model.

(4) Creep rupture life numerically calculated by the adapted overstress model is smaller than that by the non-stationary flow surface model.

REFERENCES

(1) Adachi, T. and Okano, M. (1974) : A Constitutive Equation for Normally Consolidated Clay, Soils and Foundations, Vol.14, No.4, pp.53-73.

(2) Adachi, T. and Oka, F. (1982) : Constitutive Equations for Normally Consolidated Clay Based on Elasto-Viscoplasticity, Soils and Foundations, Vol.22, No.4, pp.57-70.

(3) Adachi, T., Oka, F and Mimura, M. (1985) : Descriptive Accuracy of Several Existing Constitutive Models for Normally Consolidated Clays, Proc. 5th ICONMG, Vol.1, pp.259-266.

(4) Aubry, D., Kodaissi, E. and Meimon, E. (1985) : A Viscoplastic Constitutive Equations for Clays including Damage Law, Proc. 5th ICONMG, Vol.1, pp.421-428.

(5) Dafalias, Y. (1982) : Bounding Surface Elastoplasticity-Viscoplasticity for Particulate Cohesive Media, Proc. IUTAM Symp. on Deformation and Failure of Granular Materials, pp.97-107.

(6) Dragon, A. and Mroz, Z. (1979) : A Model for Plastic Creep of Rock-like Materials Accounting for the Kinetics of Fracture, Int. J. Rock Mech. Min. Sci. Geomech., Abstr., Vol.16, pp.253-259.

(7) Katona, M. G. (1984) : Evaluation of Viscoplastic Cap Model, J. Geotech. Eng., ASCE, Vol.110, No.8, pp.1106-1125.

(8) Matsui, T and Abe, N (1984) : Introduction to Constitutive Equations of Soils, Tsuchi-to-Kiso. JSSMFE, Vol.32, No.1, pp.71-79.

(9) Matsui, T. and Abe, N. (1985) : Elasto/Viscoplastic Constitutive Equation of Normally Consolidated Clays based on Flow Surface Theory, Proc. 5th ICONMG, Vol.1, pp.407-413.

(10) Mimura, M. and Sekiguchi, H. (1985) : A Review of Elasto-Viscoplastic Models with Particular Emphasis on Stress-Rate Effect, Proc. 20th Japan Nat. Conf. SMFE, pp.403-406(in Japanese).

(11) Mimura, M. and Sekiguchi, H. (1985) : A Review of Existing Viscoplastic Constitutive Models Regarding the Performance of Creep Rupture Prediction, Proc. 40th Japan Nat. Conf. JSCE, pp.461-462 (in Japanese).

(12) Mimura, M. and Sekiguchi, H. (1986) : Some Remarks on the Delayed Failure of Clay Foundations, Proc. 21th Japan Nat. Conf. SMFE, pp.1097-1100(in Japanese).

(13) Murayama S. and Shibata, T. (1956) : On the Rheological Characters of Clay, Transaction of JSCE, No.40, pp.1-31 (in Japanese).

(14) Nova, R. (1982) : A Viscoplastic Constitutive Model for Normally Consolidated Clay, Proc. IUTAM Symp. on Deformation and Failure of Granular Materials, pp.287-295.

(15) Oka, F. (1981) : Prediction of Time Dependent Behavior of Clay, Proc. 10th ICSMFE, Vol.1, pp.215-218.

(16) Oka, F. (1985) : Elasto-Viscoplastic Constitutive Equations with Memory and Internal Variables, Computer and Geomechanics, Vol.1, pp.59-69.

(17) Perzyna, P. (1963) : The Constitutive Equations for Workhardening and Rate Sensitive Plastic Materials, Proc. of Vibrational Problems, Warsaw, Vol.4, No.3, pp.281-290.

(18) Roscoe, K. H., Schofield, A. N. and Wroth, C. P. (1958) : On the Yielding of Soils, Geotechnique, Vol.8, pp.22-53.

(19) Schofield, A. N. and Wroth, C. P. (1968) : Critical State Soil Mechanics, McGraw-Hill.

(20) Sekiguchi, H. (1977) : Rheological Characteristics of Clays, Proc. 9th ICSMFE, Vol.1, pp.289-292.

(21) Sekiguchi, H. (1984) : Theory of Undrained Creep Rupture of Normally Consolidated Clay based on Elasto-Viscoplasticity, Soils and Foundations, Vol.24, No.1, pp.129-147.

(22) Shibata, T. (1963) : On the Volume Changes of Normally-consolidated Clays, Annuals, Disaster Prevention Research Institute, Kyoto University, No. 6, pp.128-134 (in Japanese).

CHAPTER 4

Bearing Capacity and Plastic Flow of a Rate-Sensitive Clay under Strip Loading

4-1. Introduction

The bearing capacity of loaded clay mass varies significantly with the passage of time. Under unfavorable conditions, the clay mass can undergo eventual failure after the action of embanking or excavation is completed. Such delayed failure obviously merits a due consideration in the construction control for embankments on clay foundations as well as in the design of cut slopes in clay. However, it seems that the governing mechanism has not been fully clarified on the quantitative basis.

This state of the art will be understandable in view of the fact that the process of delayed failure is affected by a number of factors which include the mode and speed of loading, the consolidation history of the clay deposits as well as the physical nature of the constituent soil. In the case of embanking, for example, partial consolidation may be expected to occur in the foundation clay along with contained plastic flow. However, it should be recognized here that the occurrence of partial consolidation does not automatically mean the increase in bearing capacity of the foundation clay, because the partial consolidation is often accompanied by abrupt breakdown in structure of that foundation clay. This aspect is particularly true of highly sensitive, natural clay deposits (Leroueil *et al.*,1979). The problem of delayed failure becomes even more complicated by the well-known fact that the clay skeleton itself has a marked rate-sensitivity (or intrinsic time effect), as exemplified by creep rupture phenomena (Casagrande and Wilson, 1951).

Particular emphasis will be placed on the clarifying the time-dependent bearing capacity of a rate-sensitive, saturated clay under strip loading, with due consideration of its two-phase nature as well. In this

chapter, for this purpose, after a brief review of the non-stationary flow surface elasto-viscoplastic constitutive model, coupled stress-flow analyses will subsequently be made for the homogeneous model clay foundation using the method of finite elements. Then, the primary characteristics of the rate-sensitive behavior of normally consolidated clay mass will be numerically investigated.

4-2. A Plane-strain Viscoplastic Constitutive Model

4-2-1. Introductory Remarks

A viscoplastic constitutive model proposed by Sekiguchi (1977, 1982) is used here to describe the rate-sensitive, plastic behavior of the foundation clay, along with the plane-strain version suggested by Sekiguchi *et al.*, 1982). Note that the plan-strain viscoplastic model is capable of evaluation of K_0 value at rest (sekiguchi, 1983). This is so significant because the calculated performance for geotechnical events can be much influenced by the initial stress condition. Taking this predictivity of K_0 value into considertation, the plane-starin version of the elasto-viscoplastic model will be used for the finite element analysis performed. Its feature of reproducing the process of undrained creep rupture is particularly important herein, because the aim of this chapter lies in critically examining the contribution of such intrinsic time-effect to the so-called delayed failure of clay mass. In the next section, the predicted performance of undrained creep rupture will be outlined. The mathematical structure of the plane-strain version of the viscoplastic constitutive model is shown in *Table-1* together with the original model. Here, the superscript, p, is used here to identify the viscoplastic component of any physical quantity. Note that the dilatancy function, $g(\xi)$ in the plane-strain version has been specified in the following equation.

$$g(\xi) = \frac{(\lambda - \kappa)}{2(1 + e_0)} \ln \left[\frac{\xi^2 - \xi + \mu}{\xi_0^2 - \xi_0 + \mu}\right] +$$

$$\frac{(\lambda - \kappa)}{2(1 + e_0)\sqrt{\mu - 1/4}} \left[\arctan\left\{ \frac{\xi - 1/2}{\sqrt{\mu - 1/4}} \right\} - \arctan\left\{ \frac{\xi_0 - 1/2}{\sqrt{\mu - 1/4}} \right\} \right] \qquad (4\text{-}1)$$

where ξ denotes the stress ratio, s/r and ξ_0 stands for its initial value. It is evident from *Table-1* that the mathematical structure of each model is essentially the same. A principal difference lies in that, as its name implies, the plane-strain version is based on the two-dimensional stress parameters, r and s, instead of their counterpart, p and q. Another point to be made here is that the plane-strain version leads to generally better predictions for K_0 values ; that is a direct consequence of the specific relation between $\dot{\gamma}^p/\dot{v}^p$ and $\xi(=s/r)$ indicated in *Table-1*.

4-2-2. Theoretical Features of Undrained Creep Rupture

Let us consider the situation where a K_0 consolidated clay element is subjected to creep loading under undrained plane-strain condition. Here, K_0 denotes the coefficient of earth pressure at rest. Imagine that the maximum shear stress, $s= (\sigma_1'-\sigma_3') / 2 \ (=(\sigma_1 - \sigma_3)/ 2)$, is instantaneously increased to a prescribed value and then maintained exactly constant with time. Here, σ_1' and σ_3' are the maximum and minimum principal stresses in terms of effective stress, whereas σ_1 and σ_3 denote the maximum and minimum principal stresses in terms of total stress. Then, the plane-strain viscoplastic model predicts that creep straining is accomplished by the gradual reduction in mean effective stress, $r=(\sigma_1'+\sigma_3') / 2$. Note that this interesting aspect of undrained creep is a direct consequence of contractancy (or negative dilatancy) of the clay considered.

Indeed, the imposed, undrained condition for the contractant clay requires the mean effective stress, $r=(\sigma_1'+\sigma_3') / 2$, to vary with time, t, in the following form :

$$A\ (r(t))\ \ exp\ \left[\frac{-h\ (r(t))}{\alpha}\right] = \frac{t}{\alpha/\dot{v}_0} \qquad (4\text{-}2)$$

Here, $A(r(t))$ and $h(r(t))$ are functions of the mean effective stress $r(t)$, both of which will be defined subsequently. The constants α and $\dot{v}_0$

Table-1 Features of Two Elasto-viscoplastic Model

Subject	Sekiguchi (1977)	Plane-strain Version (1982)
Viscoplastic Flow Rule	$\dot{\varepsilon}_{ij}^{p} = \Lambda \frac{\partial F}{\partial \sigma'_{ij}}$	
Viscoplastic Potential	$F = \alpha \cdot ln\left[1 + \frac{\dot{v}_0 \cdot t}{\alpha} exp\left(\frac{f}{\alpha}\right)\right] = v^p$	
Consistency Condition	$\dot{F} = \frac{\partial F}{\partial \sigma'_{ij}} \cdot \dot{\sigma}'_{ij} + \frac{\partial F}{\partial t} = \dot{v}^p$	
Static Yield Function	$f = \frac{\lambda - \kappa}{1 + e_0} ln\left(\frac{p}{p_0}\right) + D \cdot \left(\frac{q}{p} - \frac{q_0}{p_0}\right)$ *where* $p = \frac{1}{3}\sigma'_{ii}$ $q = \sqrt{\frac{3}{2} s_{ij} s_{ij}}$ $(i, j = 1,3)$	$f = \frac{\lambda - \kappa}{1 + e_0} ln\left(\frac{r}{r_0}\right) + g \cdot \left(\frac{s}{r}\right)$ *where* $r = \frac{1}{2}\sigma'_{ii}$ $s = \sqrt{\frac{1}{2} s_{ij} s_{ij}}$ $(i, j = 1,2)$
Strain-rate Parameters	$\frac{\dot{\varepsilon}^p}{\dot{v}^p} = \frac{1}{M - q/p}$ *where* $*\dot{\varepsilon}^p = \frac{2}{3}(\dot{\varepsilon}_1^p - \dot{\varepsilon}_3^p)$ $\dot{v}^p = \dot{\varepsilon}_1^p + \dot{\varepsilon}_2^p + \dot{\varepsilon}_3^p$	$\frac{\dot{\gamma}^p}{\dot{v}^p} = \frac{s/r}{\sin\phi' - s/r}$ *where* $\dot{\gamma}^p = \dot{\varepsilon}_1^p - \dot{\varepsilon}_3^p$ $\dot{v}^p = \dot{\varepsilon}_1^p + \dot{\varepsilon}_3^p$

* For the purpose of illustration the particular expression valid for axisymmetric strain conditions is listed here.

appearing in *Eq. (4-2)* represent the secondary compression index and the reference volumetric strain rate respectively.

The failure criterion associated rigorously with the plane-strain viscoplastic model, is expressed as follows:

$$s_f/r_f = \sin\phi' \tag{4-3}$$

where ϕ' is the angle of internal friction in terms of effective stress and is constant for a given clay. In the creep testing, the value of shear stress, $s = (\sigma_1'-\sigma_3')/2 = (\sigma_1 - \sigma_3)/2$, is maintained constant with time. Thus, the value of the mean effective stress, r_f, at creep rupture is expressed as follows:

$$r_f = s_f / \sin\phi' = s_f / \mu \tag{4-4}$$

where μ stands for $\sin\phi'$. In view of this relation, the creep rupture life, t_f, can be expressed in the following form:

$$t_f = (\alpha/\dot{v}_0)\cdot A(r_f)\cdot \exp\,[-h(r_f)/\alpha] \tag{4-5}$$

where the values of $A(r_f)$ and $h(r_f)$ are specified by

$$A(r_f) = 1 - [\, r_f/r_0]^{\frac{\kappa}{\alpha(1+e_0)}} \tag{4-6}$$

$$h\,(r_f) = -\frac{\lambda}{1+e_0}\ln\left(\frac{r_f}{r_0}\right) + \frac{(\lambda-\kappa)}{2(1+e_0)}\ln\left(\frac{\mu^2}{\xi_0^2-\xi_0+\mu}\right) +$$

$$\frac{(\lambda-\kappa)}{2\,(1+e_0)\sqrt{\mu-1/4}}\left[\arctan\left\{\frac{\mu-1/2}{\sqrt{\mu-1/4}}\right\} - \arctan\left\{\frac{\xi_0-1/2}{\sqrt{\mu-1/4}}\right\}\right] \tag{4-7}$$

Here, κ is the swelling index, λ is the compression index, e_0 is the initial void ratio, r_0 is the initial mean effective stress and ξ_0 is the initial value of the effective stress ratio, $\xi = s/r$. The features of the derived relation *(4-5)* are exemplified in *Fig. 1*, for three different values of the lumped parameter: $a(1+e_0)/\lambda$. The specific value of $a(1+e_0)/\lambda = 0.0217$ is selected

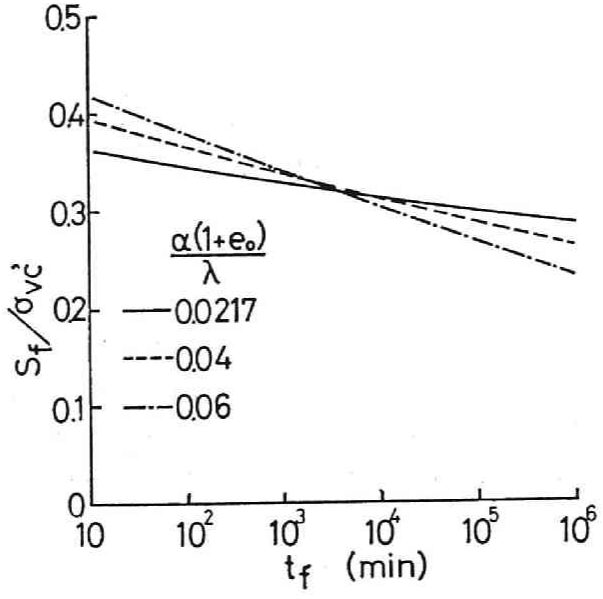

Fig. 1 Relations between Creep Stress and Creep Rupture Life

here for Fujinomori clay, in combination with the values of other parameters given in *Table-2*. The performances of the case having $a(1+e_0)/\lambda = 0.04$ and 0.06 are illustrated for purpose of comparison. It may be appropriate here to mention that the development of the shear creep strain, $\gamma = \varepsilon_1 - \varepsilon_3$, is clearly related to the evolution of $r(t)$ with time.

Table-2 Values of Material Parameters for Fujinomori Clay

Compression index	$\lambda=0.115$
Swelling index	$\kappa=0.0117$
Stress ratio at critical state	$\sin\phi'=0.567$
Secondary compression index	$\alpha=0.0013$
Reference volumetric strain rate	$\dot{v}_0=1.3\times10^{-7}$ min^{-1}
Elastic shear modulus	$G=120.0$kgf/cm^2
Consolidation pressure	$\sigma'_{vo}=\sigma'_{vc}=1.0$kgf/cm^2
Initial void ratio (for $\sigma'_{vc}=1.0$kgf/cm^2)	$e_0=0.927$
Coefficient of earth pressure at rest	$K_0=0.539$
Permeability coefficient at reference	$k_0=8.67\times10^{-7}$cm/min.
Rate of permeability change against e	$\lambda_k=0.238$

Indeed, the following relation can be derived for a given constant value of shear stress, s.

$$\gamma(t) = \frac{(s - s_0)}{G} + \frac{\kappa}{1 + e_0} ln \left[\frac{\mu - s/r}{\mu - s/r(t)}\right] \tag{4-8}$$

Here, s_0 is the value of shear stress at the K_0-consolidated phase prior to the undrained creep considered, and G is the modulus of shear rigidity.

Let us now remember that the value of $r(t)$ for a given time, t, can be determined from *Eq. (4-2)*. Actually, this equation is a transcendental equation regarding $r(t)$. Therefore, in the present study, the value of $r(t)$ for any given value of t is obtained numerically by means of the method of bisection. By substituting thus obtained values of $r(t)$ into *Eq. (4-8)*, we can construct a shear-creep curve for any given stress system for a given set of material parameters. In *Fig. 2*, two such creep curves are indicated. The basic creep rupture characteristics outlined above will serve as a reference of discussion in the next section.

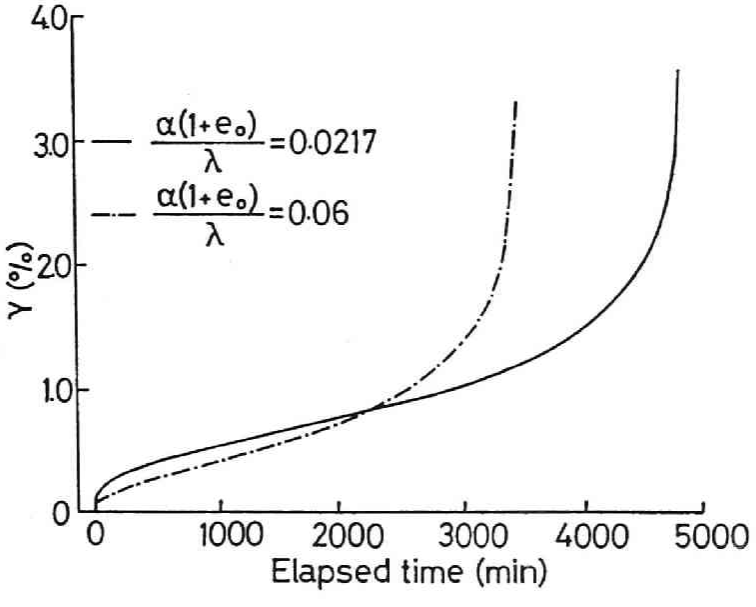

Fig. 2 Relations between Creep Strain and Elapsed Time

4-3. Coupled Stress-Flow Analysis in Terms of Finite Elements

4-3-1. Features of Finite Element Analysis

The viscoplastic constitutive relations are implemented into the finite element analysis procedure through the following incremental form:

$$\{\Delta\sigma'\} = [C^{ep}]\{\Delta\varepsilon\} - \{\Delta\sigma^R\} \tag{4-9}$$

Here, $\{\Delta\sigma'\}$ and $\{\Delta\varepsilon\}$ are the associated sets of effective stress increments and strain increments, and $[C^{ep}]$ stands for the elasto-viscoplastic coefficient matrix. The term $\{\sigma^R\}$ represents a set of '*relaxation stress*' which increases with time when strain is held constant. The pore-water flow is assumed here to obey isotropic Darcy's law. In this connection, it is further assumed that the coefficient of permeability, k, depends on the void ratio, e, in the following form:

$$k = k_0 \cdot \exp\left(\frac{e - e_0}{\lambda_k}\right) \tag{4-10}$$

in which, k_0 is the initial value of k at $e=e_0$ and λ_k is a material constant governing the rate of change in permeability subjected to the change in void ratio.

The geometry of the problem to be analyzed in this section is shown in *Fig. 3*, together with the finite element mesh used. Note that each quadrilateral element consists of four constant-strain triangles. and also, note that the nodal displacement increments and the element pore-water pressure are taken as the primary unknowns of the problem. The finite element equations governing those unknowns are established on the basis of Biot's formulation (Christian, 1968, Akai and Tamura, 1976, Shibata and Sekiguchi, 1980), and are solved by using the semi-band method of Gaussian elimination. The width of the loading strip, B, is chosen to be equal to $B=10cm$. The thickness of the foundation clay, H, is selected to be equal to $2B$, whereas the distance from the center line of the loaded area to the lateral boundary, L, is taken as $3B$. It is assumed that the foundation

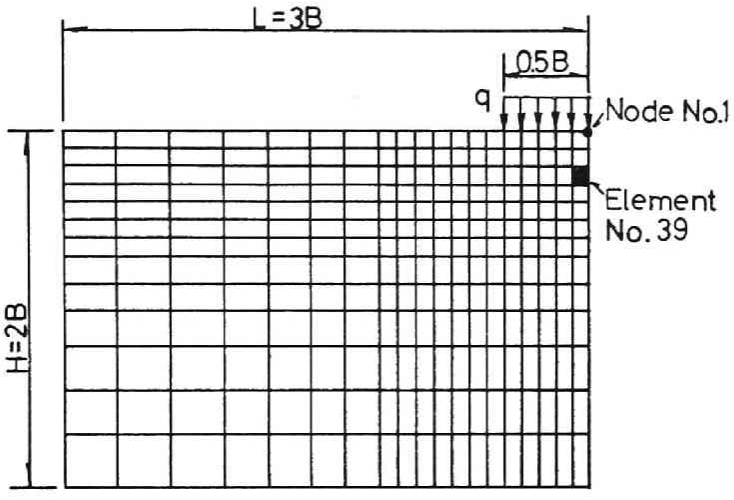

Fig. 3 Finite Element Mesh with Description of Boundary Condition Imposed

clay has been normally consolidated under K_0 conditions at a vertical consolidation pressure of $\sigma_{VC}'=1.0$ *kgf/cm²* *(98 kPa)* for 10^4 minutes, prior to the subsequent loading stage. The values of the material constants as well as the initial state variables for the foundation clay, are summarized in *Table-2*. Three types of loading tests are subsequently analyzed, as shown in *Table-3*. Here, $\dot{q}$ denotes the loading rate employed at the constant-rate-

Table-3 Finite Element Analysis Performed

Drainage condition	Loading mode	Remarks
Undrained	CRL*	$\dot{q}/\sigma_{vc}'=1.25\times10^{-2}$ min.$^{-1}$
		1.04×10^{-3} min.$^{-1}$
		1.04×10^{-4} min.$^{-1}$
	CREEP	$q/\sigma_{vc}'=1.800$
		1.725
		1.650
Partially Drained	CRL*	$\dot{q}/\sigma_{vc}'=1.25\times10^{-2}$ min.$^{-1}$

*CRL=Constant Rate of Loading tests

of-loading stage. Note that in the case of partially drained loading, the drainage is allowed to occur both from the upper and lower boundaries of

the foundation clay, whereas in the case of undrained loading, the coefficient of permeability is set equal to zero in the entire region of the foundation clay for computational purpose.

4-3-2. Results and Discussion

4-3-2-(1). Effect of Loading Rate on Undrained Bearing Capacity

The load settlement curves obtained at three different loading rates under undrained conditions, are shown in *Fig. 4*, together with the load

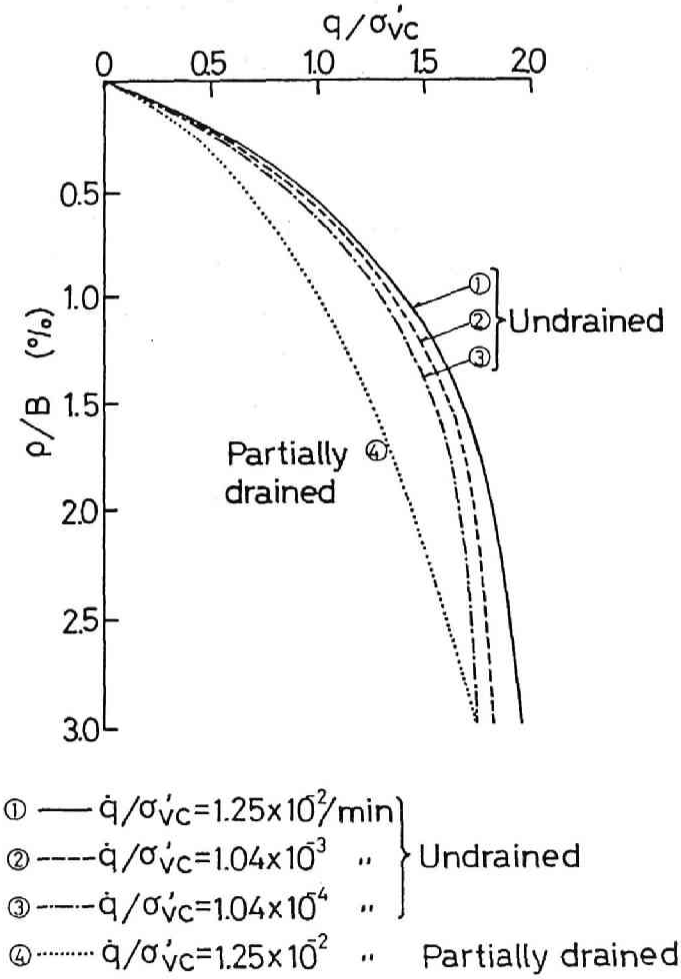

Fig. 4 Calculated Load Settlement Curves

settlement curve under partially drained condition. It is seen that, in each of three undrained cases, the foundation clay practically reaches the ultimate state when the dimensionless settlement, ρ/B, becomes equal to *3 %*. The values of the dimensionless load, q/σ_{VC}', at the ultimate state are respectively equal to *1.95*, *1.875* and *1.8*, at the loading rates of $\dot{q}/\sigma_{VC}'=1.25 \times 10^{-2}$ min^{-1}, 1.04×10^{-3} min^{-1} and 1.04×10^{-4} min^{-1}. This means that for this particular problem, the ten-fold change in loading rate gives rise to *4 %* change of the bearing capacity, q/σ_{VC}'.

The effective stress paths followed by a particular element, *No. 39* indicated on *Fig. 3*, are shown in *Fig. 5*. It is seen that the values of the dimensionless shear stress, σ/σ_{VC}', at the ultimate state are equal to *0.346*, *0.330* and *0.316* respectively at the loading rate of $\dot{q}/\sigma_{VC}'=1.25 \times 10^{-2}$ min^{-1}, 1.04×10^{-3} min^{-1} and 1.04×10^{-4} min^{-1}. It is of interest here to mention that the bearing capacity factor, N_C, is equal to *5.67* in this particular problem, irrespective of the loading rates imposed.

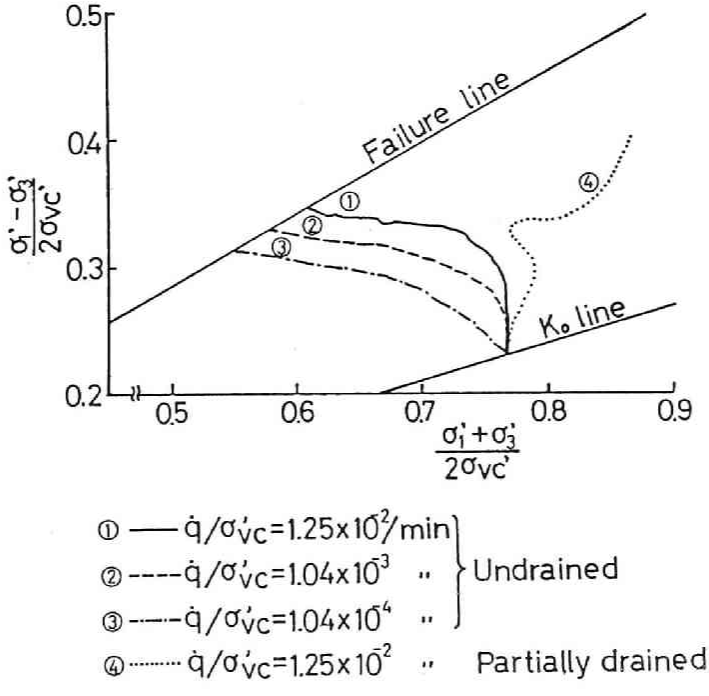

Fig. 5 Calculated Effective Stress paths Followed by a Representative Soil Element

4-3-2-(2). Effect of Stress Redistribution on Undrained Creep Rate

Let us consider the performance of undrained creep after the stoppage of the constant rate of loading. The loading speed prior to the creep phase is selected here to be equal to $\dot{q}/\sigma_{VC}'=1.25 \times 10^{-2}$ min^{-1}. The time settlement curves for such creep tests at three different values of sustained loads are shown in *Fig. 6*. A line of *'failure settlement'* given by $\rho/B=3$ %, is also drawn for purpose of comparison. It is seen that in case *C* with $q/\sigma_{VC}'=1.65$, the development settlement with time is very limited. In case *B* with $q/\sigma_{VC}'=1.725$, the settlement is seen to develop at greater rates, as compared with case *C*. At the highest creep stress of $q/\sigma_{VC}'=1.8$ (*i.e.*, in case *A*), the settlement is seen to develop abruptly and exceeds the line of failure settlement in *900* minutes. It should be noted, however, that even in case *A* with the highest creep stress level, a sign of so-called accelerating creep is not clearly detected.

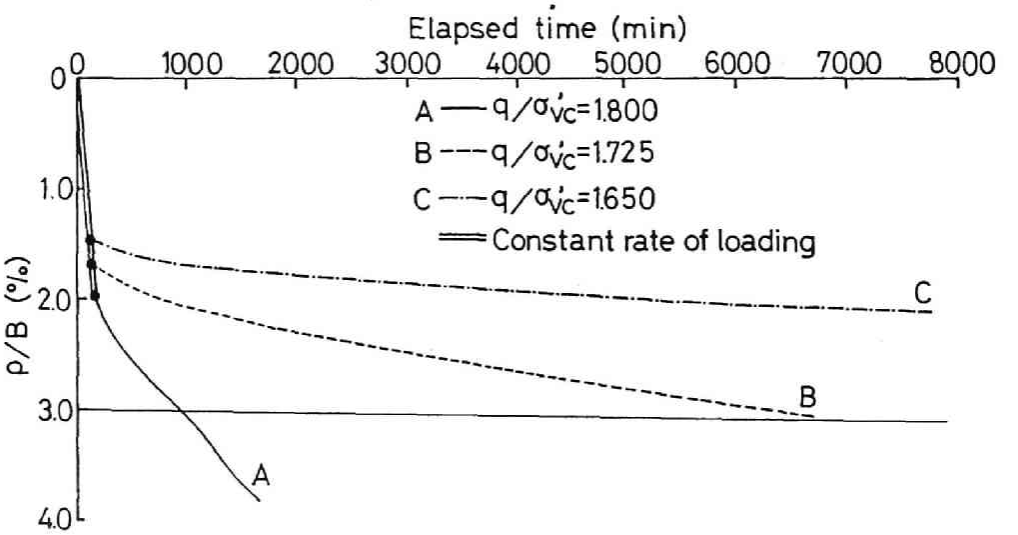

Fig. 6 Time Settlement Curves for Sustained Loading under Undrained Conditions

The evolution of effective stress state during the undrained creep process is shown in *Fig. 7*. It is seen that the effective stress state migrates with time toward the failure line, with the shear stress being gradually reduced. The relations between the final value of the shear stress, *s*, and the loading time, *t*, are shown in *Fig. 8*. The results for the aforementioned

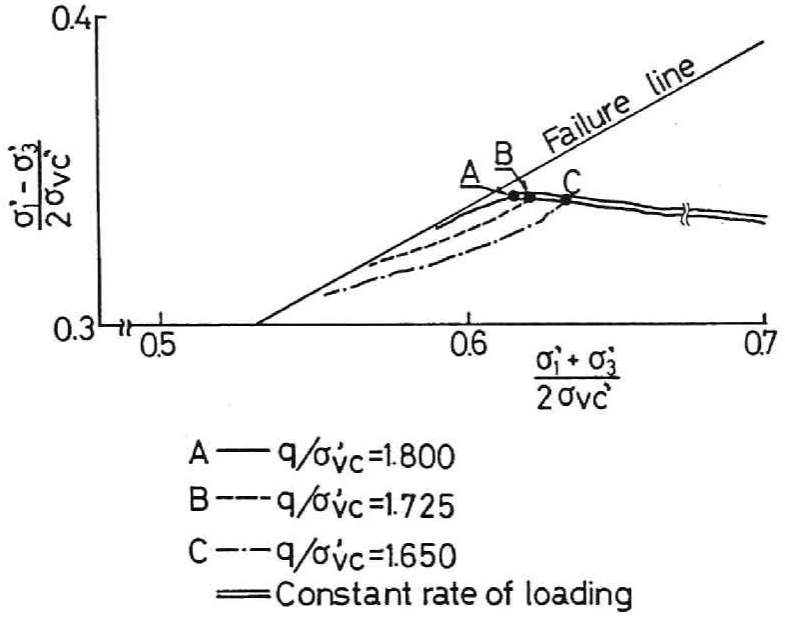

Fig. 7 Effective Stress Paths Followed by a Representative Soil Element, during Sustained Loading under Undrained Conditions

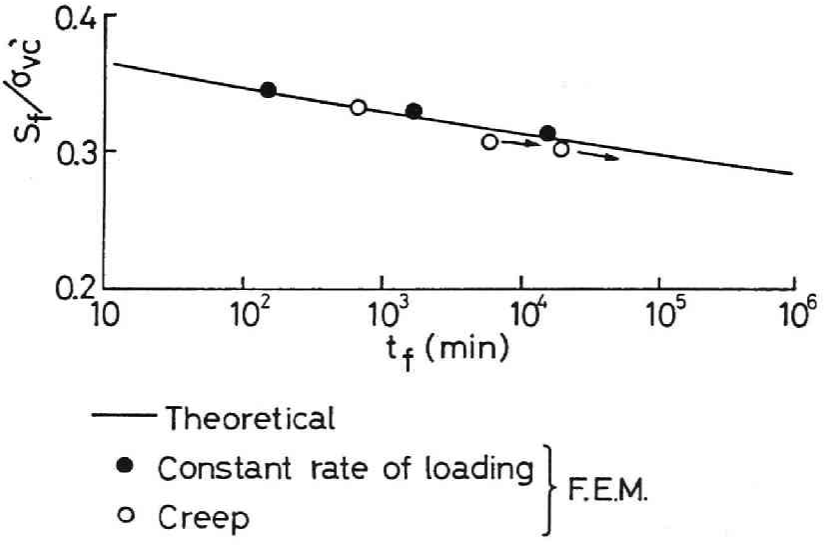

Fig. 8 Shear Strength Plotted against Durations of Loading

constant-rate-of-loading tests are also plotted, together with the theoretical s_f *versus* t_f curve based on *Eq. (4-5)*. It is seen that the results of finite element analysis for the constant-rate-of-loading tests are in good accordance with the theoretical relation. It is also seen that the reduction in shear stress observed in each of the constant-load creep tests has a remarkable consequence upon the occurrence of eventual failure. In order to see this more clearly, let us here imagine the situation where the shear stress is maintained at its initial value. Then, the creep rupture life, t_f, is able to be calculated by *Eq. (4-5)*, as summarized in *Table-4*.

Table-4 Variations in Shear stress during Sustained Loading and the Associated Variations in Creep Rupture Life

Sustained Loading Test	s/σ'_{vc}	t_f *(min.)*
A	0.345 → 0.327	138 → 1600
B	0.344 → 0.318	142 → 6500
C	0.343 → 0.311	175 → 20000

4-3-3-(3). Effect of Partial Consolidation on the Clay Behavior

The load settlement curve and a typical effective stress path for partially drained condition have been shown in *Fig. 5* and *6*, with the dotted lines. It is seen from *Fig. 6* that the increase in shear stress is accompanied by a gradual increase in mean effective stress. This behavior is noted to be quite different from those observed for the undrained cases where the mean effective stresses are reduced markedly during the loading stages. The effect of the partial consolidation on the load settlement behavior can be seen by comparing curve (4) with curves (1) through (3), all of which are drawn on *Fig. 4*. It is seen that the partial consolidation leads to a slower development of bearing capacity with increasing settlement, and at $\rho/B=3$ %, the partially drained bearing capacity barely reaches the levels of the undrained bearing capacity. The overall displacement fields, at $\rho/B=3$ %, under partially drained and undrained conditions are compared in *Fig. 9*. The comparison indicates that the partial consolidation tends to suppress the heaving or lateral displacements outside the loaded area. This suggests that the partial consolidation is

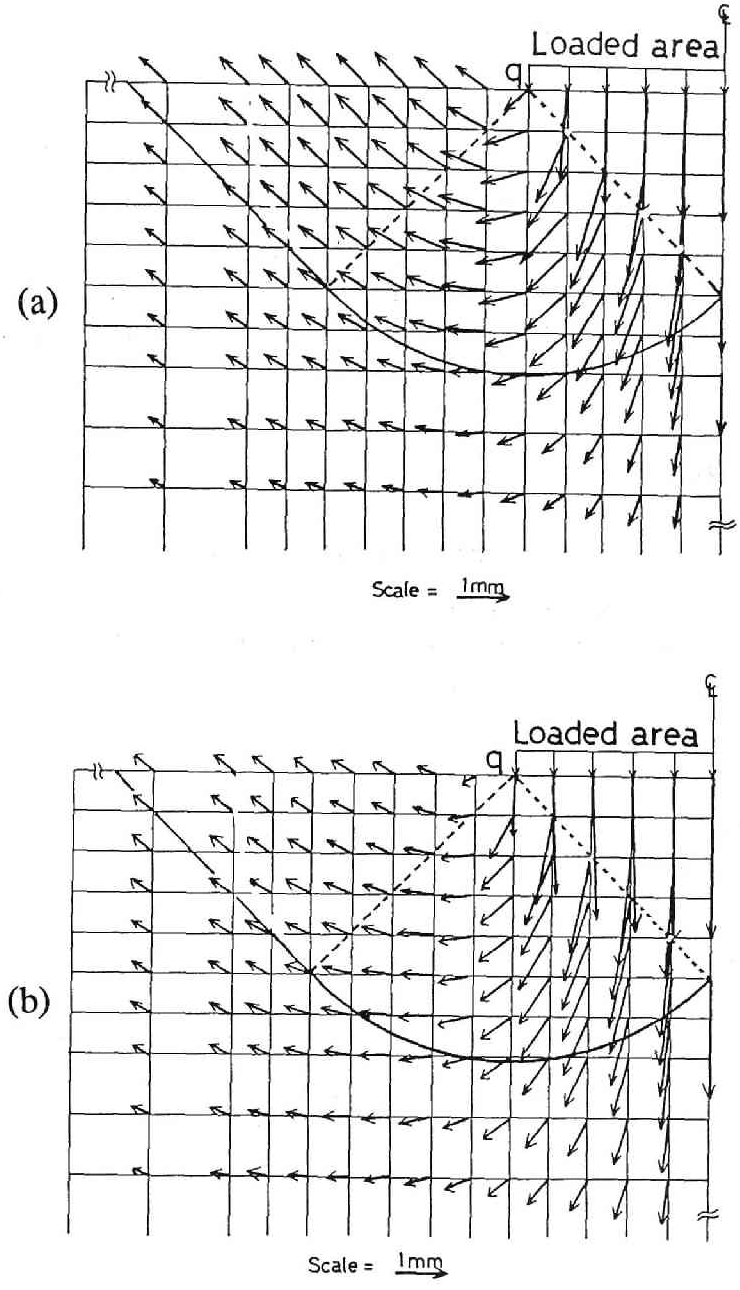

Fig. 9 Displacement Vectors at ρ/B=3%
(a) : Undrained Response, (b) : Partially Drained Response

favorable to the stability of the foundation clay. In this respect, remember the increased effective stresses due to the partial consolidation (see *Fig. 5*). It is also remarked here that a closer examination of the load settlement curve for the partially drained case indicates a reduced bearing capacity at a given value of ρ/B (see *Fig. 4*). In view of the results stated above, it may be concluded that care should be taken in assessing the effect of partial consolidation, as far as the overall performance of the structure-foundation system is concerned. Detailed study on the assessment of the effect of partial consolidation on the deformability of the clay foundation is explained in Chapter 8 with emphasis on the lateral ground movement.

4-4. Conclusions

A series of coupled stress-flow analysis for the bearing capacity and plastic flow of a rate-sensitive, saturated clay have been made using the method of finite elements. The principal conclusions drawn from these analyses are summarized as follows.

(1) The undrained bearing capacity of the clay foundation increases with increasing loading rate, in accordance with the associated increase in the shear strength of the clay element. Indeed, the bearing capacity factor, N_C, remains at a practically constant value irrespective of the loading rate.

(2) Remarkable redistribution of stress occurs within the foundation clay undergoing creep under constant loads. This phenomenon prolongs the moment of possible failure of the foundation clay much more, as compared the fictitious case where the shear stress in the soil mass would have been maintained constant during the creep process.

(3) Occurrence of the partial consolidation during the loading stage is favorable to the stability of the foundation clay itself. However, it should be kept in mind that such partial consolidation is accompanied by a remarkable increase in settlement at a given load, as compared with the undrained loading. Therefore, the assessment of the effect of

partial consolidation should be made regarding the overall performance of the structure-foundation system.

REFERENCES

(1) Akai, K. and T. Tamura (1976) : An Application of Nonlinear Stress-Strain Relations to Multi-Dimensional Consolidation Problems, Annuals D.P.R.I., Kyoto Univ., No.21 B-2, pp.19-35 (in Japanese).

(2) Casagrande, A. and S.D. Wilson (1951) : Effect of Rate of Loading on the Strength of Clays and Shales at Constant Water Content, Geotechnique, Vol.2, pp.251-263.

(3) Christian, J.T. (1968) : Undrained Stress Distribution by Numerical Methods, Journal of the Soil Mecanics Division, ASCE, Vol.94, No. SM6, pp.1333-1345.

(4) Leroueil, S., F. Tavenas, F. Brucy, P. La Rochelle and M. Roy (1979) : Behavior of Destructed Natural Clays, Journal of the Geotechnical Engineering Division, ASCE, Vol. 105, No. GT6, pp.759-778.

(5) Sekiguchi. H. (1977) : Rheological Characteristics of Clays., Proc. 9th ICSMFE, Tokyo, Vol. 1, 1977, pp.289-292.

(6) Sekiguchi. H. (1983) : Applicability of the Plane-strain Viscoplastic Model for Clay, Proc. Annual Conf. of Chubu Brance, JSCE, pp.342-343.

(7) Sekiguchi, H. (1984) : Theory of Undrained Creep Rupture on Normally Consolidated Clay Based on Elasto-Viscoplasticity, Soils and Foundations, Vol. 24, No. 1, pp.129-147.

(8) Sekiguchi. H., Y. Nishida and F. Kanai (1982) : A Plane-strain Viscoplastic Constitutive Model for Clay., Proc. 37th National Conf., JSCE, pp.181-182 (in Japanese).

(9) Shibata, T. and H. Sekiguchi (1980) : A Method of Predicting Failure of Embankment Foundation Based on Elasto-Viscoplastic Analyses, Proc. of JSCE, No. 301, pp.93-104 (in Japanese).

CHAPTER 5

Conclusions

The major conclusions obtained from the present research is summarized as follows:

In chapter 2, predictive capability of the existing constitutive models are discussed. Intrinsic characteristics of the natural clay under almost static condition are well described by Cam clay model and Pender model, whereas modified Cam clay model tends to overestimate the shear strength. Then it can be concluded that undrained static behavior of clay can be described by the existing elasto-plastic constitutive models to some extent. Both Adachi and Oka model and Sekiguchi model can describe the strain rate dependency of strength of the natural clay under the undrained triaxial condition. And adding that, stress strain relations and effective stress paths are well predicted by these models. Therefore, it can be concluded that the rate-sensitive properties of natural clay can be estimated by the existing elasto-viscoplastic constitutive models.

In chapter 3, theoretical structures of the elasto-viscoplastic constitutive models are investigated, with emphasis on the description of undrained creep rupture. First of all, it is mathematically proved that the overstress model cannot describe the acceleration creep and the subsequent undrained creep rupture due to its theoretical structure. Then, two kinds of trials are introduced to overcome these deficiencies; (1) introduction of the deterioration effect of the clay structure and (2) introduction of the concept of the non-stationary flow surface.

Considering the deterioration effect of clay, Adachi and Oka model, a typical overstress elasto-viscoplastic constitutive model, has been modified to describe acceleration creep and creep rupture phenomena. Analytical solution of undrained strength, q_f, for the model is derived as a

function of strain rate, $\dot{\varepsilon}$, and the viscoplastic parameter, C. Since the viscoplastic parameter, C, that is originally assumed to be constant, varies with decreasing in the mean effective stress during the undrained creep, the relation between the viscoplastic parameter, C, and the stress ratio, (M-q/p') is formulated based on the experimental findings. By introducing this relation, the overstress elasto-viscoplastic constitutive model has been modified to be able to describe the acceleration creep and creep rupture phenomena.

The structures of the non-stationary flow surface model are characterized by the stress rate effect. The overstress model can be derived from the non-stationary flow surface model, by ignoring the stress rate term. Then, numerically calculated creep rupture life by the adapted overstress model underestimates that by the original non-stationary flow surface model. The effect of the stress rate, $\dot{f}$,is little on the performance of the constitutive equations, because the contribution of the overstress term is predominant. Finally, it is shown that these two types of models, non-stationary flow surface model and overstress model, have common theoretical structures as far as the overstress term is concerned.

In chapter 4, the plane-strain version of the non-stationary flow surface elasto-viscoplastic constitutive equations are formulated to the finite element analysis, and applied to the coupled stress flow analysis for the bearing capacity and plastic flow of a rate sensitive, saturated model clay foundation. It is investigated that the bearing capacity factor, N_C, is almost constant and independent of loading rate, whereas the bearing capacity of clay foundation becomes larger with increasing rate of loading.

Partial consolidation takes place even during the loading stage with a appreciable increase in settlement comparing with undrained loading. Though the discussion on the effect of the partial consolidation on the deformation characteristics of clay foundation based on the intrinsic characteristics of the constitutive equations are of academic interest, nonetheless, in practice this effect should be given due consideration..

CHAPTER 6

Introduction

6-1. General Remarks

Deformation of the foundation ground is strongly influenced by the following three factors; that is to say, geometrical condition of the foundation, the physical properties of the materials and loading sequence. While the theoretical structures of the constitutive models are discussed in Part 1, with emphasis on the basic characteristics of the models which govern the behavior of soil element, in Part 2, universal evaluation of the deformation of the the foundation ground will be discussed, subjected to construction of the embankment, revetment, reclaimed land and breakwater. Generally, deformation and stability of soft clay layers sedimented shallow in the foundation ground become an issue. It is completely reasonable, considering the magnitude and loading level of the structures. For a small-scale structure, the foundation ground can be maintained safe by making the shear deformation keep in harmony with a gain in strength due to consolidation. However, with the development of coastal areas, offshore immense reclamation or breakwater construction in the deep sea have been increased. For such large-scale structures, not only increase in stress in the alluvial clay layer, but also stress propagation into deeply sedimented layers will cause the serious problems. Beside having an eye on the bearing capacity or shear deformation of the foundation as usual, attention should be paid to the delayed deformation subjected to occurring of the plastic yielding of deep overconsolidated clay.

Vertical drain methods are prevailing to promote consolidation for the thick alluvial clay layer. Furthermore, when immense structure is constructed with a strict control of deformation, soil improvements for clay foundation should be performed. For example, column of densely compacted sand (*SCP*), deep mixing method (*DMM*) or piles are equipped

in order to avoid the unfavorable deformation. Soil improvements are usually equipped as a counterpart for the superstructure load. Then, stress condition of the foundation ground and the induced deformation can not avoid being inhomogeneous and complicated. The traditional method for the deformation prediction is, however, mainly based on the theory of one-dimensional consolidation. Therefore, it is almost helpless to the problems, containing lateral ground movement, stress concentration due to soil improvement, multi-dimensional drainage effect and so forth. Therefore, the sophisticated method must be established in order to evaluate these aforementioned compound geotechnical problems.

In Part 2, various geotechnical problems of clay foundation will be investigated by using the finite element method, into which the elasto-viscoplastic constitutive equations are incorporated. In Part 1, the theoretical structures of the elasto-viscoplastic models are discussed within the framework of isotropically consolidated triaxial compression. It is a matter of great academic interest to be sure, but we should pay attention to the fact that the practical geotechnical events are usually managed under K_0 condition. Exact evaluation of the initial stress state of the foundation, in terms of K_0 value, directly leads to the reliable assessment for ground deformation. Then, in Part 2, because of its predicting capability for K_0 value at rest, the plane-strain version of the elasto-viscoplastic constitutive model will be used to analyze the ground deformation, without changing the framework of its viscoplastic features (refer to chapter 4 in Part 1). Emphasis is paid on the establishment of the rational method to predict the deformation of the foundation ground, with being conscious of the aforementioned three factors, that is, the geometry of the foundation, the material properties and the loading sequence.

6-2. Scope of the Study

In chapter 7, evaluation of lateral ground movement of a clay foundation is discussed, keeping the effect of the partial drainage in mind. Considering the significance of delayed lateral ground movement which takes place with settlement, a new index, soil volume ratio; V_δ/V_ρ is

introduced to assess the lateral ground movement quantitatively. Then, it is also stated that the local geological characteristics of the foundations have much influence on the deformation pattern, by comparing the actual results of the lateral ground movement in the world.

In chapter 8, deformation analysis of the reclaimed marine foundation is performed, exemplifying the Koshien reclaimed land constructed in Osaka Bay. Sand drains were driven beneath the rubble revetment and a large amount of sand was dumped on the alluvial clay deposit. Settlement and lateral displacement of the diluvial layers as well as these of the alluvial clay layer are numerically analyzed, and the generation/dissipation process of the excess pore water pressure due to filling is also calculated. Then, comparing these calculated performances with the *in situ* observed results, the accuracy of the deformation prediction by the proposed method in terms of the elasto-viscoplastic finite element method is confirmed.

In chapter 9, deformation and stability of the marine foundation subjected to the composite breakwater construction are analyzed using the elasto-viscoplastic finite element method. The South Breakwater of the New Nagasaki Fishing Port, damaged by the typhoon in 1987 is exemplified here. First of all, discussions are performed for the control of deformation by the soil improvement (*SCP*), equipped beneath the caisson walls. Then, the stability control of the breakwater foundation is managed by calculating and monitoring the settlement and lateral displacement profiles during the breakwater construction, because large deformation has been predicted to occur, due to the wave dissipating blocks setting. The calculated performances are found to describe qualitatively the observed deformations. However, at the same time, difficulty of the observation for offshore construction was brought in relief.

In chapter 10, the major conclusions obtained from the present study have been summarized.

CHAPTER 7

Effects of Partial Drainage on the Lateral Deformation of Clay Foundations

7-1. Introduction

The problem of lateral deformation of soft foundations under embankments and coastal fills has had increasing attention. A unique feature of the problem lies in that it relates not only to the problem of contained plastic flow or ground failure, but also to the problem of multi-dimensional consolidation. This means that classical soil-mechanics approaches, in terms of the method of limit equilibrium or the oedometric method of consolidation are almost invalid for the problem of predicting lateral soil movements. Another interesting feature of the problem stems from the geological background of alluvial deposits. That is to say, the layered nature of such soil deposits exerts a profound influence on the pattern and even magnitude of the lateral deformation that develops when the deposit is loaded by an embankment or a coastal fill.

Finite element analysis has been introduced to estimate the lateral ground movement numerically and have produced results to some extent. However, considering the modeling of the foundation ground, serious discrepancy exists between the model foundation ground concisely assumed for numerical analysis and the natural deposits that potentially have inclined or undulated bedding strata, sand seam or sand lense inside thick clay layers. Unfortunately, this heterogeneity has remarkable effect on the pattern and the magnitude of lateral ground movement. With these reasons, as well as difficulty of estimation of the physical properties of the ground materials and modelling of actual loading process, lateral ground movement is so hard to be quantitatively predicted even by using the detailed numerical analysis.

In this chapter, a rational framework for assessing lateral deformations of embankment foundations is investigated. For this purpose, results from elasto-viscoplastic consolidation analyses in terms of the method of finite elements will be presented in chart form. Emphasis will be placed on quantifying the effects of embanking speed or partial drainage upon the lateral soil movements. Then the effect of stratification of natural soil deposits on lateral ground movement characteristics is substantiated by systematically completing the *in situ* performances for the test embankments, and the lateral deformability of the clay deposits is also discussed.

7-2. Elasto-Viscopastic Finite Element Analysis

The elasto-viscoplastic constitutive model used in this paper was proposed by Sekiguchi (1977). Sekiguchi *et al.*(1982) modified the model to a plane-strain version. The viscoplastic flow rule for the model is generally expressed as

$$\dot{\varepsilon}_{ij}^{p} = \Lambda \frac{\partial F}{\partial \sigma_{ij}'} \tag{7-1}$$

in which F is the viscoplastic potential and Λ is the proportional constant. Viscoplastic potential F is defined as follows:

$$F = \alpha \cdot \ln \left[1 + \frac{\dot{v}_0 \cdot t}{\alpha} \exp\left(\frac{f}{\alpha}\right)\right] = v^p \tag{7-2}$$

in which a is α secondary compression index, v_0 is the reference volumetric strain rate, f is the function in terms of the effective stress and v^p is the viscoplastic volumetric strain. The concrete form of the model is shown in the previous chapter. The resulting constitutive relations are implemented into the finite element analysis procedure through the following incremental form:

$$\{\Delta\sigma'\} = [C^{ep}]\ \{\Delta\varepsilon\} - \{\Delta\sigma^R\} \tag{7-3}$$

Where $\{\Delta\sigma'\}$ and $\{\Delta\varepsilon\}$ are the associated sets of the effective stress increments and the strain increments respectively, and $[C^{ep}]$ stands for the elasto-viscoplastic coefficient matrix. The term $\{\sigma^R\}$ represents a set of 'relaxation stress' which increases with time when the strain is held constant. The pore water flow is assumed to obey isotropic Darcy's law. In relation to this, it is further assumed that the coefficient of permeability, k, depends on the void ratio, e, in the following form:

$$k = k_0 \cdot \exp\left(\frac{e - e_0}{\lambda_k}\right) \tag{7-4}$$

in which k_0 is the initial value of k at $e=e_0$ and λ_k is a material constant governing the rate of change in permeability subjected to a change in the void ratio.

7-3. Framework for Assessing Lateral Soil Movements

7-3-1. Basic Parameters

Consider a long embankment constructed on the bed of soft clay (*Fig. 1(a)*). The base width of the fill and its height from the ground surface are denoted by B and h. The thickness of the soft foundation is denoted by H. Due to the weight of the fill, the foundation block immediately below the fill will deform in a manner such as shown in *Fig.1(a)*. Here, ρ_{CL} represents the surface settlement at the center of the embankment, V_ρ represents the volume lost in settlement and V_δ stands for the volume gained in lateral displacement. The lateral displacement, δ will hereafter be taken as positive when it is directed away from the embankment. The net reduction in the volume of the foundation block may be expressed as $V_{net} = V_\rho - V_\delta$. This may also be expressed in the following dimensionless form:

$$\frac{V_{net}}{V_0} = \frac{V_\rho - V_\delta}{V_0} \tag{7-5}$$

Here, V_0 is the volume of the foundation block per running meter. Note that those volumetric parameters defined above will be used below to quantify the overall degree of partial drainage of soft foundations.

It is also convenient for later discussion to define the maximum value in a given, vertical profile of lateral displacement at or very near the toe of the embankment (see *Fig.1(b)*). In this paper such a local maximum of the lateral displacements is denoted by δ_m.

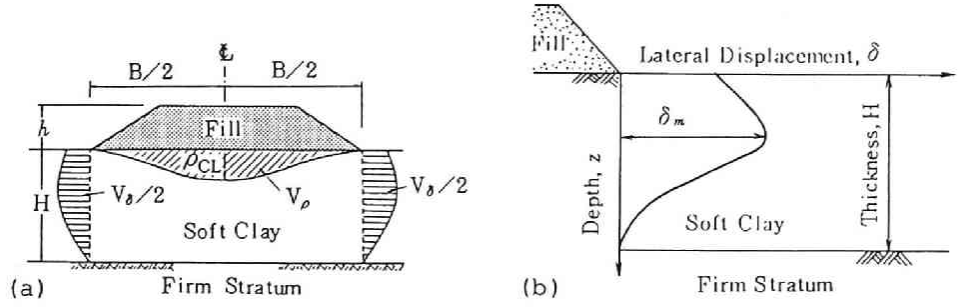

Fig. 1 Cross-section of an Embankment Foundation System together with Principal Symbols Indicated

7-3-2. Distribution of Lateral Displacements

The distribution of lateral displacements within an embankment foundation at a given time is best illustrated in the form of contours of equal lateral displacement. Such an example is given in *Fig. 2*. The results are based on a coupled stress-flow analysis using the method of finite elements, in which a plane-strain version (Sekiguchi *et al.*, 1982) of the elasto-viscoplastic constitutive model for clay (Sekiguchi, 1977, Sekiguchi *et al.*, 1981) stated in the previous section, is implemented. Only the right-hand side of the embankment-foundation system is shown in *Fig. 2*, in view of the symmetry of the system considered. Note that the largest lateral displacement occurs at point *A*, below the approximately midside of the slope. Consider next a vertical line through point *B*, running in close proximity to the toe of the embankment. In this particular profile, the lateral displacements take a local maximum, δ_m, at a point just exemplified by point *B*. It is noteworthy that such a particular maximum, δ_m,

approximates numerically to the largest lateral displacement such as exhibited at point *A*.

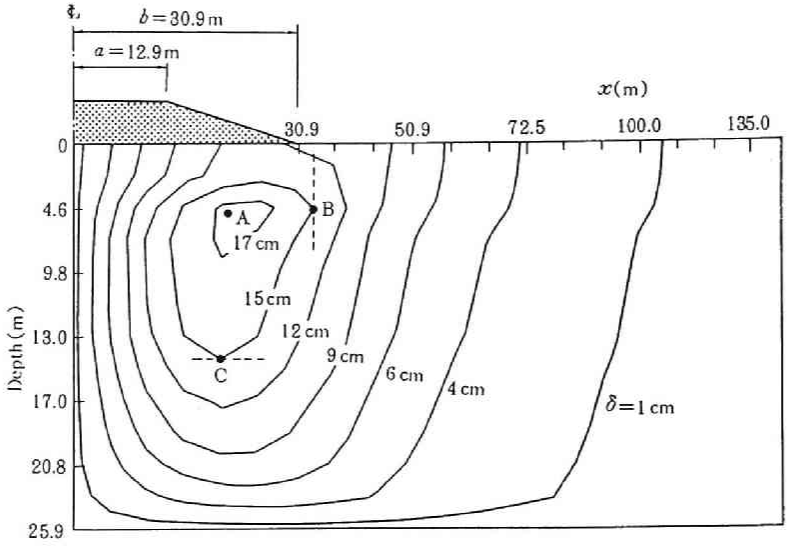

Fig. 2 Calculated Contours of Equal Lateral Displacement

In *Fig. 2* it should also be noted that a local maximum of another kind is realized at point *C*. That is to say, the following relation holds at point *C*:

$$\varepsilon_h = \frac{\partial \delta}{\partial x} = 0 \tag{7-6}$$

Here, ε_h is the horizontal strain and x denotes the horizontal co-ordinate. Thus the lines joining such points as *A* and *C* represent the loci of zero lateral strain, inside which the lateral strains are expansive and outside which the lateral strains are compressive. A series of related finite-element analyses suggest that a workable expression for the loci of zero lateral strain is as follows:

$$x = (a^2 + b^2)^{1/2} \tag{7-7}$$

where a is the half of the crest width of the embankment and b is the half width at the embankment base.

It should be mentioned here that the *Eq.(7-7)* is obtained by referring to the corresponding expression for the semi-infinite, undrained, elastic body subjected to embankment loading. Namely, the loci in the case of an undrained elastic ground take the following analytical form:

$$x^2 - z^2 = \frac{a^2 + b^2}{2} \tag{7-8}$$

where a and b are the shape parameters for the embankment loading (see *Fig. 3*). There are some factors invalidating *Eq.(7-8)* for more realistic ground conditions. Theses include the presence of a rigid base or firm strata below the clay bed as well as the occurrence of partial drainage even during construction stage. Note that the just mentioned is the background of suggesting *Eq.(7-7)* for realistic soil conditions.

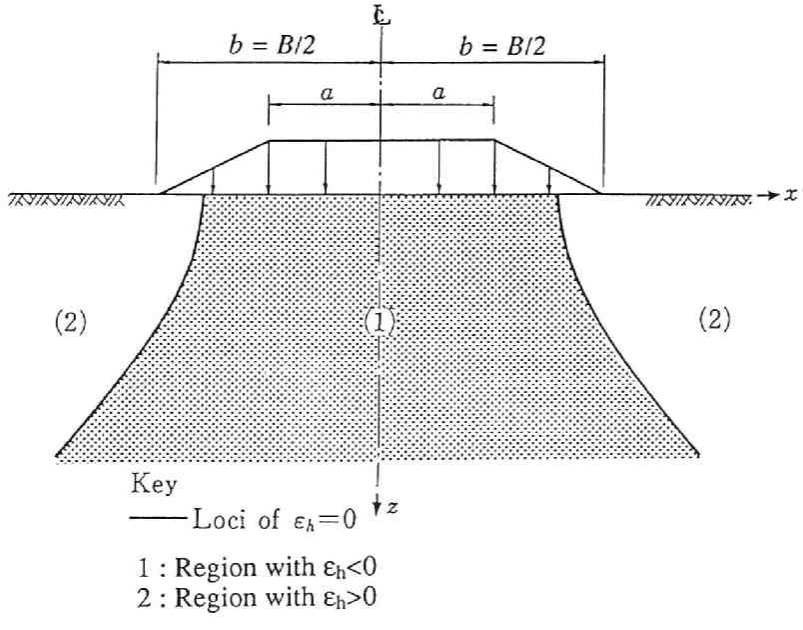

Fig. 3 Loci of Zero Strain in a Semi-Infinite Undrained Elastic Body

7-3-3. Partial Drainage as Affected by Embanking Speed

The purpose of this section is to relate the partial drainage of a clay foundation to the embanking speed as well as the consolidation capability of the clay foundation.

Consider that an embankment is constructed on a homogeneous bed of clay at a constant rate of loading, q, to a prescribed intensity of loading, q_{ec}, and thereafter it is left to stand at that constant load intensity. In general, the degree of partial drainage within the clay foundation depends on the rate of loading relative to its consolidation or drainage capability. It is appropriate herein to introduce a time factor, T_{ec}, as being such a rate parameter. That is to say,

$$T_{ec} = \frac{c_v \cdot t_{ec}}{H_d^2} \tag{7-9}$$

where t_{ec} is the elapsed time to the end of construction of the embankment from its commencement of embanking, c_v is the coefficient of (one-dimensional) consolidation of the clay foundation and H_d is the maximum length of drainage of the clay foundation.

The next thing to do is to define the overall degree of drainage of the clay foundation in terms of a relevant measure. For this purpose, we introduce the following parameter:

$$U_v(t) = \frac{V_{net}(t)}{V_{net\,f}} \tag{7-10}$$

Here, $U_V(t)$ stands for the degree of consolidation at any instant of time, t, in terms of the net volume-changes of the foundation block discussed in *Fig. 1(a)*, and $(V_{net})_f$ denotes the final, net volume-changes that are reached if the intensity of loading is maintained at $q = q_{ec}$ after the end of construction The physical meaning of the new parameter U_v can clearly be seen from *Fig. 4*. Here, the normalized volume-changes gained in lateral deformation are drawn against the normalized volume-changes lost in

settlement after the stoppage of four different rates of embanking. The B/H ratio involved is equal to 2, and the load level adopted is equal to $q_{ec}/\sigma_{vc}'=1.8$, where σ_{vc}' is the vertical consolidation pressure. The broken lines on this figure schematically show the behavior during the construction stage. Note that the performance with $T_{ec} = B$ stands for the perfectly drained performance, and this is computationally realized here by rendering the coefficient of permeability, k, of the foundation clay infinitely large in value. It is seen that in this particular example, all the final points fall on the line of $V_{net}/V_0 = 5$ %, irrespective of the T_{ec} value. This is a direct consequence of the present constitutive model and is compatible with what has been observed for many clays (Schofield and Wroth, 1968). It is thus logical to define the degree of consolidation in terms of the net volume-changes in the form of *Eq.(7-10)*. Indeed, the lines of equal U_v in *Fig. 4* are drawn on the basis of the above reasoning.

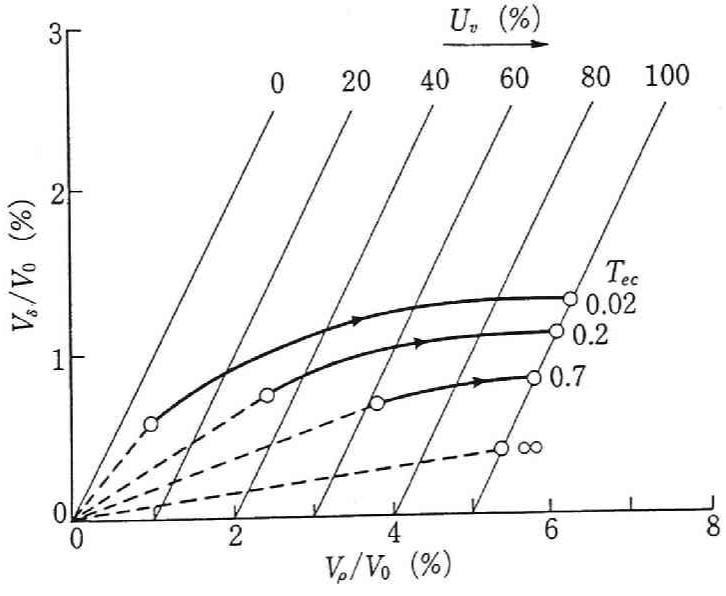

Fig. 4 Calculated Performance of Displacement Volumes

Let $(U_v)_{ec}$ be the degree of elasto-viscoplastic consolidation at the end of construction, in the sense stated above. The calculated relationship between $(U_v)_{ec}$ and the corresponding time factor, T_{ec}, for the B/H ratio of

2 is shown in *Fig. 5*. Note that calculations at other B/H ratios of *3*, *4* and *6* yield curves essentially the same as in the case of $B/H=2$, although they are omitted on *Fig. 5* for brevity. Instead, the theoretical relationship between the end-of-construction degree of consolidation and the time factor obtained by Lumb (1963) within the framework of one-dimensional elastic consolidation is presented in *Fig. 5*. It is of interest to note that both curves are remarkably similar despite their totally different sets of assumptions.

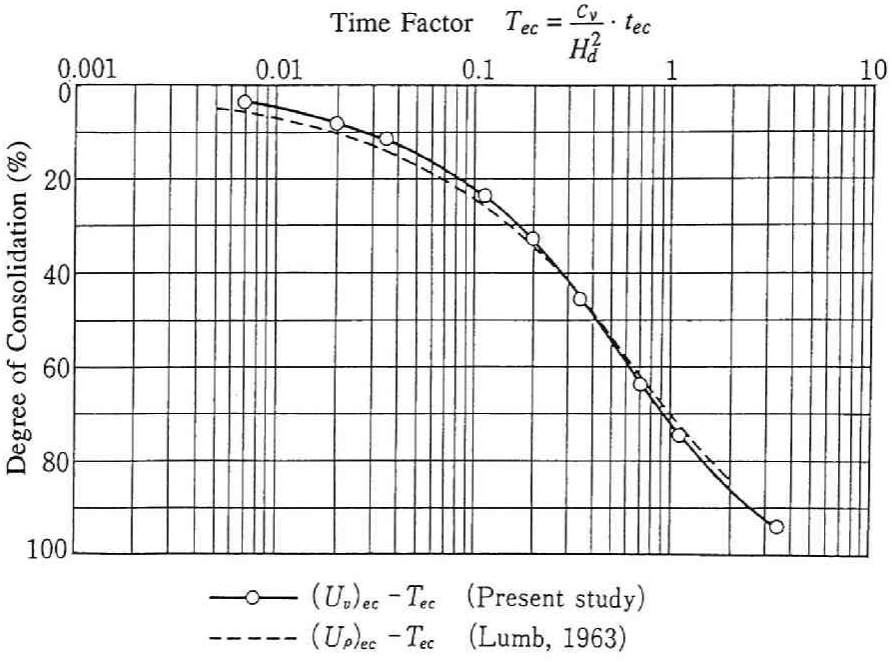

Fig. 5 Calculated Relationship between the Degree of Consolidation and the Time Factor

7-3-4. Effects of Partial Drainage on Lateral Soil Movements

The calculated effects of partial drainage (or embanking speed) on the lateral soil movements can be summarized in the form of *Fig. 6*. Here, the ratios of the volume gained in lateral deformation to the volume lost in settlement at the end of construction, are drawn against the corresponding degrees of consolidation in terms of the net volume-changes of the foundation blocks with B/H ratios of *2*, *3*, *4* and *6*. It is seen that for a

given B/H ratio, the lateral deformation develops more rapidly as the degree of consolidation in terms of the net volume-changes, $(U_v)_{\varepsilon\chi}$ is less than 30%.

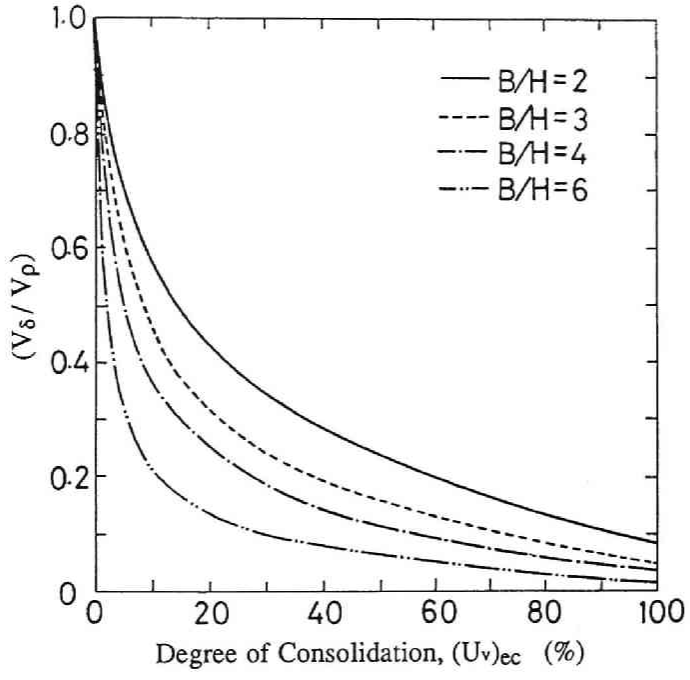

Fig. 6 Ratio of Displacement Volume Plotted against the Degree of Consolidation

From *Fig. 6* it is also noted that for a given value of $(U_v)_{ec}$, the lateral deformation tends to be suppressed with increasing B/H ratio, except for the undrained case where the value of V_δ/V_ρ is always unity by definition.

7-4. Performances of Lateral Deformation in Natural Soil Deposits

7-4-1. Introductory Remarks

The performances of lateral deformation in natural soil deposits are discussed in this chapter. The underlying idea is that the variety of soil-

forming processes is well reflected in the stratification of each deposit as well as in the nature of the constituent soils.

Let us first make a brief review of the case histories compiled by Tavenas *et al.* (1979). From the information given in their *Table 1*, we take up the lateral deformability factors, $(\delta_m/H)_{ec}$, for a total of *21* embankments and depict them in the form of *Fig. 7*. Here, δ_m is the maximum lateral displacement in a vertical profile through the toe of a given embankment, H is the thickness of the soft foundations and the subscript, *ec*, means the end of construction, as defined before. We classify the status of each embankment as follows: "Constructed to failure" or "Very close to failure" or "Stable", on the basis of the description by Tavenas *et al.* (1979) and the related references. Also, we arrange all the

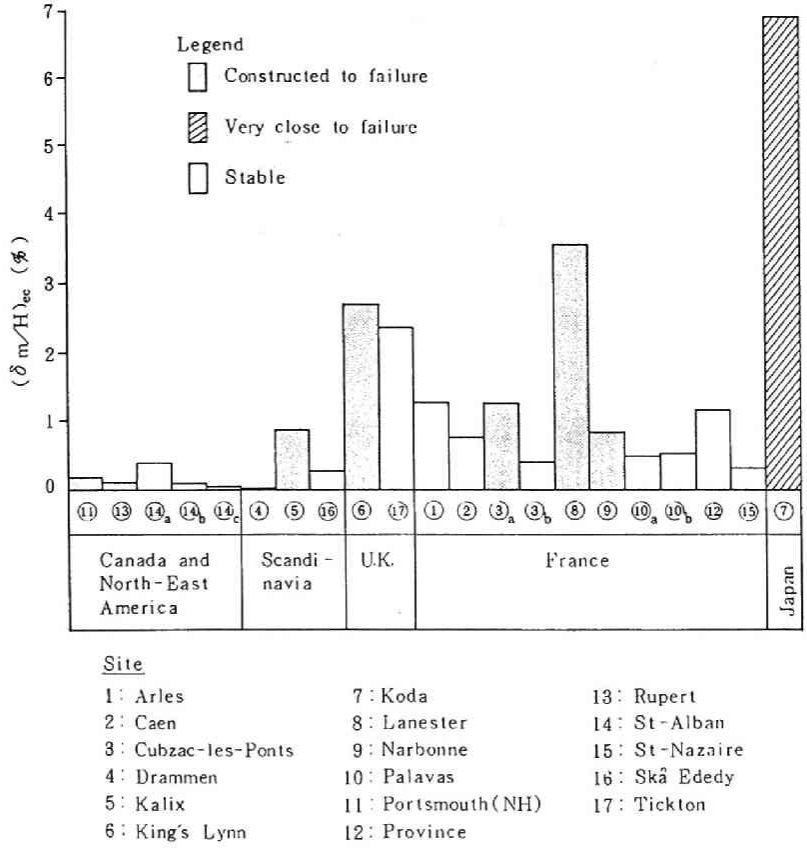

Site

1 : Arles	7 : Koda	13 : Rupert
2 : Caen	8 : Lanester	14 : St-Alban
3 : Cubzac-les-Ponts	9 : Narbonne	15 : St-Nazaire
4 : Drammen	10 : Palavas	16 : Skå Ededy
5 : Kalix	11 : Portsmouth(NH)	17 : Tickton
6 : King's Lynn	12 : Province	

Fig. 7 Lateral Deformability Factor at 17 Test Sites

embankments in five groups, in view of the construction sites on a global scale. It is then clear that the case histories covered are concerned with rather restricted regions in the world. Care should be taken in this regard, however, that the apparent trend would be owing principally to the availability of the published case histories. In other words, the trend encourages us to collect more information from sources effective in the other regions as well.

Another aspect to be noted in *Fig. 7* is the scope in deformability. At the one extreme, the koda test embankment (*site 7*) exhibits the lateral deformability factor as high as *7%*. In contrast, the Portsmouth test embankment (*site 11*) has the lateral deformability factor as low as *0.17%*, although it was brought to eventual failure. Such a remarkable difference in the lateral deformability seems to come primarily from the difference in the nature of the soil deposits. In the following sections this interesting aspect will be discussed fully.

7-4-2. The Deposits of Soft Soils Selected

A total of nine deposits of soft soils are selected for the present discussion. Their sources of information are summarized in *Table 1*, together with the principal data on the embankments constructed on the deposits. The columnar sections below the ground level are shown in *Fig. 8*, relative to the mean sea level (*M.S.L.*). Columnar section 1 represents a

Table-1 Summary of the Nine Deposits of Soft Soils Selected

Column. Sec. No.	Site	Nation	B (m)	H (m)	Source of Data
1	Koda	Japan	24	6.0	Muromachi & Watanabe (7)
2	Ebetsu	Japan	63	28.9	J.H.P.C. (8)
3	Atchafalaya Levee	U.S.A.	72	36.0	Kaufman & Weaver (9)
4	Rio de Janeiro	Brazil	40	11.3	Ramalho-Oritigao et al. (10)
5	River Thames	U.K.	47	12.0	Marsland & Powell (11)
6	Cubzac-les-Ponts	France	43	9.0	Magnan et al. (12)
7	Portsmouth	U.S.A.	71	13.4	Ladd (13)
8	Boston	U.S.A.	71	45.6	Lambe (14)
9	Kanda	Japan	62	23.3	J.H.P.C. (15)

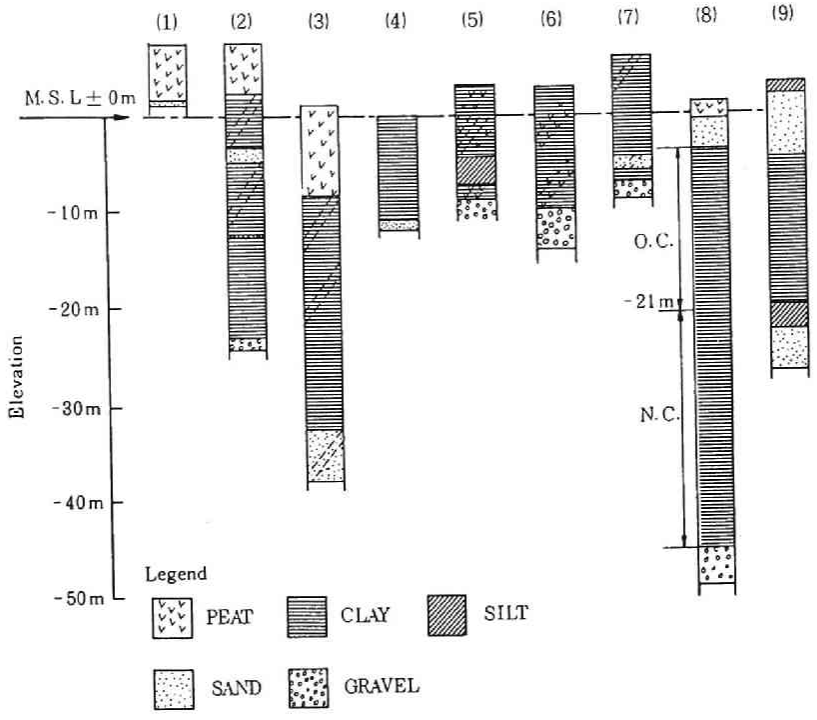

Fig. 8 Stratification of the Soil Deposits Selected

borehole log that was taken from a small-scale deposit of peat located between hills. Columnar sections 2 and 3 both feature the large-scale lowlands, in which there exist the thick beds of soft clays overlain by the highly compressible peats. Columnar sections 4, 5 and 6 indicate the deposits of soft, slightly organic clays, with clay crusts Columnar section 7 is drawn for the deposit of the highly sensitive clay that was presumably subjected to leaching. Columnar section 8 features the very thick bed of Boston blue clay (Lambe, 1973, D'Appolonia *et al.*, 1971). Note that the upper half of the blue clay is overconsolidated to unusually high extents, compared with an ordinary deposit of alluvial clay (*Fig. 9*). Indeed, the presence of the sandy glacial till below the blue clay is revealing concerning the process of formation of this particular deposit. Columnar section 9 in *Fig. 8* depicts a borehole log that was taken from a past drowned valley (marked *C* on *Fig. 10*), in the Kanto district, Japan (The Japan Highway Public Corporation, 1981, Endo *et al.*, 1983). Note that in this deposit the thick bed of marine clay is overlain by the naturally

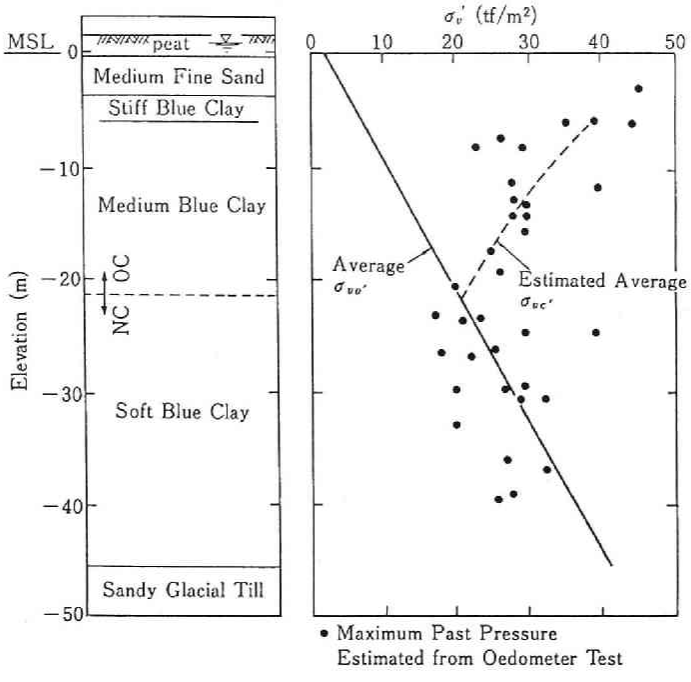

Fig. 9 Distribution of Soil Properties at the Boston Test Site (D'Appolonia et al.)

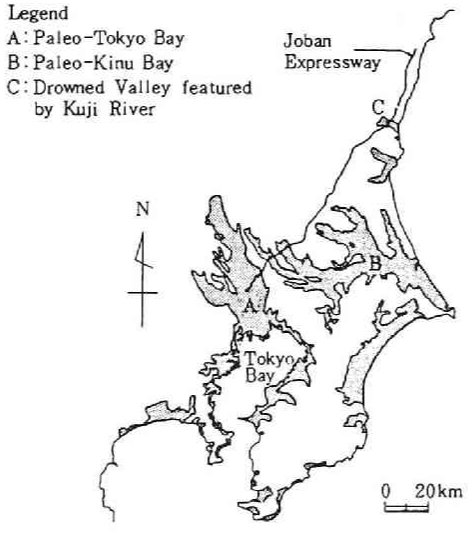

Fig. 10 Drowned Valleys at 6000 Years B.P. in the Kanto District, Japan (Endo et al.)

sedimented sand. It will thus be evident that the soil deposits selected here cover a comprehensive range of alluvial deposits of clays and peats.

7-4-3. The Stress-Deformability Performances and Discussion

7-4-3-(1). Pressure-Deformability Curves

The performances of the eight deposits loaded by the embankments are shown in *Fig. 11*. Here, the observed maximum lateral displacement in a vertical profile through the toe of each embankment is plotted against the applied load intensity for the construction phase. For the Ebetsu test embankment, the performance during the holding period and the second filling stage is also indicated. The performance of the Atchafalaya levee is not shown in *Fig. 11*, because it was concerned solely with the test raising of the existing bank and the preceding lateral soil movements due to the

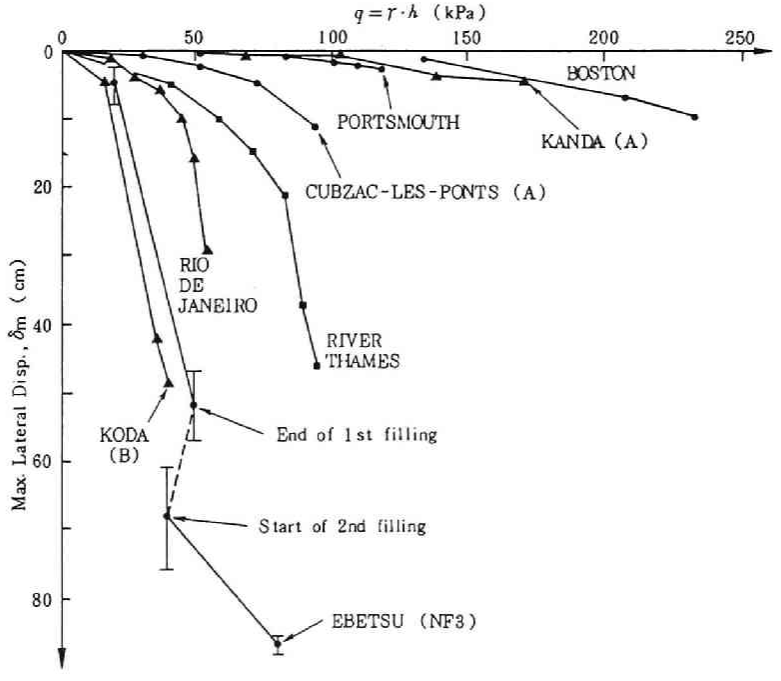

Fig. 11 Load - Maximum Lateral Displacement Curves for Eight Deposits

existing bank were not reported in the literature (Kaufman and Weaver, 1967). By closely examining the pressure-deformability curves in *Fig. 11* in the light of the soil profiles shown in *Fig. 8*, we can come to a conclusion that those pressure-deformability curves well reflect the nature of the soil deposits concerned.

7-4-3-(2). Practical Implications

The pressure-deformability curves shown in *Fig. 11* include those from the four test embankments that were actually brought to failure: Rio de Janeiro (Ramalho-Ortigao *et al.*, 1983); River Thames (Marsland and Powell, 1977); Cubzac-les-Ponts (A) (Magnan *et al.*, 1983); and Portsmouth (Ladd, 1972). In the case of the Rio de Janeiro test embankment as well as the River Thames test bank, the stiffness factor, $\Delta q/\Delta\delta_m$, tends to decrease remarkably with increasing intensity of loading, q until the eventual failure of the embankment is reached. This immediately suggests that for these particular kinds of soft deposits, the monitoring of lateral soil movements is an effective means for identifying the impending failure of the embankment-foundation system.

The above statement can be reinforced from *Fig. 12*, which indicates the reported degradation in overall stiffness of the soft foundations below the River Thames test bank (Marsland and Powell, 1977, Shibata and Sekiguchi, 1980). Note here that the test bank was brought to failure by regularly placing 0.33 meter-thick lifts at one-day intervals (Marsland and Powell, 1977). The resulting increment in lateral displacement, $\Delta\delta$, over

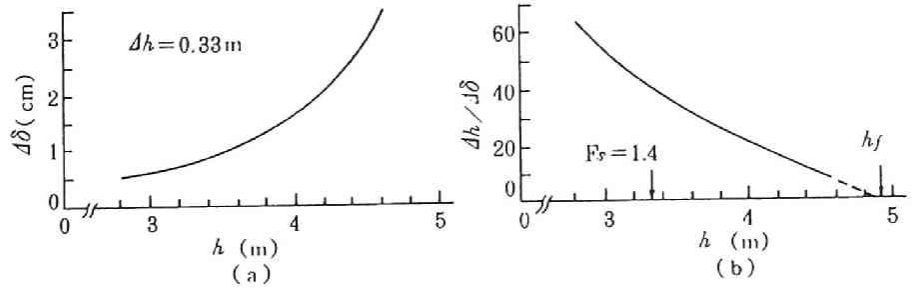

Fig. 12 Performance of the River Thames Test Bank

that one-day interval is indicated in *Fig. 12(a)* as a function of the height of the bank, h, from the original ground level. The associated relationship between the stiffness factor, $\Delta h/\Delta\delta$, and the fill height, h, is shown in *Fig. 12(b)*, after Shibata and Sekiguchi (1980). It is seen that at higher levels of loading the stiffness factor, $\Delta h/\Delta\delta$, tends to decrease linearly with increasing height of the bank, h, thus enabling one to assess the failure height, h_f, in advance of the eventual failure (Shibata and Sekiguchi, 1980).

Such an observational procedure of failure prediction does not seem to be applicable, however, to deposits of brittle nature. A case-history implying this is with the Portsmouth test embankment that was built on the highly sensitive clay. Indeed, Ladd (1972) reports that the test embankment underwent eventual rupture, without any noticeable signs of failure. The pressure-deformability curve given in *Fig. 11* also is compatible with the statement made by Ladd and is only barely indicative of the degradation in stiffness before failure.

The performance of the Cubzac-les-Ponts (A) test embankment is also worth discussing. The deposit is featured by a *8* meter-thick, slightly overconsolidated, soft organic clay that has a natural water content as high as *200%* at its weakest portion (Magnan *et al.*, 1983). The pressure-deformability curve depicted in *Fig. 11*, however, suggests that the overall stiffness of the deposit is moderate. In this regard, it is important to recognize that the soft organic clay actually is covered with a *1.8* meter-thick, overconsolidated clay crust, and that the embankment was brought to failure rather rapidly in *8* days (Leroueil *et al.*, 1985). If the loading were performed more slowly, then the passage of the foundation soils from the overconsolidated to the normally consolidated state would have been more dominant, thus causing more remarkable reduction in the overall stiffness.

It may now be instructive to set a reference bearing capacity, in such a way that a soil deposit having a lower bearing capacity exhibits the highly ductile behavior, whereas a soil deposit having a larger bearing capacity undergoes the rather brittle behavior. The results summarized in *Fig. 11* suggest that such a reference bearing capacity can be taken at around *100 kPa*.

In essence, the above discussion emphasizes the importance of allowing for the deformability or the nature of the soil deposit as part of the strategy for monitoring the embankment stability.

7-4-4. Performances of Partial Drainage and Discussion

The measured relationships between the volume gained in lateral deformation and the volume lost in settlement are shown in *Fig. 13* for the peat deposit (Koda) and for the deposits of soft clays overlain by peats (Ebetsu and Atchafalaya levee). In *Fig.13(a)*, the performances during the construction stage (or the first filling stage) are depicted, whereas in *Fig. 13(b)*, the performances after the end of construction (or the end of the first filling stage) are also indicated. Symbols *E* and *S* on *Fig.13(b)* stand, respectively, for the end of the first filling phase and the start of the second filling phase. What is most notable from *Fig. 13* is that the behavior of the soft foundations is far from undrained, or isochoric in a more rigorous sense, even during the loading stages.

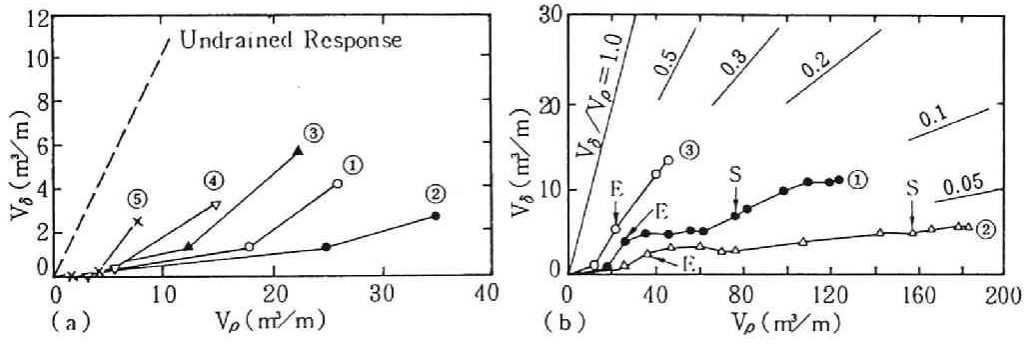

① Ebetsu (NF3)
② Ebetsu (RF), with Sand Drains
③ Atchafalaya Levee (TS2)
④ Koda (B)
⑤ Koda (A), with Sand Drains

Fig. 13 Performances of the Displacement Volumes of the Deposits Characterized by the Presence of Peats

The ratios of the volume gained in lateral deformation to the volume lost in settlement at the end of construction, or at the end of the first filling stage, are plotted in *Fig. 14* against the *B/H* ratios of the five embankments indicated. For purposes of comparison, the theoretical results discussed in *Fig. 6* are also indicated on *Fig. 14*.

Let us first discuss the performances of the Ebetsu test embankment. The selection of the thickness of soft foundations, H, for this test site deserves attention, because there exist the intercalated sands in the clay bed (see columnar section 2 in *Fig. 8*). In short, we have adopted the thickness ($H^*=11.3$ *m*) from the ground surface to the the upper sand layer at *M.S.L.-3.6* m, in view of the inclinometer readings available, instead of the total thickness of the soft foundations, $H=29.5$ *m* on average. It should also be mentioned regarding the test section (*RF*) that the sand drains were installed down to the level of the upper sand layer, and that the reinforcement of the fill itself was made using steel strips. A comparison between the field performance data plotted on *Fig. 14* clearly shows that in

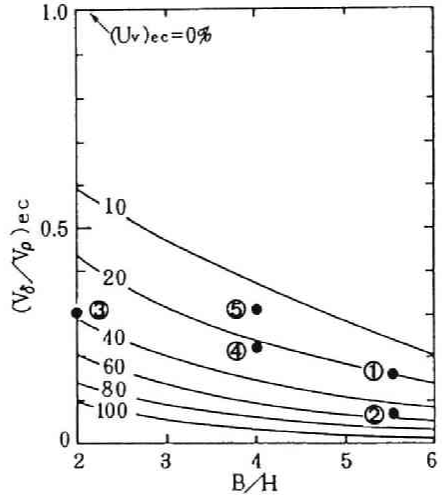

① Ebetsu (NF3)
② Ebetsu (RF), with Sand Drains
③ Atchafalaya Levee (TS2)
④ Koda (B)
⑤ Koda (A), with Sand Drains

Fig. 14 Ratio of Displacement Volumes Plotted against B/H Ratio, with the Lines of Equal Degree of Consolidation in terms of Net Volume Changes

this particular site, the sand-drain treatment of the soft foundations coupled with the fill reinforcement was highly effective in suppressing the lateral flow. In this regard, it may be appropriate to mention that in the test section marked *RF*, the fill was successfully constructed, in two stages, to the height of *8.0 m*, whereas in the untreated section (*NF3*) the fill was raised to the height of *3.5 m* with much difficulty (The Japan Highway Public Corporation, 1979).

In the case of the Koda test site, however, no beneficial effects of installing sand drains can be seen from the field performance data plotted on *Fig. 14*. This may be ascribed to the fact that the embankment width relative to the thickness of the peat layer was rather narrow at the Koda test site, as compared with the Ebetsu test site.

The field performance data of the test section 2 of the Atchafalaya levee plotted on *Fig. 14*, suggests that significant net volume-changes were accompanied by the ground deformation. This suggestion would be interesting, in view of the reported fact (Kaufman and Weaver, 1967) that the test section was designed at a factor of safety equal to 1.1 and was actually marginal in stability at the final stage of the filling work. A clue for re-examining the above suggestion in the future would be to assess the degree of saturation of the foundation soils (in particular, of the peaty soils) , and to make clear how much the porewater was really squeezed out of the foundation soils.

7-5. Conclusions

A framework for assessing the lateral soil movements has been developed, based on the coupled stress-flow analyses using the method of finite elements and based on a detailed study of the field performance data. The framework facilitates a general understanding of the problem of lateral soil movements, before conducting individual numerical analyses for specific configurations of embankments on specific kinds of soft soils, at specific sites. This perspective becomes particularly important, in view of the following main findings of the present research:

(1) Degree of partial drainage of embankment foundation is governed by the rate of filling and the rate of consolidation, and it can be estimated by using the time factor proposed here.

(2) The ratio of displacement volumes, V_δ/V_ρ is introduced. It is defined as the ratio of the volume gained in lateral deformation to the volume lost in settlement, and governed by the degree of partial drainage and B/H ratio.

(3) The nature or stratification of the soft soil deposits is well reflected in their pressure-lateral deformability performances, that is, deterioration of the foundation rigidity is remarkable for 'weak soft foundations' that mainly consist of peat or organic clay, whereas, almost no reduction in the rigidity takes place for 'stiff clay foundations' formed in the post-glacial area.

(4) In many cases, a significant drainage is accompanied by the lateral ground movement taking place even during the loading stage.

REFERENCES

(1) D'Appolonia, D. J., T.W. Lambe and H.G. Poulos (1971) : Evaluation of pore pressures beneath an embankment, J. Soil Mech. Found. Div., ASCE, Vol.97, SM6, pp. 881-897.

(2) Endo, K., K. Sekimoto, T. Takano, M. Suzuki and Y. Hirai (1983) : Alluvium of the planes of Kanto, URBAN KUBATA, Vol.21, pp. 26-43 (in Japanese).

(3) Kaufman, R. I. and F.J. Weaver (1967) : Stability of Atchafa-laya levees. J. Soil Mech. Found. Div., ASCE, Vol.93, SM4, pp. 157-176.

(4) Ladd, C. C. (1972) : Test embankment on sensitive clay. Proc. Specialty Conf. on Performance of Earth and Earth-Supported Structures, ASCE, 1, pp. 101-128.

(5) Lambe, T. W. (1973) : Predictions in soil engineering, Geotechnique, Vol.23, No.2, pp. 149-202.

(6) Leroueil, S., J.P. Magnan et F. Tavenas (1985) : Remblais sur Argiles Molles. Technique et Documentation, Lavoisier, Paris.

(7) Lumb, P. (1963) : Rate of settlement of a clay layer due to a gradually applied load. Civil Eng. Publ. Wks Rev, March, pp.315-317.

(8) Magnan, J. P., C. Mieussens and D.D. Queyroi (1983) : Etude d'un remblai sur sols compressibles-Le remblai B du site experimental de Cubzac-les-Ponts. Rapports de Recherche LPC N, 127, Laboratoire Central des Ponts et Chaussees, Paris.

(9) Marsland, A. and J.J.M. Powell (1977) : The behavior of a trial bank constructed to failure on soft alluvium of the River Thames. Proc. Int. Symp. on Soft Clay, Bangkok, 1, pp. 505-525.

(10) Muromachi, T. and S. Watanabe (1963) : Deformation of soft peat foundation under embankment. Railway Technical Research Report, 364, pp. 1-49 (in Japanese).

(11) Ramalho-Ortigao, J. A. (1983) : Werneck, M. L. G. and Lacerda, W. A., Embankment failure on clay near Rio de Janeiro. J. Geotech. Eng., ASCE, Vol.109, No.11, pp.1460-1479.

(12) Schofield, A. N. and C. P. Wroth (1968) : Critical State Soil Mechanics, McGraw-Hill, London.

(13) Sekiguchi, H., (1977) : Rheological characteristics of clays, Proc. 9th Int. Conf. Soil Mech. Found. Eng., Tokyo, Vol.1, pp. 289-292.

(14) Sekiguchi, H., Y. Nishida and F. Kanai (1981) : Analysis of partially drained triaxial testing of clay. Soils and Foundations, Vol.21, No.3, pp. 53-66.

(15) Sekiguchi, H., Y. Nishida and F. Kanai (1982) : A plane-strain viscoplastic constitutive model for clay. Proc. 37th Nat. Conf., JSCE, pp. 181-182 (in Japanese).

(16) Shibata, T. and H. Sekiguchi (1980) : A method of predicting failure of embankment foundation based on elasto-viscoplastic analyses. Proc. of JSCE, Vol.301, pp. 93-104 (in Japanese).

(17) Tavenas, F., C. Mieussens and F. Bourges (1979) : Lateral displacements in clay foundations under embankments, Canadian Geotech. Journal, Vol.16, pp.532-550.

(18) The Japan Highway Public Corporation (1979) : Report on the performances of Ebetsu Trial Embankment (in Japanese).

(19) The Japan Highway Public Corporation (1981) : Report on the performances of Kanda Trial Embankment (in Japanese).

CHAPTER 8

Deformation Analysis of a Reclaimed Marine Foundation Subjected to Land Construction

8-1. Introduction

The outstanding development of coastal areas has recently been accomplished here in Japan. As shown in *Fig. 1*, we already have huge reclaimed islands, along the Osaka Bay, such as Port Island, Rokko Island and the Osaka Nanko Islands. Furthermore, Kansai International Airport is under construction in the offing of southern Osaka. With the construction of offshore structures, the deformation and stability of the alluvial clay sedimented in close vicinity to the seabed have become an issue because of its low strength. In order to overcome these problems, the alluvial deposits just beneath the revetments are often treated with densely compacted sand (*SCP*) to control the settlement of the foundation ground. In addition, sand

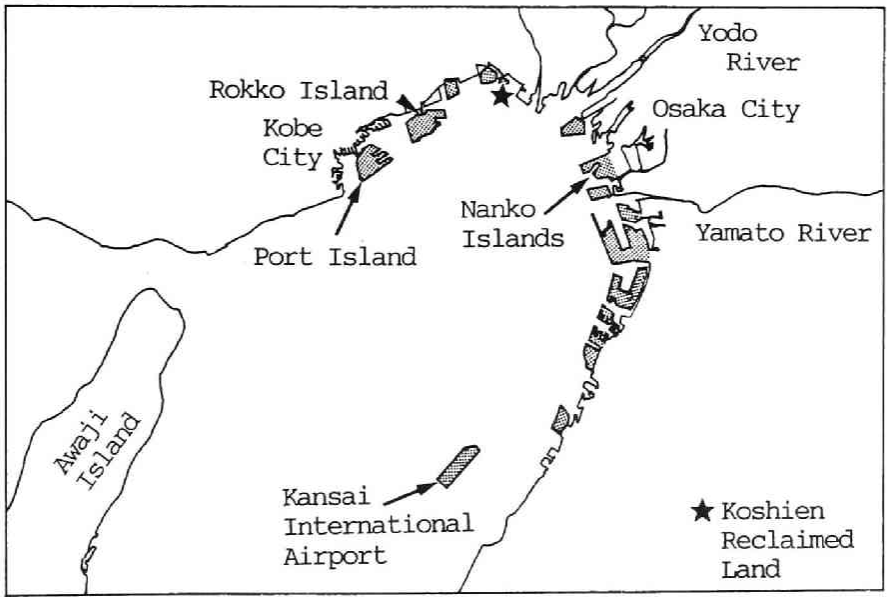

Fig. 1 Distribution of Reclamation Development in the Osaka Bay Area

drains are driven into the clay foundation to promote drainage and consolidation, especially in the reclaimed areas. In this way, good results have been obtained for deformation and stability control of alluvial deposits by soil improvement.

As offshore structures have been growing larger, however,deep and thick diluvial clay layers sedimented beneath the alluvial deposits have begun to be affected. Therefore, the plastic yielding and long-term characteristics of the diluvial clay have become a problem. Since it is almost impossible to improve diluvial clay layers, because of their stratigraphic position, consolidation takes much time and corresponding long-term deformation will continue. When the foundation is built, a sand gravel stratum situated between the alluvial and diluvial clay deposits is usually selected as a bearing stratum. Therefore, the long-term settlement of the diluvial clay layers has a negative effect on the superstructures; the differential settlement is particularly harmful to the consistent operation.

In this chapter, deformation analysis of a reclaimed marine foundation is performed in terms of the elasto-viscoplastic finite element method, in which the construction process of reclaimed ground has been modelled exactly. The Koshien reclaimed land, which is under construction is exemplified here. Firstly, the stability of the reclaimed marine foundation is investigated through an elaborate consideration of numerically derived settlement and lateral displacement profiles and the generating/dissipating process of excess pore water pressure subjected to reclamation. Special attention is then paid to the estimation of the plastic yielding phenomena of the diluvial clay layers, which has a serious effect on the long-term deformation of the reclaimed marine foundation. Secondly, the settlement of the ground surface and the diluvial clay deposits, lateral displacement profiles and excess pore water pressure with depth were observed for the reclamation performed during fiscal 1988. The calculated performance by *FEM* is compared with these *in situ* measured results. The validity of the elasto-viscoplastic algorithm used here is then discussed for deformation prediction of the reclaimed marine foundation. Finally, a numerical analysis is performed to investigate the harmful effects of the residual deformation occurring after commencement

of the operation on the Hanshin Expressway Bayroute, which will be constructed on this reclaimed land. The consistent operation of the expressway is also then discussed.

8-2. Elasto-Viscoplastic Finite Element Analysis

8-2-1. Elasto-Viscoplastic Constitutive Model

The elasto-viscoplastic constitutive model used in this paper was proposed by Sekiguchi (1977). Sekiguchi et al.(1982) modified the model to a plane-strain version. The viscoplastic flow rule for the model is generally expressed as follows:

$$\dot{\varepsilon}_{ij}^{p} = \Lambda \frac{\partial F}{\partial \sigma_{ij}'} \tag{8-1}$$

in which F is the viscoplastic potential and Λ is the proportional constant. Viscoplastic potential F is defined as follows:

$$F = \alpha \cdot \ln \left[1 + \frac{\dot{v}_0 \cdot t}{\alpha} \exp\left(\frac{f}{\alpha}\right)\right] = v^p \tag{8-2}$$

in which α is a secondary compression index, $\dot{v}_0$ is the reference volumetric strain rate, f is the function in terms of the effective stress and v^p is the viscoplastic volumetric strain. The concrete form of the model is shown in reference 4 (Mimura and Sekiguchi, 1986). The resulting constitutive relations are implemented into the finite element analysis procedure through the following incremental form:

$$\{\Delta\sigma'\} = [C^{ep}]\{\Delta\varepsilon\} - \{\Delta\sigma^R\} \tag{8-3}$$

Where $\{\Delta\sigma'\}$ and $\{\Delta\varepsilon\}$ are the associated sets of the effective stress increments and the strain increments respectively, and $[C^{ep}]$stands for the elasto-viscoplastic coefficient matrix. The term $\{\sigma^R\}$ represents a set of '*relaxation stress*' which increases with time when the strain is held

constant. The pore water flow is assumed to obey isotropic Darcy's law. In relation to this, it is further assumed that the coefficient of permeability, k, depends on the void ratio, e in the following form:

$$k = k_0 \cdot \exp\left(\frac{e - e_0}{\lambda_k}\right) \tag{8-4}$$

in which k_0 is the initial value of k at $e=e_0$ and λ_k is a material constant governing the rate of change in permeability subjected to a change in the void ratio. The drainage effect of sand drains driven into alluvial clay deposits is formulated by the macro-element method (Sekiguchi *et al.*, 1986).

8-2-2. General Condition of Koshien Reclaimed Land

The plan for the Koshien reclaimed land is shown in *Fig. 2*. The chain-dotted line will be the center of the Hanshin Expressway Bayroute. In this paper, coupled stress-flow analysis in terms of the elasto-viscoplastic

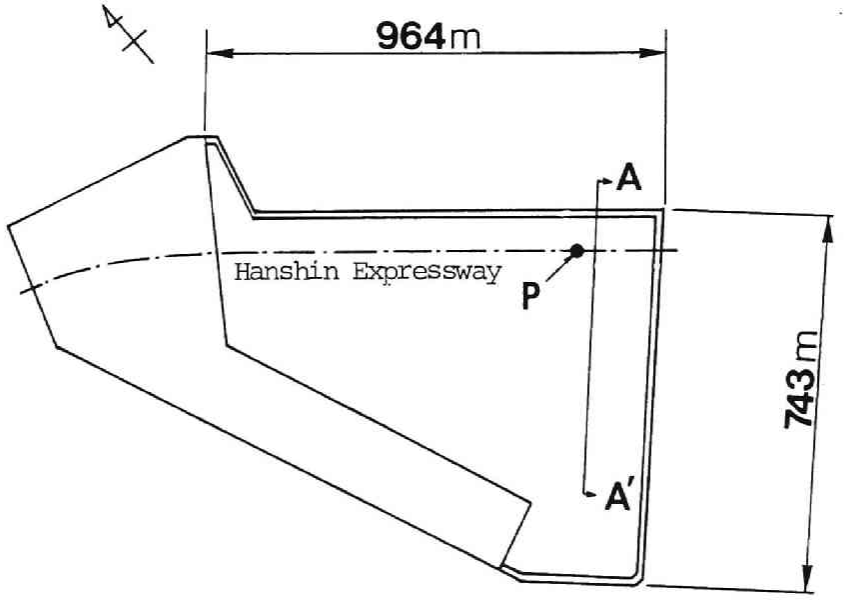

Fig. 2 Plan View of Koshien Reclaimed Land

finite element method is performed along the section shown by *A-A'*, at a right angle to the expressway.

The soil profile for the *FE* analysis is determined on the basis of the soil boring log shown in *Fig. 3*. A subsoil investigation was carried out at the point represented by *P* in *Fig. 2*. The original foundation ground is

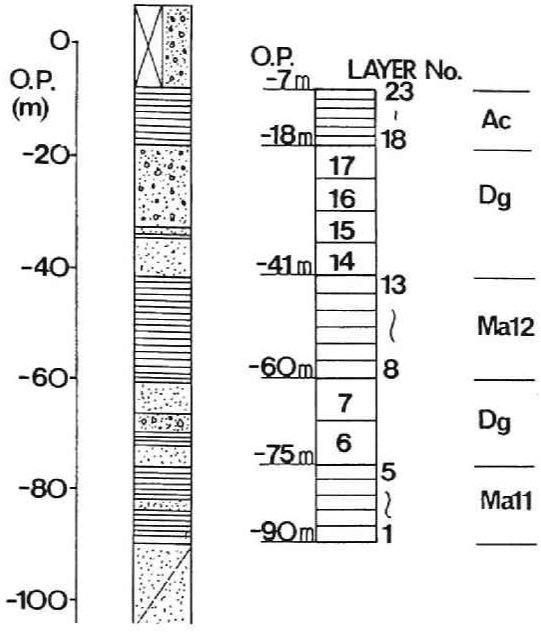

Fig. 3 Soil Boring Log Showing the Lithographic Distribution

modelled as shown in *Fig. 4*. The region selected for the *FE* analysis is 470 meters long and 83 meters deep into a diluvial sand layer. The foundation assumed here is divided into 23 layers. *Ac* represents the alluvial clay layer, and the diluvial clay deposits are divided into two layers (*Ma*12 and *Ma* 11) by a thick gravel sand layer(*Dg*). The thick gravel sand layer (*Dg*),between the alluvial and diluvial clay layers, has usually been selected as a bearing stratum for superstructures. In this paper, sand and gravel beds are assumed to be composed of perfectly drained elastic material with no excess pore water pressure generation subjected to loading. Sand drains, 50 cm in diameter and at 2 m regular intervals, are driven in a rectangular arrangement just beneath the mound revetment to promote consolidation.

In regards to reclamation, finite elements corresponding to the actual construction process are generated. As a result, we have 968 nodes and 909 finite elements for the completed cross-section of the Koshien reclaimed land.

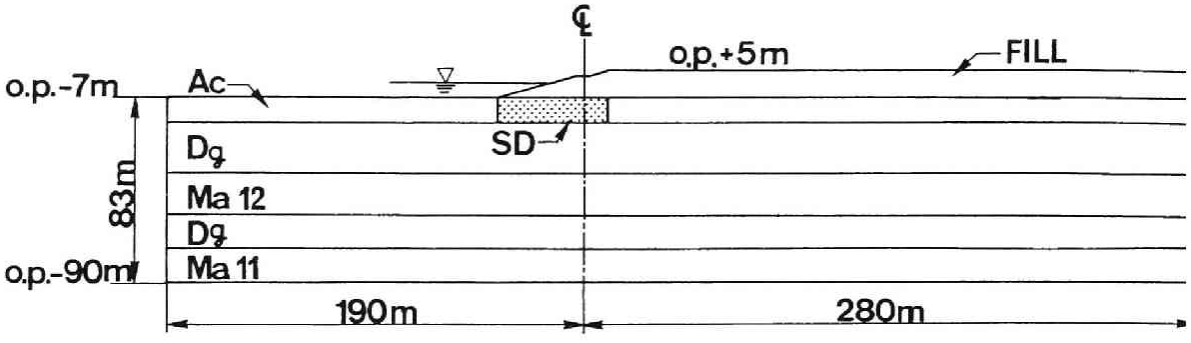

A-A' section

Fig. 4 Finite Element Model of the Foundation

8-2-3. Determination of Soil Parameters

The physical properties of the foundation clay and sand are determined and explained as follows:

(a) Compression Index λ

The definition of compression index λ is

$$\lambda = -de/d\ln(\sigma_v') = 0.434\ Cc \qquad (8\text{-}5)$$

Here, C_C is a compression index in terms of the common logarithms of overburden σ_v', the value of which can be derived by conventional oedometer tests.

(b) Swelling Index κ

The definition of swelling index κ is

$$\kappa = -de/d\ln(\sigma_v') = 0.434\ Cs \tag{8-6}$$

Here, Cs is also a swelling index in terms of the common logarithms of overburden σ_v', the value of which can be derived by oedometer tests.

(c) Critical Stress Ratio M

Concerning the critical effective stress ratio, M, we cannot directly determine the value of M, since no triaxial compression tests were conducted. A value of M equal to 1.4 is adopted as a typical value for Osaka clay after the findings by Tsuchida *et al.*, (1984) and Adachi *et al.*, (1985). The critical stress ratio, $\sin \phi'$, required for the plane-strain version model used here, can be calculated by the following relation:

$$\sin \phi' = \frac{3M}{6 + M} \tag{8-7}$$

(d) Secondary Compression Index α

Secondary compression index, α should be determined by long-term consolidation tests. However, since no long-term consolidation tests were carried out, we assume the unique relationship between $C_{\alpha e}$ and Cc here on the basis of the experimental findings (Ishii *et al.*, 1984), that is,

$$C_{\alpha e} = 0.05\ Cc \tag{8-8}$$

in which $C_{\alpha e}$ denotes the secondary compression index in terms of void ratio e. We then determine the value of α by the following definition:

$$\alpha = \frac{dv}{d \cdot \ln t} = 0.434 \left(\frac{C_{\alpha e}}{1 + e_0} \right) \tag{8-9}$$

(e) Reference Volumetric Strain Rate $\dot{v}_0$

The ratio of secondary compression index α to the reference volumetric strain rate $\dot{v}_0$, $(\alpha/\dot{v}_0)$ means characteristic time related to the completion of the primary consolidation. We adopt 10^3 days for the alluvial clay layer and 10^4 days for the diluvial clay layers (Sekiguchi *et al*, 1988).

(f) Coefficients of Earth Pressure at Rest $K_0^{(NC)}$ and $K_0^{(OC)}$

The coefficient of earth pressure at rest, $K_0^{(NC)}$, under a normally consolidated condition, can be introduced from the plane-strain elasto-viscoplastic constitutive model (Sekiguchi, 1983) used here. It is expressed as follows:

$$K_0^{(NC)} = \frac{2 - \kappa/\lambda - \sin\phi'}{2 - \kappa/\lambda + \sin\phi'} \tag{8-10}$$

Ladd *et al.* (1977) summarized the relation between the coefficient of earth pressure at rest and the overconsolidation ratio (OCR) for various clays, in terms of the plasticity index of clay. The coefficient of earth pressure at rest for overconsolidated clay $K_0^{(OC)}$ can be determined from the following relation:

$$K_0^{(OC)} = K_0^{(NC)} (OCR)^m \tag{8-11}$$

The superscript, m, can be derived in terms of the plasticity index of clay. And for ordinary natural clay whose plasticity index is around *40* to *80* %, the value of m is experimentally determined as *0.3*. In this study, therefore, the coefficient of earth pressure at rest in the overconsolidated range, $K_0^{(OC)}$, is determined as follows:

$$K_0^{(OC)} = K_0^{(NC)} (OCR)^{0.3} \tag{8-12}$$

(g) Poisson's Ratio in Terms of Effective Stress ν'

Poisson's ratio in terms of effective stress ν' can be expressed as:

$$\nu' = \frac{K_0^{(NC)}}{1 + K_0^{(NC)}} \tag{8-13}$$

(h) Elastic Rigidity G_0

Elastic shear modulus G_0 for overconsolidated clay is calculated by the following equation:

$$G_0 = \frac{1 - 2\nu'}{2(1 - \nu')} \cdot \frac{1 + e_0}{\kappa} \cdot \sigma'_{VC} \tag{8-14}$$

in which σ_{VC}' is the vertical pre-consolidation stress. According to the data, the alluvial clay deposit is normally consolidated, while on the contrary, the diluvial clay layers remain overconsolidated. The overconsolidation ratio, *OCR* for *Ma* 11 and *Ma* 12 adopted here are *1.44* and *1.5*, respectively. Pre-consolidation stress can be derived from initial overburden pressure σ_{V0}' and the *OCR* as follows:

$$\sigma_{VC}' = (OCR)\ \sigma_{V0}' \tag{8-15}$$

On the other hand, the elastic shear modulus for sand deposits is determined by the following empirical relationship in terms of the *SPT*-N value (Yosinaka, 1967)

$$G_0 = \frac{70 \cdot N}{2(1 + \nu')} \tag{8-16}$$

Values of the principal soil parameters are summarized in *Table-1*.

Table-1 Principal Soil Parameters Adopted for the Ground under the Original Seabed

MTYP	λ	κ	M	α	$\dot{v}_0$ (day^{-1})	ν'	G_0 (tf/m^2)	σ_{v0}' (tf/m^2)	σ_{vc}' (tf/m^2)	K_0	$K_{0(NC)}$	e_0	k_0 (m/day)	λ_k	
23	0.37	0.05	1.4	5.7×10^{-3}	5.7×10^{-6}	0.348	7.4	0.45	0.45	0.533	0.533	2.50	1.64×10^{-3}	0.45	Ac
22	0.37	0.05	1.4	5.7×10^{-3}	5.7×10^{-6}	0.348	21.5	1.35	1.35	0.533	0.533	2.42	1.04×10^{-3}	0.45	Ac
21	0.37	0.05	1.4	5.7×10^{-3}	5.7×10^{-6}	0.348	35.0	2.25	2.25	0.533	0.533	2.34	6.9×10^{-4}	0.45	Ac
20	0.37	0.05	1.4	5.7×10^{-3}	5.7×10^{-6}	0.348	47.9	3.15	3.15	0.533	0.533	2.26	4.7×10^{-4}	0.45	Ac
19	0.37	0.05	1.4	5.7×10^{-3}	5.7×10^{-6}	0.348	62.0	4.05	4.05	0.533	0.533	2.18	3.1×10^{-4}	0.45	Ac
18	0.37	0.05	1.4	5.7×10^{-3}	5.7×10^{-6}	0.348	72.3	5.00	5.00	0.533	0.533	2.10	2.1×10^{-4}	0.45	Ac
17	—	—	—	—	—	0.33	1222	8.00	15.44	0.5	0.5	0.93	—	—	Sand
16	—	—	—	—	—	0.33	1222	13.50	26.06	0.5	0.5	0.93	—	—	Sand
15	—	—	—	—	—	0.33	1222	19.50	37.64	0.5	0.5	0.93	—	—	Sand
14	—	—	—	—	—	0.33	1222	25.50	49.22	0.5	0.5	0.93	—	—	Sand
13	0.64	0.07	1.4	1.05×10^{-2}	1.05×10^{-6}	0.35	463.6	29.30	43.95	0.607	0.538	2.20	7.6×10^{-5}	0.71	Ma12
12	0.64	0.07	1.4	1.05×10^{-2}	1.05×10^{-6}	0.35	476.5	30.89	46.34	0.607	0.538	2.12	6.0×10^{-5}	0.71	Ma12
11	0.64	0.07	1.4	1.05×10^{-2}	1.05×10^{-6}	0.35	488.2	32.48	48.72	0.607	0.538	2.04	4.3×10^{-5}	0.71	Ma12
10	0.64	0.07	1.4	1.05×10^{-2}	1.05×10^{-6}	0.35	498.7	34.07	51.11	0.607	0.538	1.96	3.6×10^{-5}	0.71	Ma12
9	0.64	0.07	1.4	1.05×10^{-2}	1.05×10^{-6}	0.35	507.8	35.66	53.49	0.607	0.538	1.88	2.6×10^{-5}	0.71	Ma12
8	0.64	0.07	1.4	1.05×10^{-2}	1.05×10^{-6}	0.35	519.3	37.51	56.27	0.607	0.538	1.80	2.2×10^{-5}	0.71	Ma12
7	—	—	—	—	—	0.33	1300	42.32	60.94	0.5	0.5	0.93	—	—	Sand
6	—	—	—	—	—	0.33	1300	49.82	71.74	0.5	0.5	0.93	—	—	Sand
5	0.41	0.05	1.4	8.7×10^{-3}	8.7×10^{-7}	0.349	864.1	54.58	78.59	0.597	0.535	1.37	2.3×10^{-5}	0.47	Ma11
4	0.41	0.05	1.4	8.7×10^{-3}	8.7×10^{-7}	0.349	895.8	56.59	81.48	0.597	0.535	1.37	2.3×10^{-5}	0.47	Ma11
3	0.41	0.05	1.4	8.7×10^{-3}	8.7×10^{-7}	0.349	927.7	58.60	84.38	0.597	0.535	1.37	2.3×10^{-5}	0.47	Ma11
2	0.41	0.05	1.4	8.7×10^{-3}	8.7×10^{-7}	0.349	959.5	60.61	82.27	0.597	0.535	1.37	2.3×10^{-5}	0.47	Ma11
1	0.41	0.05	1.4	8.7×10^{-3}	8.7×10^{-7}	0.349	991.4	62.62	90.17	0.597	0.535	1.37	2.3×10^{-5}	0.47	Ma11

8-2-4. Process of Revetment Construction and Reclamation

The construction sequence is shown in *Fig. 5* and the completed cross-section of the reclaimed land is shown in *Fig. 6* with the process of the revetment construction and reclamation. First of all, sand drains (*SD*) were driven into the alluvial deposit just beneath the mound revetment to promote consolidation, subsequently, a rubble mound has been formed in 1985. The mound revetment was constructed in 1986. Reclamation was

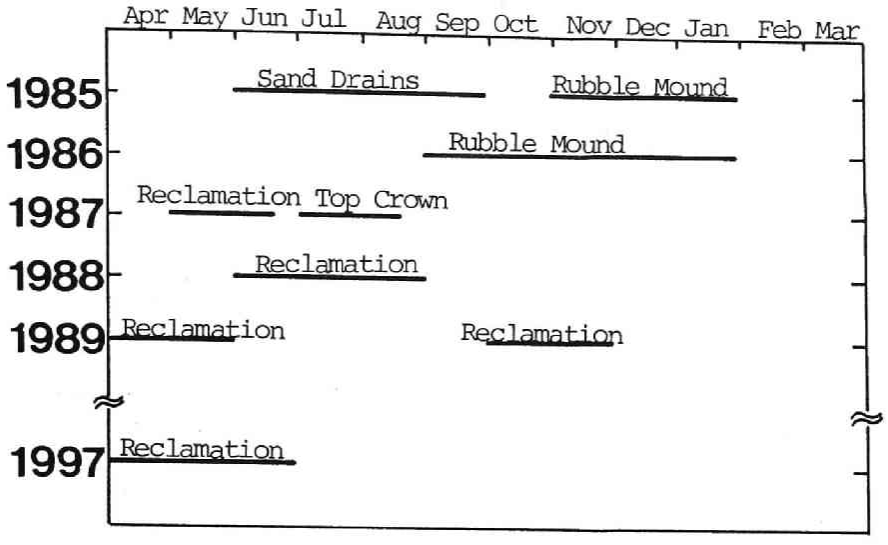

Fig. 5 Construction Sequence

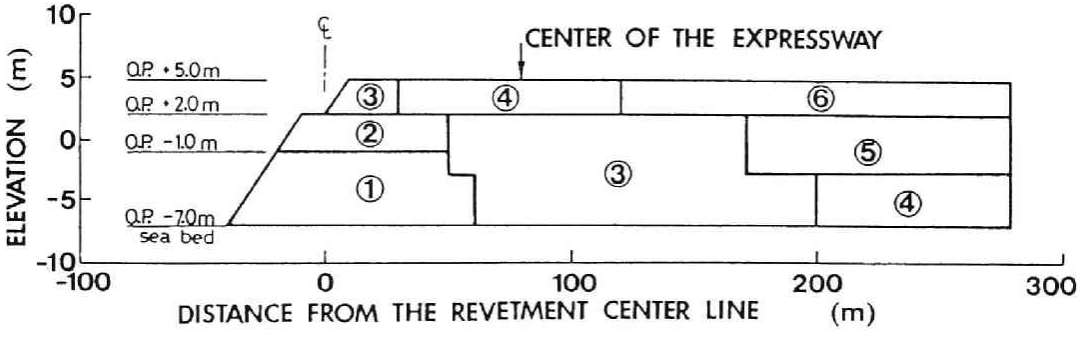

① 1985 : Rubble mound formation
② 1986 : Raising of the revetment mound
③ 1987 : Reclamation and construction of top crown of the revetment
④ 1988 : Reclamation
⑤ 1989 : Reclamation
⑥ 1997 : Reclamation

Fig. 6 Cross-section of the Reclaimed Land with the Process of Construction

initiated in 1987, and the area where the Hanshin Expressway will be built was completed in 1988 with an *O.P.* 5.0 meters high. Reclamation of the island will be completed by 1993 when operation of the expressway will commence, except the final raising up to the height of an *O.P.* 5.0 meters planned to be performed inside of the reclaimed land in 1997.

Instruments have been set up to observe ground movement and the generation/dissipation of excess pore water pressure subjected to reclamation since the beginning of 1988. Settlement plates have been set on the surface of the reclaimed ground along the cross-section *A-A'*, and differential settlement gauges have been installed in the foundation ground together with pore water pressure cells to check the generation/dissipation process of the excess pore water pressure. In addition, inclinometers have been installed at the center line of the expressway to measure the lateral displacement profiles of the reclaimed marine foundation.

8-3. Calculated Performance of the Reclaimed Marine Foundation

8-3-1. Settlement Profiles

The settlement profile of the seabed along cross section *A-A'* subjected to revetment construction and reclamation is shown in *Fig. 7*. A

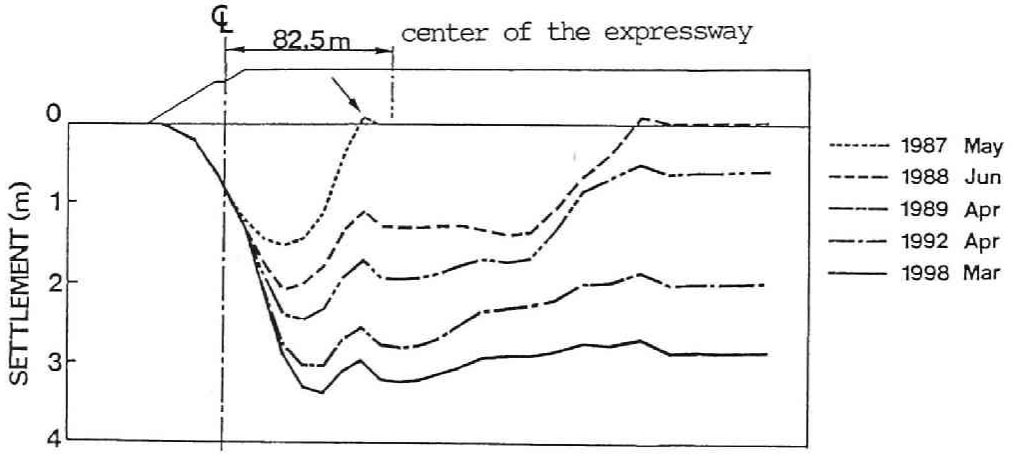

Fig. 7 Settlement Profiles of the Seabed

large settlement occurred beneath the revetment because water dissipation and consolidation were promoted in this *SD* treated area and considerably heavy localized loading was applied at the revetment construction. The seabed heaved due to rapid construction of the revetment at the edge of this localized loading area, as indicated by the arrows in *Fig. 7*. Subsequent extensive reclamation initiated in 1987 has been performed uniformly, such that the corresponding settlement of the seabed advanced equally. As a result, an uneven shape of the seabed has remained. The calculated maximum settlement of *3.3* meters will take place 45 meters inside the reclaimed ground from the revetment centerline by the end of fiscal 1998.

The settlement profile at the crest of the diluvial clay deposits is shown in *Fig. 8*. Both the shape of the profile and the location of the maximum settlement which occurred are different from those of the seabed. This is because stress deep in the foundation ground (diluvial layers) must be what reflects the loading magnitude on the seabed, due to stress dispersion and redistribution. Let us take a look at the profiles of the total vertical stress increment, ($\Delta\sigma_V$), subjected to reclamation at the start of operation of the Hanshin Expressway represented by the solid lines *(A)* in *Figs. 9(a)* and *(b)*. The effects of the construction process is outstanding for the alluvial clay deposits situated at a shallow depth in the foundation ground. In other words, the vertical stress increment becomes largest beneath the rubble mound of the revetment, *45* meters from the centerline of the revetment. On the other hand, the stress state for the diluvial layer

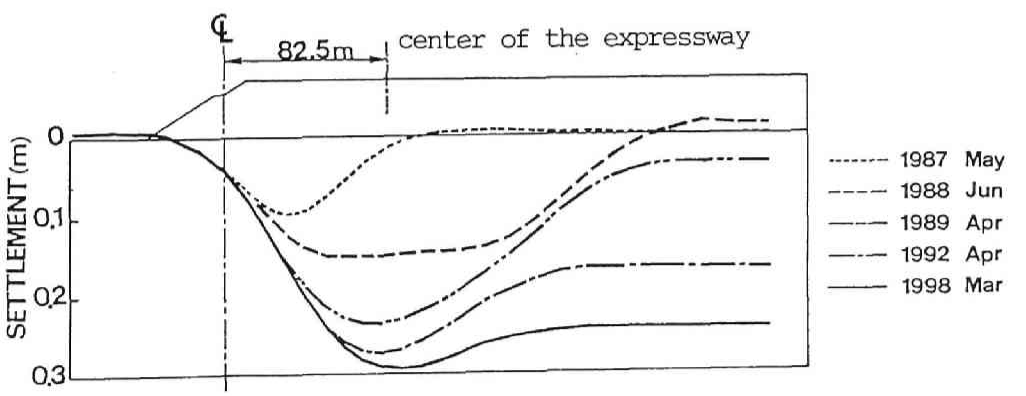

Fig. 8 Settlement Profiles of the Diluvial Layers

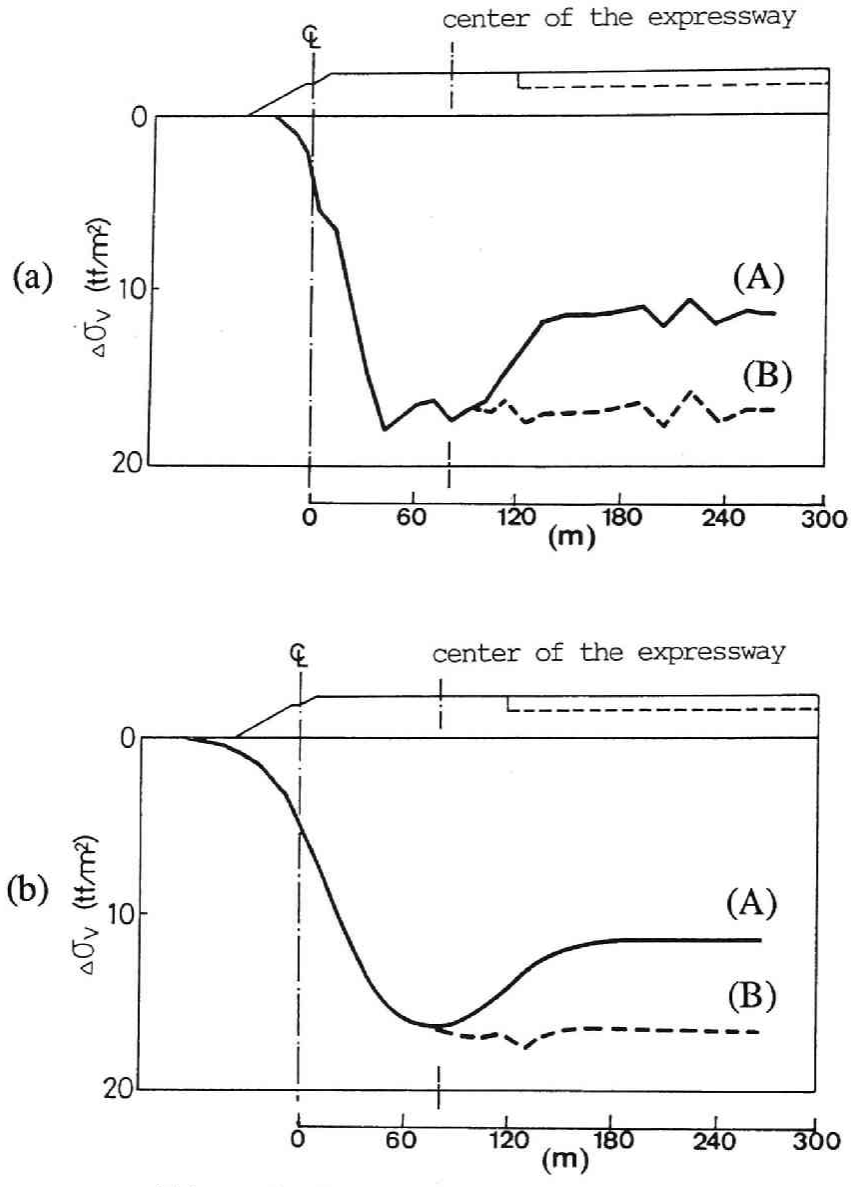

(A) : at the Start of Operation (1993)
(B) : at the Completion of Reclamation (1998)

Fig. 9 (a) Stress Increment Profile at the Seabed
(b) Stress Increment Profile at the Crest of the Diluvial Layers

(*Ma* 12) is influenced more by the magnitude of the filling. Reclamation will be performed at the back of the expressway after operation has begun. The height reaches *O.P.* 5.0 meters, which is equivalent to that of the existing completed area. Stress increment profiles shown by the hatched lines *(B)* in those two figures reflect these phenomena well. Uniform stress profiles are derived inside the reclaimed land for both alluvial and diluvial clay deposits. As mentioned above, however, the uneven shape of the settlement profiles remains. This is mainly due to the occurrence of plastic deformation at the early stage of construction. Again in *Fig. 8* , the calculated maximum settlement of the diluvial clay deposits will be *30* cm at most by the end of fiscal 1998, although we have potential plastic yielding in the upper *Ma* 12 layer. Since the residual settlement from the first *5* years from the start of operation of the Hanshin Expressway (1993 to 1998) is limited to a few centi meters, harmful effects to superstructures may be ruled out.

Stress distribution with depth at the centerline of the expressway, *80* meters from the revetment centerline, is shown in *Figs. 10(a), (b)* and *(c)*, at the completion of the reclamation, at the start of operation (1993), and *5* years after the start of operation (1998), respectively. The total stress due to reclamation is expressed by the solid lines. The pre-consolidation pressure, σ_{VC}', and the initial effective overburden are expressed by the hatched and chain-dotted lines. In the normally consolidated clay layer, large amounts of excess pore water pressure with a maximum value of *15* tonf/m^2 (*147*kN/m^2) are generated. As the drainage advances, this excess pore water pressure gradually dissipates. It remains at about *7.0* tonf/m^2 (69kN/m^2) at the start of the expressway operation and becomes only 1.0 tonf/m^2 (*9.8*kN/m^2) by the end of 1998, *5* years after the start of operation. After dissipating the excess pore water pressure, we must pay attention to the long-term settlement due to secondary consolidation for the alluvial clay layer. On the other hand, since plastic yielding occurs only in the upper part of the diluvial clay layer (*Ma* 12), no serious long-term settlement will take place for the diluvial layers.

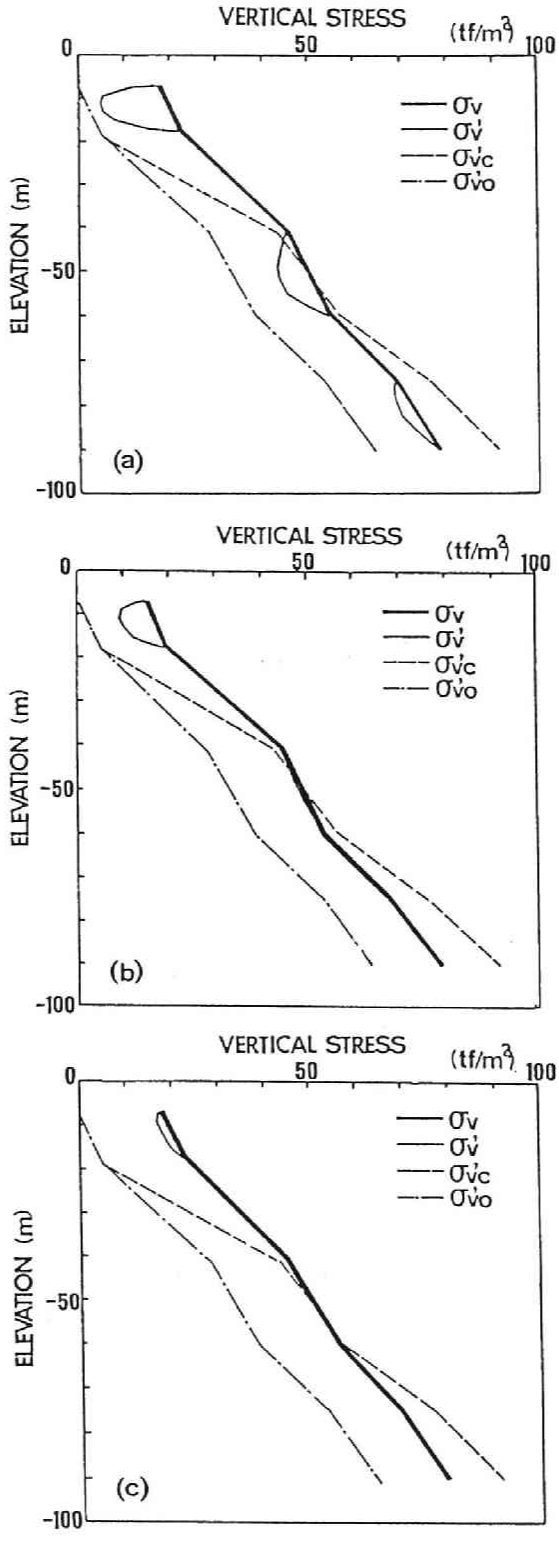

Fig. 10 Stress Distribution with Depth at the Center of the Expressway
(a) : at the Completion of Reclamation (1988),
(b) : at the Start of Operation of the Expressway (1993),
(c) : 5 Years after the Operation of the Expressway (1998)

8-3-2. Time-Settlement Relations

Time-settlement performance clearly reflects the process of excess pore water dissipation. The calculated time-settlement relation of the seabed and the crest of the diluvial layers at the centerline of the expressway are shown in *Figs. 11* and *12*, respectively. In both figures,

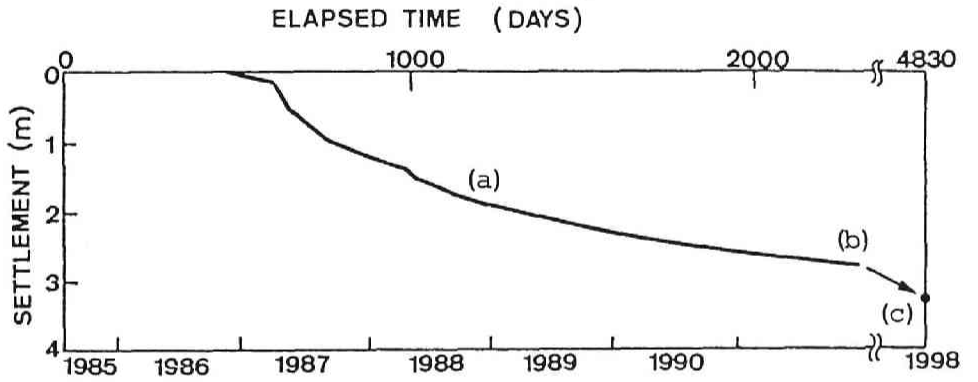

Fig. 11 Time Settlement Curve of the seabed at the Center of the Expressway ;
(a) : at the Completion of Reclamation (1988)
(b) : at the Start of Operation of the Expressway (1993),
(c) : 5 Years after Operation of the Expressway (1998)

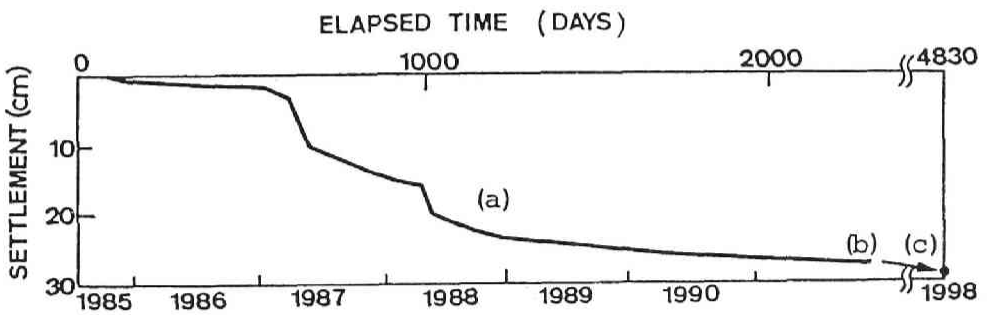

Fig. 12 Time Settlement Curve of the Diluvial Layers at the Center of the Expressway;
(a) : at the Completion of Reclamation (1988)
(b) : at the Start of Operation of the Expressway (1993),
(c) : 5 Years after Operation of the Expressway (1998)

symbols *(a)*, *(b)* and *(c)* correspond to those in *Fig. 10*, that is to say, *(a)* at the completion of reclamation, *(b)* at the start of operation of the expressway and *(c)* 5 years after the start of operation of the expressway. As indicated by *(c)*, the total settlement of the seabed and the diluvial clay layer shall reach *3.3* m and *0.3* m, respectively, by 1998, *5* years after commencement of the expressway operation. Because the major part of the diluvial clay deposits remains in a non-yielding state, even after completion of the reclamation, *90 %* of the total settlement is governed by the settlement that occurred in the alluvial clay layer in this particular case.

8-3-3. Lateral Displacement Profiles

The lateral displacement profile with depth at the centerline of the mound revetment is shown in *Fig. 13*. Remarkable lateral ground

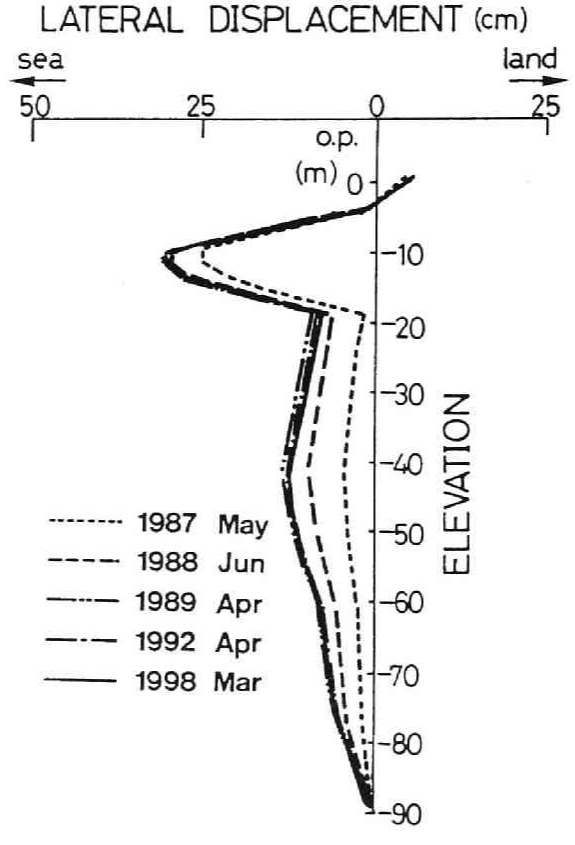

Fig. 13 Lateral Displacement Profiles with Depth beneath the Revetment

movement takes place upon construction of the mound revetment from 1985 to 1987, with a maximum seaward displacement of *0.25* m in the alluvial clay layer. This large amount of displacement is mainly due to a rapid localized gravel mound formation on the very soft seabed. At the same time, the crest of the mound revetment moved towards the reclaimed land because of the predominant settlement of the reclaimed area during construction. The lateral displacement of the alluvial clay layer caused by subsequent reclamation was not as large, although that of the diluvial layers still continued. As a whole, however, the large lateral displacement mainly occupied the alluvial clay layer, and movement of the diluvial layers was restrained by the thick sand gravel stratum beneath the alluvial clay deposit.

The lateral displacement profile at *80* meters from the revetment centerline (centerline of the expressway) is shown in *Fig. 14*. Lateral

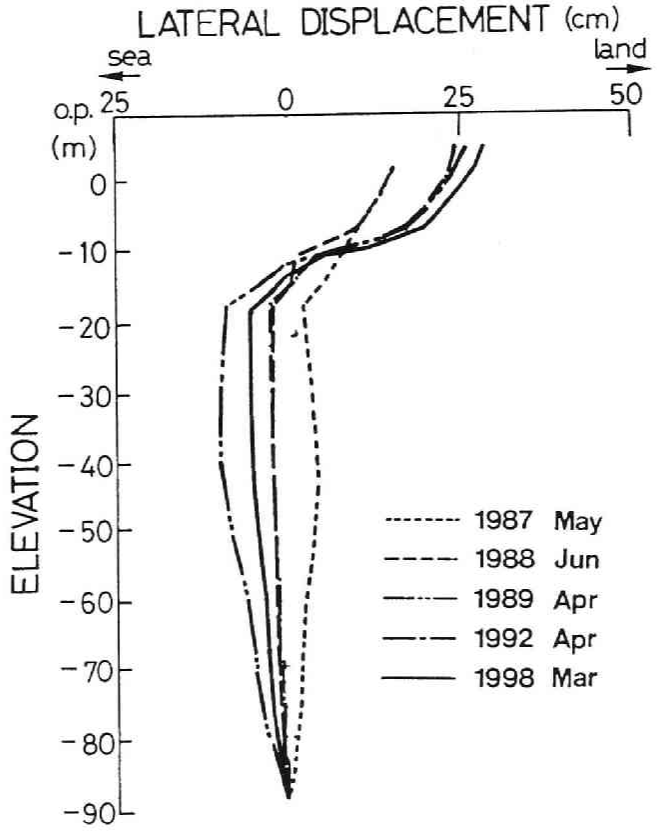

Fig. 14 Lateral Displacement Profiles with Depth at the Center of the Expressway

displacement first occurred towards the reclaimed land due to mound revetment construction. With advanced reclamation, however, the lateral displacement predominantly occurred seawards. Compared with the performance at the centerline of the revetment, the marine foundation deformed uniformly without a remarkable peak lateral displacement. This is because the area was reclaimed uniformly and remained unaffected by the rapid construction of the mound revetment. For these reasons, we observe a stable lateral displacement profile at the centerline of the expressway.

8-3-4. Effective Stress Path

Effective stress paths of the alluvial clay layer subjected to reclamation are shown in *Fig. 15*. The selected points are : *(a)* beneath the mound revetment, *(b) 40* meters from the revetment centerline in the reclaimed land and *(c) 80* meters from the revetment centerline in the reclaimed land. All selected elements are located at a depth of *O.P. -10.6* to *-12.4* meters, which is in the middle of the alluvial clay layer. Here, r denotes the mean effective stress in terms of $(\sigma_1' + \sigma_3')/2$ and s denotes the deviatoric stress in terms of $(\sigma_1' - \sigma_3')/2$. In *Fig. 15 (a)*, only a small change in stress can be seen for the element beneath the mound revetment due to a reduction in stress transmitted to the marine foundation subjected to an inclination of the slope and buoyancy. In regards to the element *40* meters from the revetment centerline (*Fig. 15 (b)*), the stress path once approaches the failure line by the rapid revetment construction in 1986. We must pay attention to the undrained response of the foundation ground, especially under the low stress level, because it directly leads to failure. In this particular case, however, the state of the foundation ground has been restored by subsequent consolidation, and the stress path moves along the K_0 line. Thus, the marine foundation is thought to remain steady. A steady stress state has also been confirmed for the element just beneath the centerline of the expressway (*Fig. 15 (c)*). Through the construction process, the stress path moves along the K_0 line. According to these findings, the alluvial clay deposits are far from failure during the process of revetment construction and reclamation.

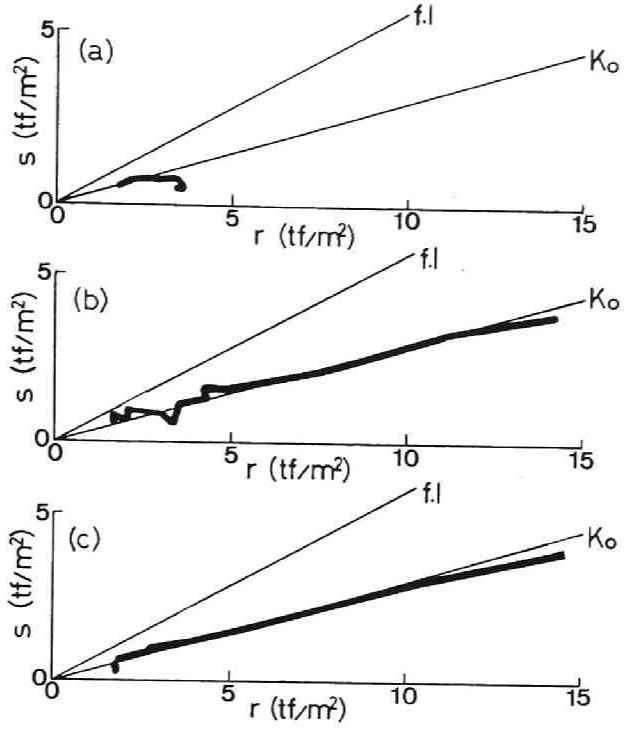

Fig. 15 Effective Stress Paths of the Alluvial Clay Elements;
(a) : beneath the Revetment,
(b) : 45 meters from the Center of the Revetment,
(c) : at the Center of the Expressway

The effective stress paths of the diluvial clay layers are shown in *Fig. 16*. The location of the selected elements is the same as that of the alluvial clay layer shown in *Fig. 15*. All elements are chosen from the *Ma* 12 layer at a depth of *O.P.* -44 to -47 meters, which is in the middle of this layer. As mentioned above, the *OCR* of the *Ma* 12 layer is assumed to be *1.5* from the oedometer test results in this study. The change in stress is rather small for the element beneath the revetment, *(a)*, in the same way as that for the alluvial clay layer. In contrast, for the elements beneath the reclaimed land, *(b)* and *(c)*, deviatoric stresses increase during the primary stage and the stress paths move along the normally consolidated K_0 line because plastic yielding partially occurs due to reclamation. As a whole, however, the diluvial clay layers also keep a very steady stress state during the process of revetment construction and reclamation.

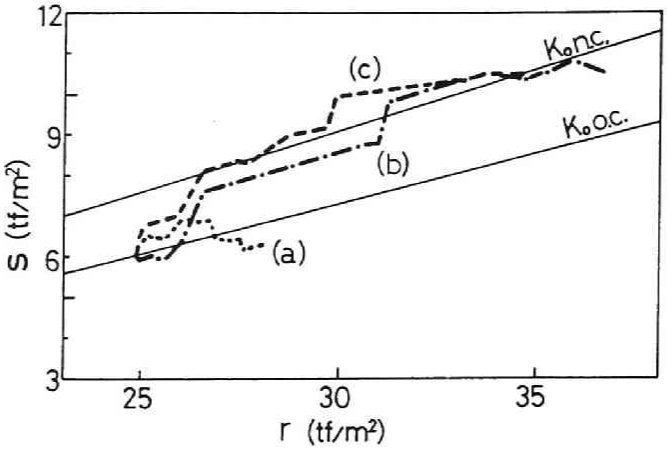

Fig. 16 Effective Stress Paths of the Diluvial Clay Elements (Ma 12);
(a) : beneath the Revetment,
(b) : 45 meters from the Center of the Revetment,
(c) : at the Center of the Expressway

8-4. Comparison of measured Results and Calculated Performance

Settlement plates, differential settlement gauges, inclinometers and pore water pressure cells have been equipped in the reclaimed land since 1988 to monitor the ground movement and water pressure generation/dissipation subjected to reclamation. In this section, we shall compare the calculated performance with the measured results along cross-section *A-A'*.

After setting up these devices for observation, reclamation to a height of *O.P. +5.0* meters was initiated. And, the elevation of the reclaimed land has been increased to *O.P. +5.0* meters at the centerline of the expressway. The observation period was from either April or June of 1988 to the end of 1988, depending on the observation. Settlement, lateral displacement and excess pore water pressure were measured for about eight months. *Fig. 17* shows a comparison of the calculated performance and measured results for the settlement profile of the reclaimed ground surface. The calculated performance accurately predicts the *in situ* measured settlement profile.

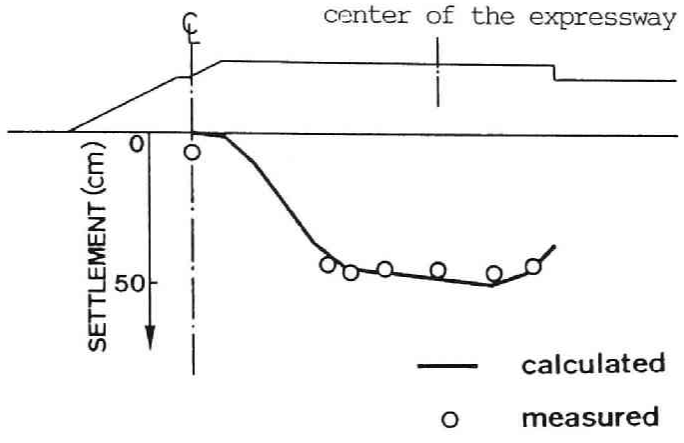

Fig. 17 Comparison of the Calculated Performance and Measured Results for the Settlement of the Seabed

A comparison of the calculated performance and measured results for the settlement profile of the crest of the diluvial layers is shown in *Fig. 18*. Underground settlements were measured by the differential settlement gauges installed in the ground. Although we have only two items of data measured for the settlement of the diluvial layers, calculated performance can predict the measured results exactly. As for the settlement which took place during the reclamation in 1988, the deformation of the alluvial clay deposit is much more predominant than that of the diluvial layers.

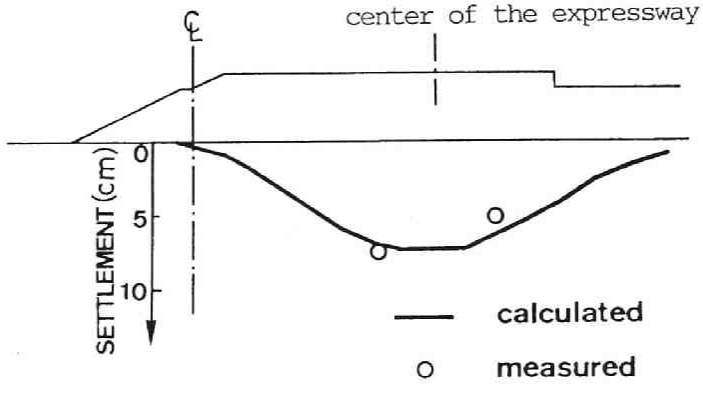

Fig. 18 Comparison of the Calculated Performance and Measured Results for the Settlement of the Diluvial Layers

A comparison of the calculated performance and measured results for the lateral displacement profile with depth at the centerline of the expressway is shown in *Fig. 19*. We can see a little discrepancy for the lateral displacement profile in the fill, that is, the calculated performance shows a typical profile toward the side of the reclaimed land, whereas the measured lateral displacements are restrained to some extent. As a whole, the calculated performance qualitatively predicts the measured lateral displacement profile during the reclamation in 1988.

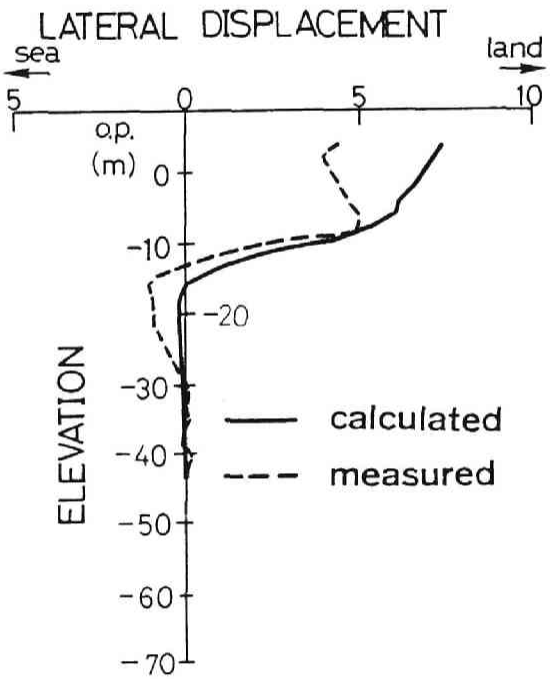

Fig. 19 Comparison of the Calculated Performance and Measured Results for the Lateral Displacement Profiles with Depth at the Center of the Expressway

Fig. 20 shows a comparison of the calculated performance and measured results for the excess pore water pressure generation/dissipation profiles with depth due to the reclamation in 1988. The water pressure cells have been embedded in both the alluvial and the diluvial clay layers, *45* meters from the revetment centerline. For the alluvial clay layer, the calculated performance can accurately predict the excess pore water

pressure generation/dissipation process. For the upper diluvial clay layer (Ma 12), on the other hand, the calculated performance slightly underestimates the measured results. The problems with an exact evaluation of the permeability of overconsolidated clay and the permeability transition subjected to plastic yielding still remain. Here, the coefficient of permeability for clay is assumed to be constant throughout the overconsolidated region and the sharp transition of permeability is also assumed at pre-consolidation pressure σ_{VC}'. Considering these unsolved problems, the calculated and measured excess pore water pressure profiles

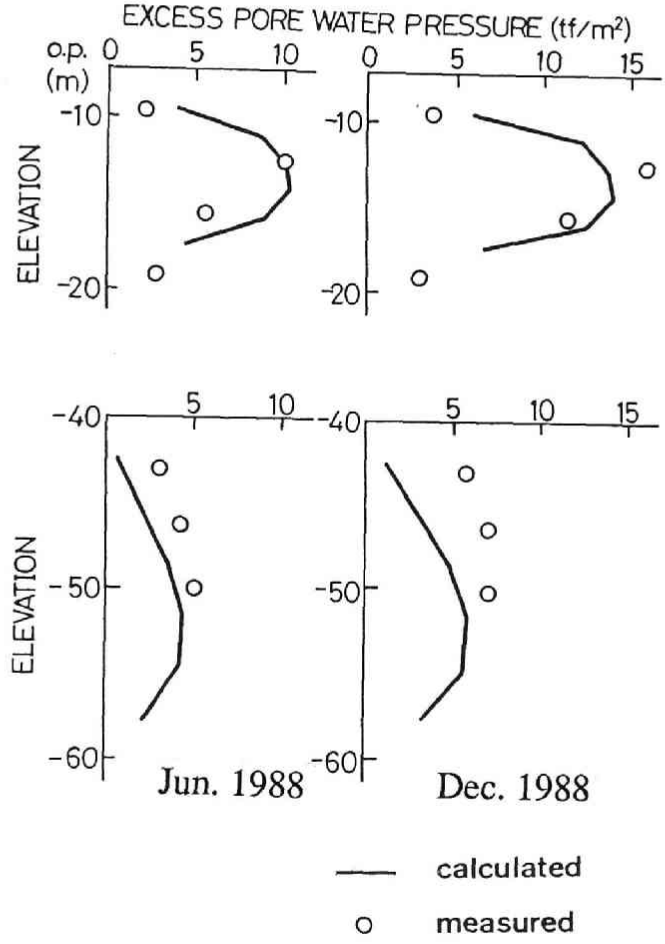

Fig. 20 Comparison of the Calculated Performance and Measured Results for Excess Pore Water Pressure Generation due to Reclamation in 1988

in the diluvial clay layer agree well. In addition, the major part of the deformation of the reclaimed marine foundation ground due to the reclamation in 1988 took place in the alluvial clay layer, and the plastic yielding of the diluvial clay is almost negligible. Therefore, the slight difference between the calculated and measured excess pore water pressures will not pose any problems.

The foundation ground shall keep deforming even after operation of the expressway subjected to delayed consolidation, delayed lateral deformation or secondary consolidation. Therefore, we must investigate the harmful effects of the delayed deformation of the ground on the existing superstructures and their foundations. A calculated lateral displacement profile at the centerline of the expressway is shown in *Fig. 21*. The lateral displacements expressed in this figure occur during the 5-year period from the start of the expressway operation from 1993 to 1998. Because the maximum lateral displacement is at most 5 cm and the

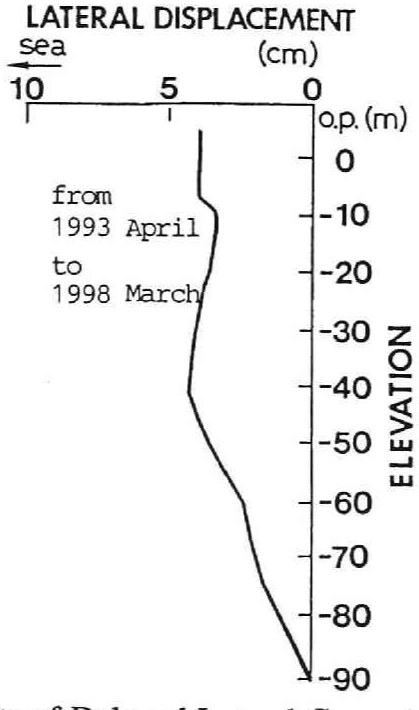

Fig. 21 Effects of Delayed Lateral Ground Movement on the Expressway Foundation

foundation ground deforms almost uniformly in the alluvial clay and gravel layers, the effects of the delayed lateral ground movement taking place after operation of the expressway has begun on the superstructures and their foundations do not become a serious issue.

8-5. Conclusions

Coupled stress-flow analysis of a reclaimed marine foundation subjected to the construction of Koshien reclaimed land is conducted using the method of finite elements based on the theory of viscoplasticity. The following conclusions are drawn:

(1) Upon revetment construction, the alluvial clay layer once approached failure due to its subjection to rapid localized loading on the very soft seabed. Because of subsequent consolidation, however, the Koshien reclaimed marine foundation ground is considered to deform stably.

(2) Compression of the alluvial clay layer contributes to the major part of the settlement subjected to reclamation. The calculated maximum settlement amounts to *3.3* meters, *3.0* meters of which is occupied by the settlement of the alluvial clay layer.

(3) Long-term settlement of the diluvial clay layers is an issue. Although the upper part of the diluvial clay deposits yields partially, the calculated settlement of the diluvial layers is limited to *0.3* m.

(4) Lateral displacements take place mainly in the alluvial clay layer with a maximum value of *0.3* m seawards at the revetment centerline, a major part of which occurs during the revetment construction. Lateral displacements of the diluvial layers are not so serious, and therefore, long-term lateral ground movement does not have any harmful effects on the superstructures and their foundations.

(5) Instruments have been installed to monitor ground movement and the generation/dissipation of excess pore water pressure. The measured

results are compared with the calculated performance. The calculated performance can accurately predict the settlement profiles, lateral displacement profile with depth and the generation/dissipation process of excess pore water pressure subjected to reclamation.

REFERENCES

(1) Adachi. T., F. Oka and M. Mimura (1985) : Descriptive Accuracy of Several Existing Constitutive Models for Normally Consolidated Clays., Proc. 5th ICONMIG, Vol. 1, pp. 259-266.

(2) Ishii. I., F. Ogawa and K. Zen (1984) : Engineering Properties of Marine Clays in Osaka Bay (Part 2) Physical Properties., Consolidation Characteristics and Permeability, Technical Note of the Port and Harbour Research Institute, Ministry of Transport, No. 498, pp. 47-86 (in Japanese).

(3) Ladd, C.C., R. Foott, K. Ishihara, F. Schlosser and H.G. Poulos (1977) : Stress-Deformation and Strength Characteristics, Proc. 9th ICSMFE, Vol. 2, pp. 421-494.

(4) Mimura. M. and H. Sekiguchi (1986) : Bearing Capacity and Plastic Flow of Rate-Sensitive Clay under Strip Loading., Bull. of D.P.R.I., Kyoto Univ., Vol. 36, Part 2, pp. 99-111.

(5) Sekiguchi. H. (1977) : Rheological Characteristics of Clays., Proc. 9th ICSMFE, Tokyo, Vol. 1, 1977, pp. 289-292.

(6) Sekiguchi. H., Y. Nishida and F. Kanai (1982) : A Plane-Strain Viscoplastic Constitutive Model for Clay., Proc. 37th National Conf., JSCE, pp. 181-182 (in Japanese).

(7) Sekiguchi. H. (1983) : Application of Plane-Strain Viscoplastic Constitutive Model for Clay., Proc. Annual Conf., Chubu Branch, JSCE, pp. 342-343 (in Japanese).

(8) Sekiguchi H., T. Shibata, A. Fujimoto and H. Yamaguchi (1986) : A Macro-Element Approach to Analyzing the Plane-Strain Behaviour of Soft Foundation with Vertical Drains., Proc. 31th Symposium, ICSMFE, pp. 111-120 (in Japanese).

(9) Sekiguchi, H., T. Shibata, M. Mimura and K. Sumikura (1988) : Behaviour of the Seawall and Bridge Abutment at the Edge of an Offshore Airport Fill., Annuals of the D.P.R.I., Kyoto Univ., No. 31 B-2, pp. 123-145 (in Japanese).

(10) Tsuchida. T., Y. Kikuchi, K. Nakashima and M. Kobayashi (1984) : Engineering Properties of Marine Clays in Osaka Bay (Part 3), Static Characteristics of Shear., Technical Note of the Port and Harbour Research Institute, Ministry of Transport, No. 498, pp. 87-114 (in Japanese).

(11) Yoshinaka, R. (1968) : Lateral Coefficient of Subgrade Reaction, Civil Engineering Journal, Vol. 10, No. 1, pp. 32-37 (in Japanese).

CHAPTER 9

Numerical Investigation on the Deformation of a Marine Foundation Subjected to Caisson-Composite Breakwater Construction

9-1. Introduction

A breakwater is indispensable to the security of harbor facilities and the anchorage of vessels, because it maintains calmness in the harbor by weakening/reflecting the wave energy from the open sea. Serenity can be confirmed for a small-scale harbor by a few hundred meters of breakwater, whereas an immense breakwater, extending over 1000 meters, must be constructed for harbors where large vessels drop anchors. Failure of the breakwater has such a harmful effect on harbor facilities, and daily human life in general, that it is of great significance that the stability of the breakwater and its foundation ground be confirmed. In regards to breakwater failure, cases exist where the composite breakwater with caissons at Niigata Fishing Port in Japan was destroyed by a billow caused by a 1976 typhoon, and the mound breakwater at Sines Port in Portugal was also damaged by a billow brought about by an earthquake and a storm in 1978. Both breakwaters were damaged not only by wave forces, but also because the clay foundation grounds remained poor without any soil reinforcement, where the rubble mound was formed, the caisson walls were set and the wave dissipating blocks were constructed.

In order to grasp the mechanism of ground deformation, a series of observational methods has been introduced to field construction and has produced remarkable results. However, it is obviously difficult to construct offshore structures while monitoring the deformation of the foundation ground, because instruments such as settlement plates, inclinometers and pore water pressure cells are so very hard to equip or install into a marine foundation ground and because much difficulty exists even in the

observation itself. And, in addition to the above problems, these instruments potentially obstruct the actual construction. For these reasons, almost no data exists on monitoring the deformation of breakwater foundation ground at the beginning of construction, and therefore, the deformation characteristics of a marine foundation subjected to breakwater construction have not been made clear thus far.

In this chapter, the South Breakwater at the New Nagasaki Fishing Port, which was damaged by Typhoon No. 12 in 1987, comes into question. Coupled stress-flow analyses are performed in terms of the elasto-viscoplastic finite element method to investigate the deformation of the breakwater foundation ground subjected to restoration of the damaged breakwater. The construction processes are modeled for the analyses as accurately as possible. Observations of the settlement and lateral displacement are also carried out using settlement plates and inclinometers equipped during the restoration. The stability and stress-strain characteristics of the breakwater foundation are discussed in detail by comparing the calculated performance with the measured results for both the settlement and the lateral displacement.

9-2. General Remarks on the South Breakwater of the New Nagasaki Fishing Port

9-2-1. Location and disaster of the South Breakwater

The South Breakwater of the New Nagasaki Fishing Port is located in the Mie district of Nagasaki City facing the Sea of Goto, in the southern part of the Nishisonogi Peninsula in Nagasaki Prefecture. The plan of the South Breakwater is shown in *Fig. 1*. This breakwater is one of the largest in Japan, extending to a length of 1090 meters. According to the August 31st morning edition of the Asahi Newspaper, the waves caused by the typhoon surged and upset the caissons, which were filled with an amount of sand equaling 9100 tons of force, by beating against the breakwater repeatedly with unforeseen magnitude. It was also reported that the South Breakwater suffered from a catastrophic disaster because the New Nagasaki

Fishing Port opens up to the Sea of Goto, and thus, there are few islands or peninsulas protecting the harbor from the ocean waves.

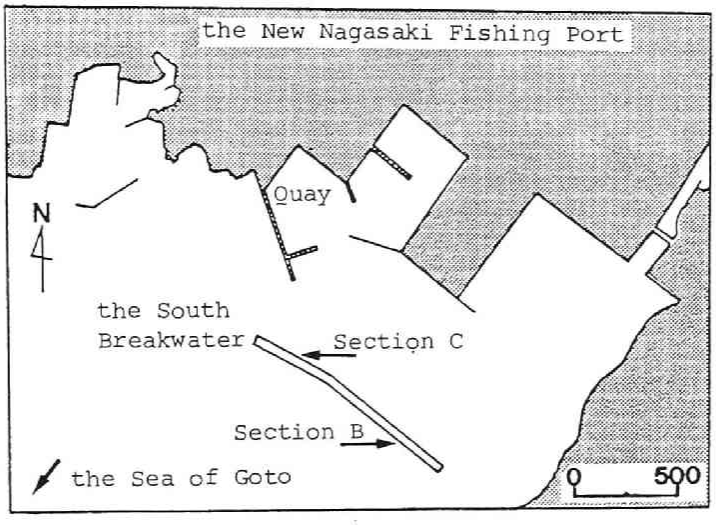

Fig. 1 Layout of the South Breakwater at the New Nagasaki Fishing Port

This breakwater was originally designed to maintain a safety factor of 1.2, by considering the design wave height to be 4.1 to 5.5 meters. According to the meteorological observatory, however, the maximum recorded wave height in the East China Sea due to the typhoon was 7.5 meters. Therefore, it may be assumed that the wave height in the Sea of Goto was probably almost equivalent to the height which was observed in the East China Sea.

The disaster chart for the South Breakwater is shown in *Fig. 2*. Almost all the caisson walls were upset in Section B for which there were no wave dissipating blocks on the sea side. On the other hand, caisson walls numbers 31 through 34 in Section B and 1 through 4 and 16 through 18 in Section C were not destroyed. The caisson walls which remained stable have wave dissipating blocks on the sea side.

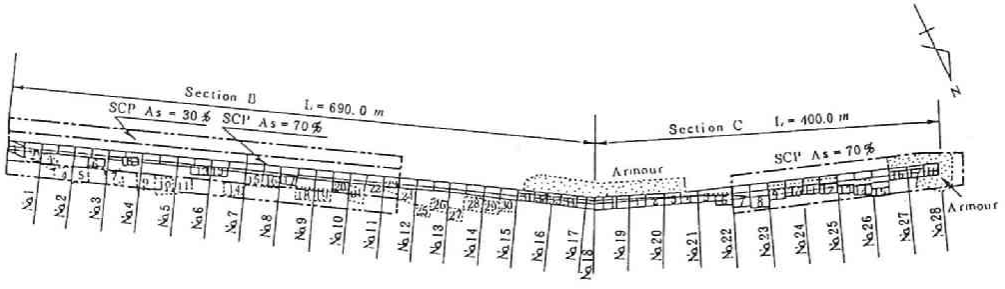

Fig. 2 Affected Position of the Caisson after the 1987 Typhoon

9-2-2. Geological Conditions

A series of soil explorations was carried out just after the destruction of the breakwater in 1987. As shown in *Fig. 3*, there are seven boreholes in Section B and four boreholes in Section C. In this study, coupled stress-flow analyses are performed along the B-2 line (investigation No. 6) and the C-2 line (investigation No. 26). The soil boring logs for the above-mentioned two sites are shown in *Fig. 4*. Both foundation grounds mainly consist of soft alluvial silt and have a couple of meters of loose sand layers at the seabed. There is also a thin sand seam between the thick silt layers. The bearing strata, consisting of mica schist appear at a depth of around *C.D.L.*-40 meters and have no diluvial clay deposits.

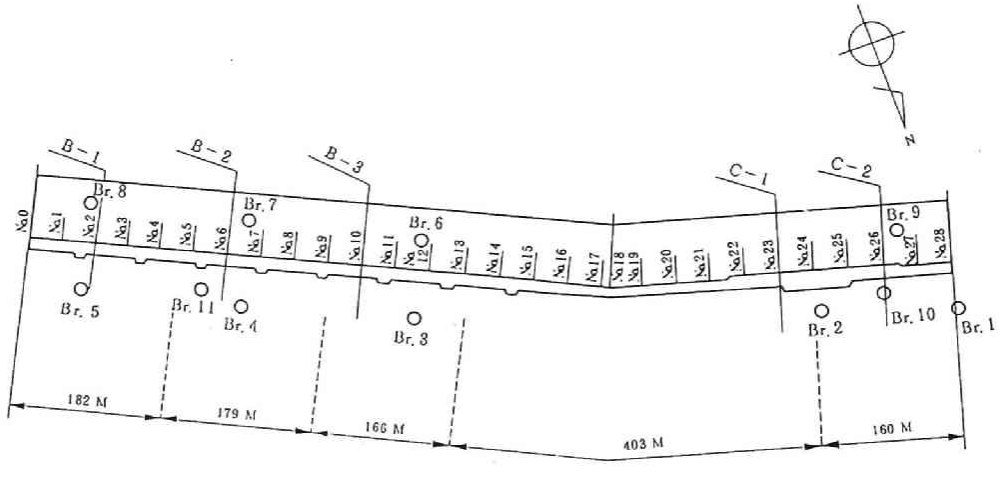

Fig. 3 Plan of Restoration for the Affected Area as well as the FEM Profiles and Boreholes

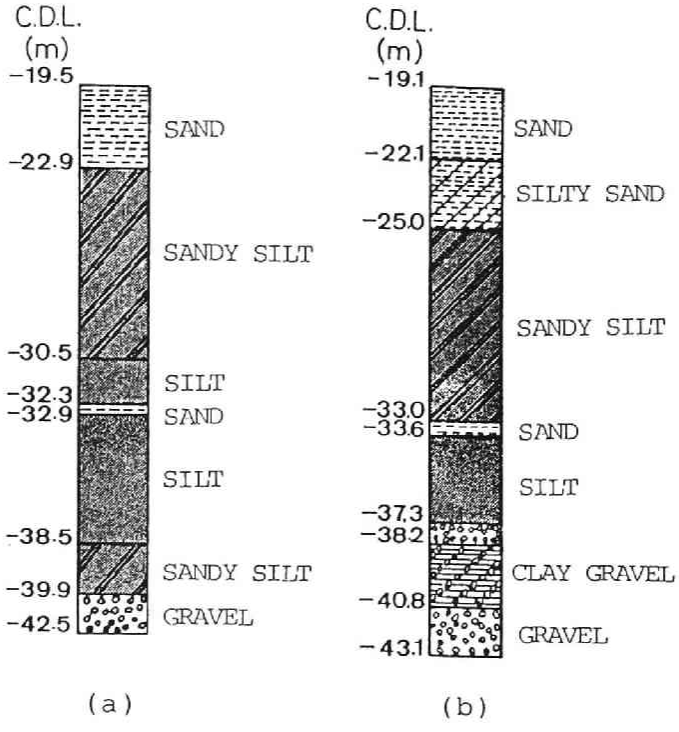

Fig. 4 Soil Boring Logs; (a) Boring No.7 at Section B, (b) Boring No.9 at Section C

9-2-3. Deformation Monitoring of the Foundation

Restoration of the South Breakwater had to be carried out in a short time and the cross-section of the restored breakwater was designed to be larger than the original one in order to stand up against wave forces which repeatedly attack the harbor. For this purpose, a large amount of rubble mound and wave dissipating blocks were set up on the unreinforced soft seabed. Naturally, attention must be paid to the failure of the foundation ground which might be caused by this rapid and large-scale breakwater construction. Therefore, the restoration was conducted by monitoring the deformation of the foundation ground subjected to the breakwater construction. Settlements of the seabed were measured by the settlement plates installed beneath the rubble mounds and armor blocks, and lateral displacement profiles were observed by the inclinometers.

9-3. Elasto-Viscoplastic Finite Element Analysis

9-3-1. Elasto-Viscoplastic Constitutive Model

The elasto-viscoplastic constitutive model used in this paper was proposed by Sekiguchi (1977). Sekiguchi *et al.*(1982) modified the model to a plane-strain version. The viscoplastic flow rule for the model is generally expressed as follows:

$$\dot{\varepsilon}_{ij}^{p} = \Lambda \frac{\partial F}{\partial \sigma_{ij}'} \tag{9-1}$$

in which F is the viscoplastic potential and Λ is the proportional constant. Viscoplastic potential F is defined as follows:

$$F = \alpha \cdot \ln \left[1 + \frac{\dot{v}_0 \cdot t}{\alpha} \exp\left(\frac{f}{\alpha}\right)\right] = v^p \tag{9-2}$$

in which a is a secondary compression index, $\dot{v}_0$ is the reference volumetric strain rate, f is the function in terms of effective stress and v^p is the viscoplastic volumetric strain. A concrete form of the model is shown in the reference (Mimura and Sekiguchi, 1986). The resulting constitutive relations are implemented into the finite element analysis procedure through the following incremental form:

$$\{\Delta\sigma'\} = [C^{ep}]\ \{\Delta\varepsilon\} - \{\Delta\sigma^R\} \tag{9-3}$$

Here, $\{\Delta\sigma'\}$ and $\{\Delta\varepsilon\}$ are the associated sets of effective stress increments and strain increments, respectively, and $[C^{ep}]$ stands for the elasto-viscoplastic coefficient matrix. The term $\{\sigma^R\}$ represents a set of 'relaxation stress' which increases with time when the strain is held constant.

The pore-water flow is assumed here to obey isotropic Darcy's law. In relation to this, it is further assumed that the coefficient of permeability, k, depends on the void ratio, e, in the following form:

$$k = k_0 \cdot \exp\left(\frac{e - e_0}{\lambda_k}\right) \tag{9-4}$$

in which k_0 is the initial value of k at $e=e_0$ and λ_k is a material constant governing the rate of change in permeability subjected to a change in void ratio. The drainage effect of sand drains driven into alluvial clay deposits is formulated by the macro-element method (Sekiguchi *et al.*, 1986).

The nodal displacement increments and element pore water pressure are taken as the primary unknowns of the problem. The finite element equations governing these unknowns are established on the basis of Biot's formulation and are solved numerically with the semi-band method of Gaussian elimination.

9-3-2. Finite Element Modeling and Soil Parameters

The regions selecting for the *FE* analysis are 300 meters long and 23 meters deep into the bearing stratum at a depth of *C.D.L.*-42.5 meters for Section B and 370 meters long and 23.5 meters deep into the bearing stratum at a depth of *C.D.L.*-43.1 meters for Section C, based on the soil boring logs shown in *Fig. 4*. The original foundation grounds for Sections B and C are then modeled as shown in *Fig. 5* and *6*, respectively. For both sections, the marine foundation is divided into 15 layers. The sand layer existing inside the alluvial silt layer is assumed to be a perfectly drained elastic material in which no excess pore water pressure can be generated when subjected to loading. In the analyses here, the area reinforced by densely compacted sand (*SCP*) is also modeled into finite elements. Considering the reduction in settlement, the settlement reduction factor, b (Aboshi *et al.*, 1982), is introduced. The compression index, swelling index and secondary compression index are changed respectively with the following empirical relations.

$$\lambda = \beta\,\lambda\,,\ \kappa = \beta\,\kappa\,,\ \alpha = \beta\,\alpha$$

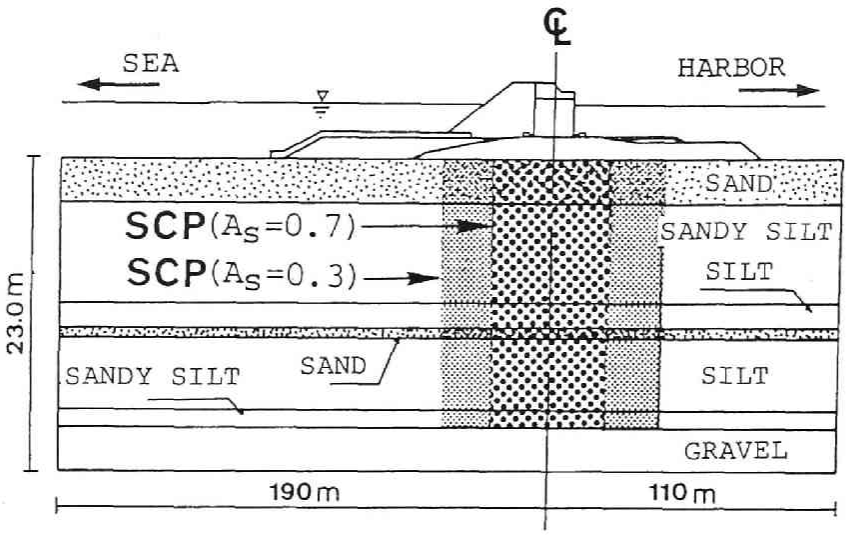

Fig. 5 Cross-section of the Foundation at Section B

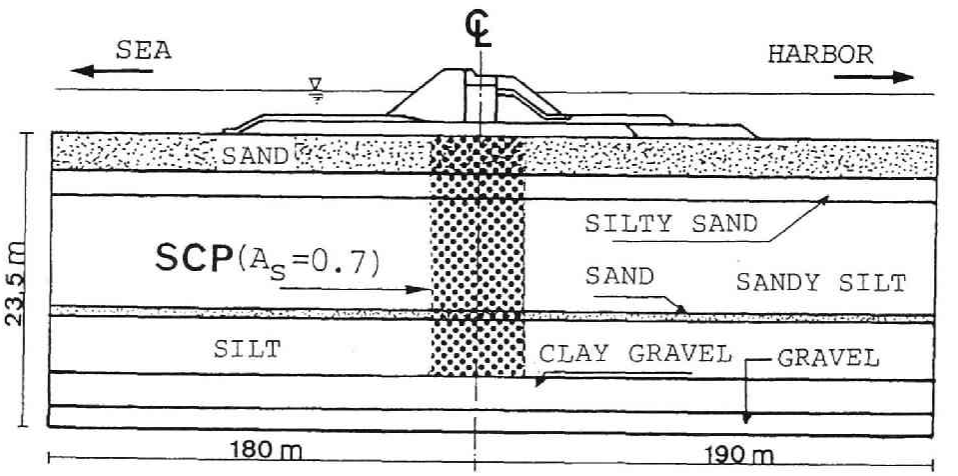

Fig. 6 Cross-section of the Foundation at Section C

Here, β is assumed to be the function of the replacement ratio, a_S. Therefore, the value of β can then be determined by the following relation.

$$\beta = 1 - a_S$$

In Section B, the alluvial deposit just beneath the caisson is improved by *SCP* with an a_S value of 70 % and both sides of this area are also improved in the same way with an a_S value of 30 %. In Section C, on the other hand, only the alluvial deposit beneath the caisson is reinforced by *SCP* with an a_S value of 70 %. The drainage effect of these *SCP* reinforced areas is also formulated by the macro-element method (Sekiguchi *et al.*, 1986).

The values of the soil parameters of the foundation ground used in this study are summarized in *Tables-1* and *2* for both sections. The specified way to determine the physical properties is explained in detail in the references (Sekiguchi *et al.*, 1988; Mimura *et al.*, 1989).

Table-1 Values of the Principal Soil Parameters Adopted for the Ground under the Original Seabed (Section B)

(tm・day)

MTYP	λ	κ	M	α	$\dot{v}_0$ (day^{-1})	ν'	G_0 (tf/m^2)	σ_{v_0}' (tf/m^2)	K_0(nc)	e_0	k_0 (m/day)	λ_k
15	—	—	—	—	—	0.33	158	0.60	0.47	1.00	0.86	0.012
14	0.012	0.006	1.3	1.8×10^{-4}	1.8×10^{-5}	0.33	158	1.35	0.47	1.00	0.86	0.012
13	0.189	0.019	1.3	2.1×10^{-3}	2.1×10^{-6}	0.36	136	3.10	0.56	1.68	1.3×10^{-3}	0.120
12	0.189	0.019	1.3	2.1×10^{-3}	2.1×10^{-6}	0.36	189	4.31	0.56	1.68	1.3×10^{-3}	0.120
11	0.189	0.019	1.3	2.1×10^{-3}	2.1×10^{-6}	0.36	242	5.52	0.56	1.68	1.3×10^{-3}	0.120
10	0.189	0.019	1.3	2.1×10^{-3}	2.1×10^{-6}	0.36	294	6.72	0.56	1.68	1.3×10^{-3}	0.120
9	0.240	0.024	1.3	2.7×10^{-3}	2.7×10^{-6}	0.36	173	7.93	0.56	1.68	1.3×10^{-3}	0.270
8	0.240	0.024	1.3	2.7×10^{-3}	2.7×10^{-6}	0.36	199	9.10	0.56	1.68	1.3×10^{-3}	0.270
7	—	—	—	—	—	0.33	316	10.0	0.50	1.00	0.86	0.032
6	0.280	0.028	1.3	3.2×10^{-3}	3.2×10^{-6}	0.36	204	10.9	0.56	1.64	4.9×10^{-4}	0.310
5	0.280	0.028	1.3	3.2×10^{-3}	3.2×10^{-6}	0.36	227	12.1	0.56	1.64	4.9×10^{-4}	0.310
4	0.280	0.028	1.3	3.2×10^{-3}	3.2×10^{-6}	0.36	249	13.3	0.56	1.64	3.5×10^{-4}	0.300
3	0.280	0.028	1.3	3.2×10^{-3}	3.2×10^{-6}	0.36	272	14.5	0.56	1.64	3.5×10^{-4}	0.300
2	—	—	—	—	—	0.33	824	15.9	0.50	1.00	0.86	—
1	—	—	—	—	—	0.33	824	17.3	0.50	1.00	0.86	—

Table-2 Values of the Principal Soil Parameters Adopted for the Ground under the Original Seabed (Section C)

(tm・day)

MTYP	λ	κ	M	α	$\dot{v}_0$ (day^{-1})	ν'	G_0 (tf/m^2)	σ_{v0}' (tf/m^2)	K_0 (nc)	e_0	k_0 (m/day)	λ_k
15	—	—	—	—	—	0.33	182	0.75	0.47	1.00	0.86	0.012
14	0.012	0.006	1.3	1.8×10^{-4}	1.8×10^{-5}	0.33	182	2.80	0.47	1.00	0.86	0.012
13	0.217	0.022	1.3	2.3×10^{-3}	2.3×10^{-6}	0.36	220	4.72	0.56	1.56	1.3×10^{-3}	0.120
12	0.217	0.022	1.3	2.3×10^{-3}	2.3×10^{-6}	0.36	266	5.71	0.56	1.56	1.3×10^{-3}	0.120
11	0.240	0.024	1.3	2.8×10^{-3}	2.8×10^{-6}	0.36	155	6.65	0.56	1.56	3.0×10^{-4}	0.240
10	0.240	0.024	1.3	2.8×10^{-3}	2.8×10^{-6}	0.36	186	7.96	0.56	1.56	3.0×10^{-4}	0.240
9	0.240	0.024	1.3	2.8×10^{-3}	2.8×10^{-6}	0.36	217	9.30	0.56	1.56	3.6×10^{-4}	0.230
8	0.240	0.024	1.3	2.8×10^{-3}	2.8×10^{-6}	0.36	264	11.2	0.56	1.56	3.6×10^{-4}	0.230
7	—	—	—	—	—	0.33	316	12.6	0.50	1.00	0.86	0.032
6	0.250	0.025	1.3	3.2×10^{-3}	3.0×10^{-6}	0.36	296	13.4	0.56	1.52	8.2×10^{-4}	0.180
5	0.250	0.025	1.3	3.2×10^{-3}	3.0×10^{-6}	0.36	326	14.8	0.56	1.52	8.2×10^{-4}	0.180
4	0.280	0.028	1.3	3.2×10^{-3}	3.3×10^{-6}	0.36	319	16.2	0.56	1.52	3.5×10^{-4}	0.180
3	0.280	0.028	1.3	3.2×10^{-3}	3.3×10^{-6}	0.36	349	17.7	0.56	1.52	3.5×10^{-4}	0.180
2	—	—	—	—	—	0.33	824	19.2	0.50	1.00	0.86	—
1	—	—	—	—	—	0.33	824	20.2	0.50	1.00	0.86	—

As far as the breakwater construction is concerned, finite elements corresponding to the designed construction sequence are generated according to circumstances. As a result, we have 745 nodes and 679 elements for Section B, and 826 nodes and 759 elements for Section C.

The construction sequences for Sections B and C are shown in *Fig. 7* and *8*, respectively. The loading processes for the finite element analyses are modeled with these construction sequences as accurately as possible. The completed cross-sections for both sections are shown in *Figs. 9* and *10*.

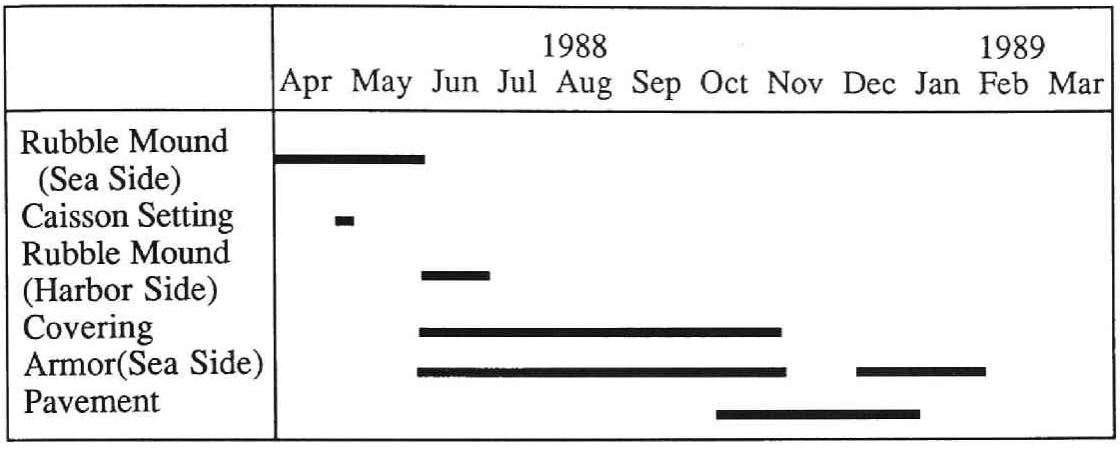

Fig. 7 Sequence of Breakwater Construction at Section B

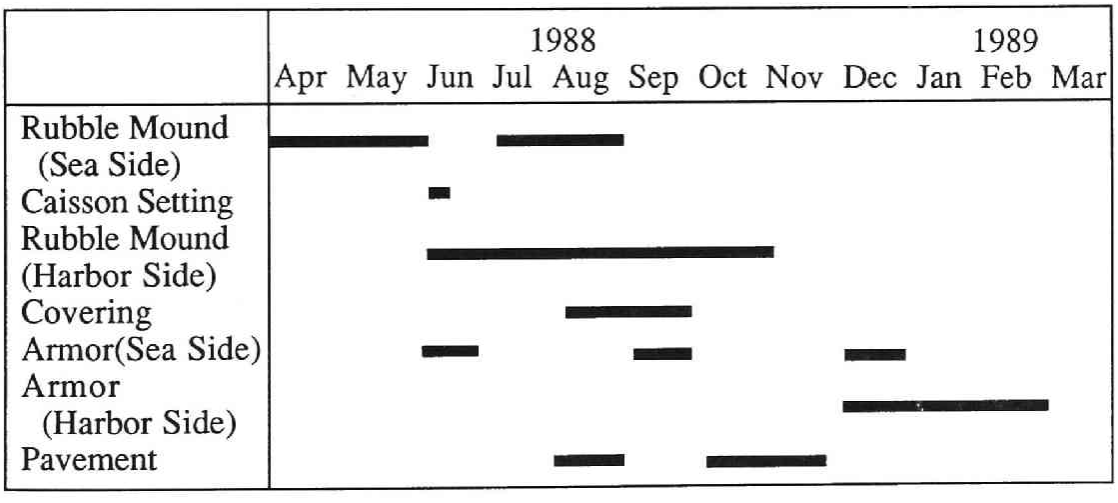

Fig. 8 Sequence of Breakwater Construction at Section C

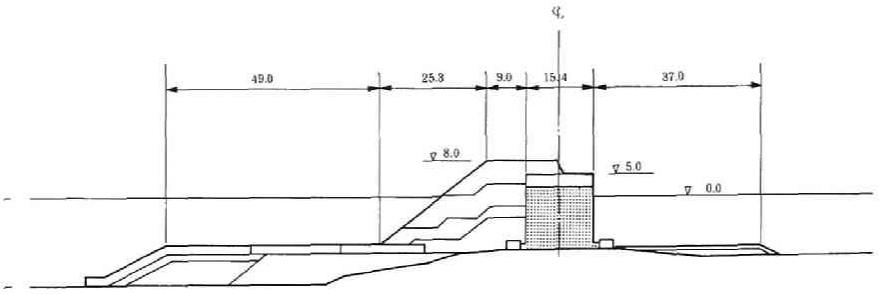

Fig. 9 Cross-section of the Breakwater (Section B)

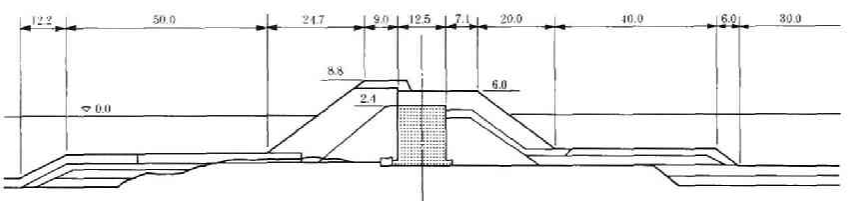

Fig. 10 Cross-section of the Breakwater (Section C)

9-4. Calculated Performance of the Breakwater Foundation

9-4-1. Settlement Profiles of the Seabed

Calculated settlement profiles of the seabed for Sections B and C are shown in *Figs. 11* and *12*, respectively. In *Fig. 11*, the solid curve shows the settlement profile of the seabed due to the rubble mound constructed 12 years ago, and thus, it represents the shape of the foundation ground just before the initiation of the breakwater restoration. The hatched line represents the completion of the pavement, the chain-dotted line is for the completion of the breakwater construction and the chain double-dotted line

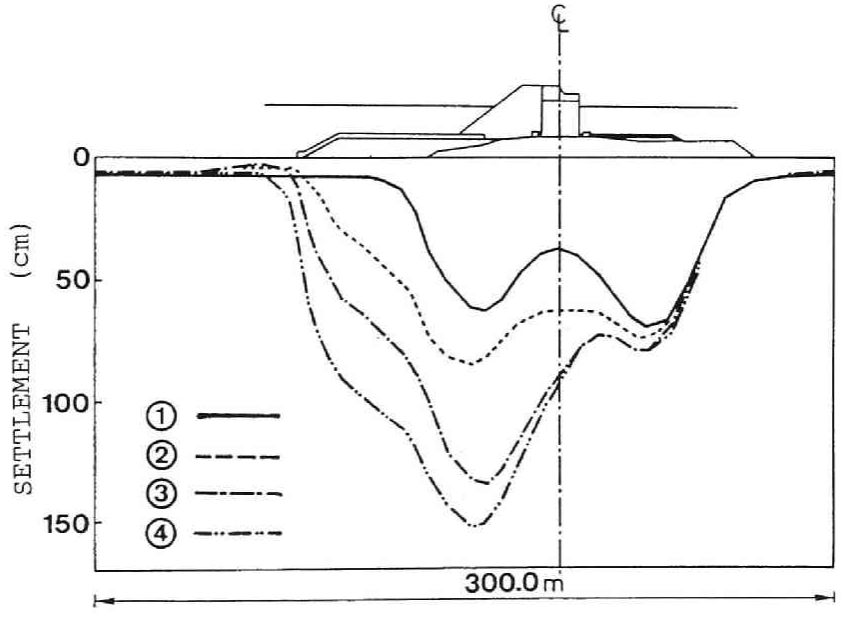

Fig. 11 Calculated Settlement Profiles of the Seabed (Section B);
1 : Existing Rubble Mound, 2 : Pavement, 3 : Completion of Construction, 4 : A Year after Completion of Construction

shows the profile a year after the breakwater construction. In *Fig. 12*, the solid, chain-dotted and chain double-dotted lines denote the settlement profiles for the same points as those in *Fig. 11*. The hatched line, however, shows the profile at the completion of the covering on the sea side. Because the foundation grounds have been reinforced by *SCP* beneath the caissons

for both sections and for the adjacent area in Section B, settlement in the reinforced area is controlled, whereas that taking place at the boundary between the reinforced and unreinforced areas is predominant. The calculated maximum settlement on both sites also occurs here, and it reaches 1.55 meters for Section B and 1.54 meters for Section C, a year after the completion of the breakwater construction.

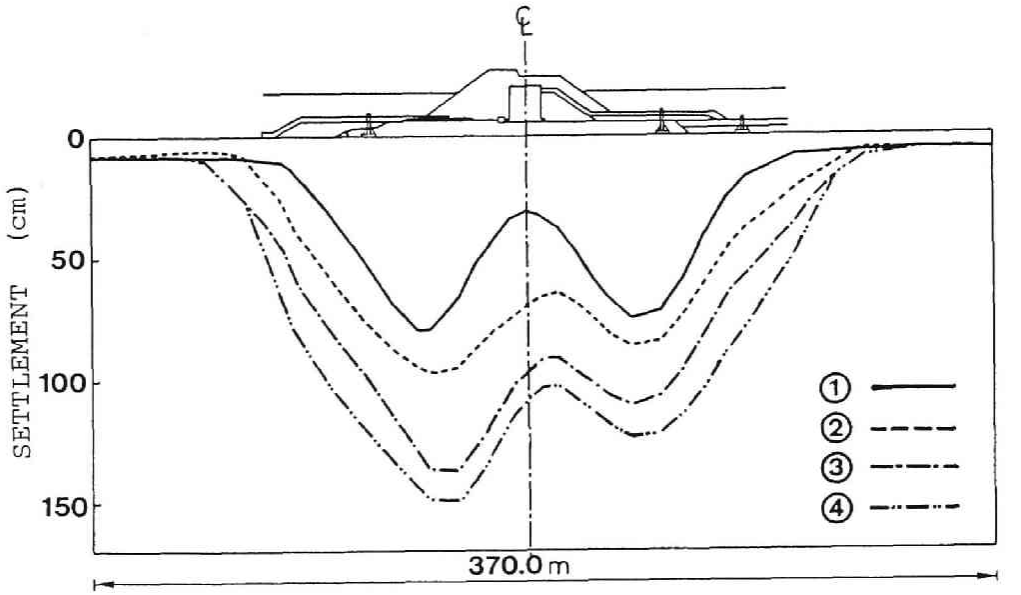

Fig. 12 Calculated Settlement Profiles of the Seabed (Section C);
1 : Existing Rubble Mound, 2 : Covering on the Sea Side,
3 : Completion of Construction, 4 : A Year after Completion of Construction

9-4-2. Time-Settlement Performance of the Seabed

Calculated time-settlement relations of the seabed beneath the caissons are shown in *Figs. 13 (a)* and *(b)*. The initiation of the breakwater restoration is adopted here as the reference time for these relations. A remarkable settlement occurs just after the caissons in both sections have been set and filled. The marine foundation ground begins to subside again with the pavement and construction of the armor units (wave dissipating blocks). For Section B (*Fig. 13 (a)*), after the settlement increases due to a

raising of the armor units (wave dissipating blocks), the marine foundation becomes stable as consolidation is promoted. The calculated settlement of the seabed subjected to breakwater restoration is 0.56 meters at the completion of the construction. On the other hand, the calculated settlement of the seabed for Section C is 0.66 meters at the completion of the construction (*Fig. 13(b)*).

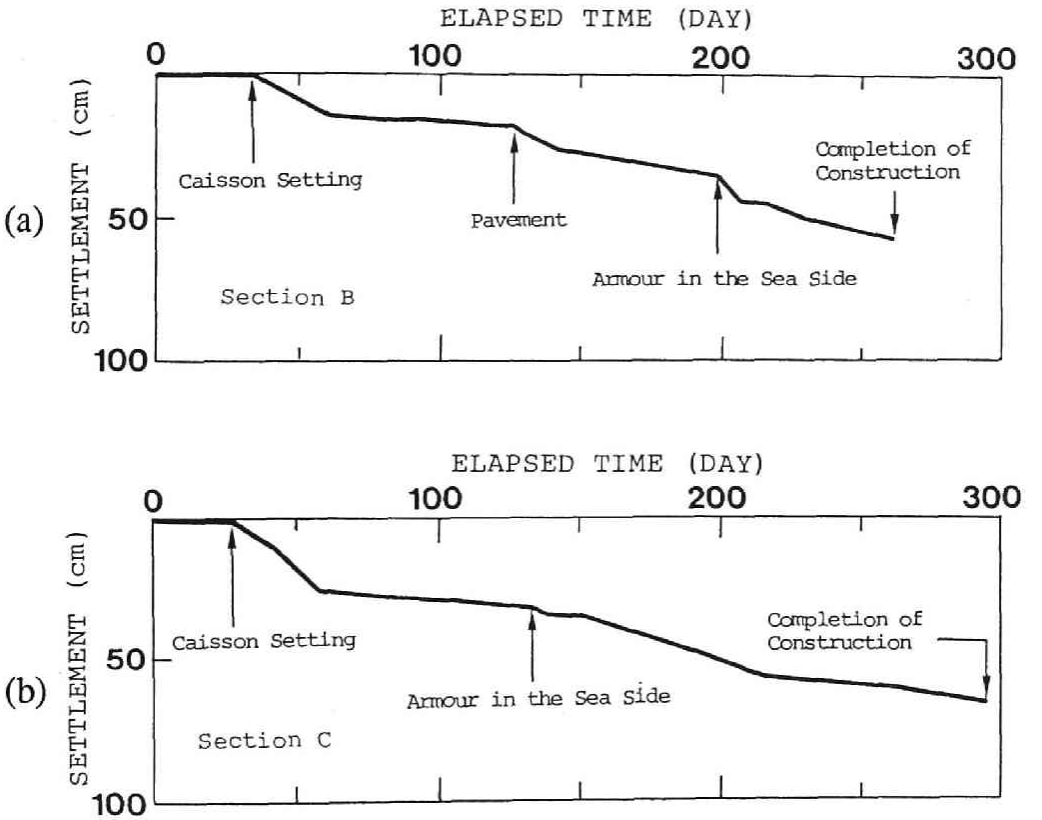

Fig. 13 Calculated Time-Settlement Performance of the Seabed beneath the Caisson Wall; (a) : Section B, (b) : Section C

9-4-3. Long-Term Settlement of the Foundation

Calculated excess pore water pressure profiles with depth for Sections B and C are shown in *Figs. 14 (a)* and *(b)*, respectively. Both places selected are untreated areas where much time is required for the excess pore water pressure to dissipate, because the long-term settlement is

mainly governed by this process of excess pore water pressure dissipation. The point selected for Section B is 70 meters seaward from the center line of the breakwater and that for Section C is 55 meters seaward from the center line of the breakwater. In *Fig. 14*, the solid lines *(1)* denote the

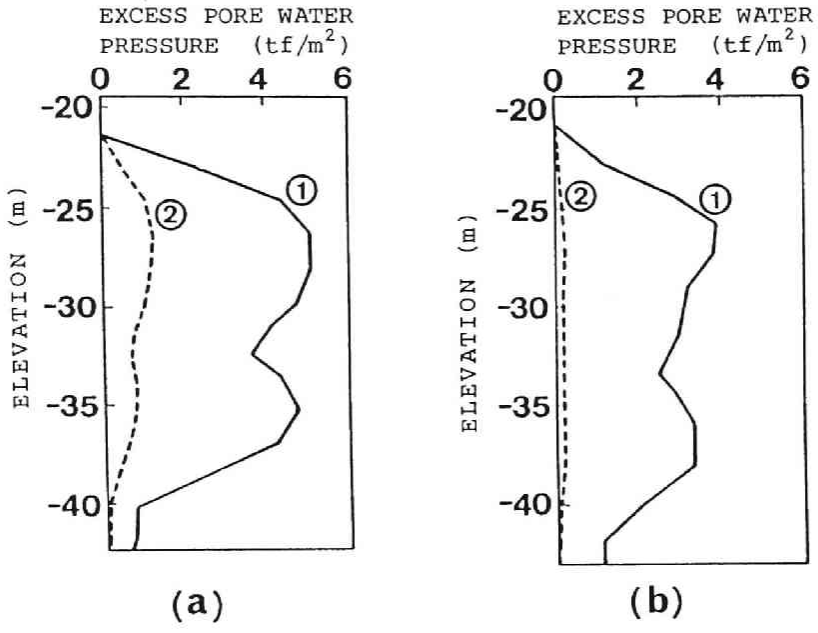

Fig. 14 Calculated Excess Pore Water Pressure Dissipation beneath the Rubble Mound; (a) : Section B, (b) : Section C
(1 : at the Completion of Construction, 2 : A Year after Completion of Construction)

profiles at the completion of the breakwater construction and the hatched lines *(2)* denote the profiles a year after the completion of the breakwater construction. As a result of the generation and dissipation of the pore water pressure during the construction process, the calculated excess pore water pressure profiles are obtained as shown in *Fig. 14*. Although the maximum values of the excess pore water pressures, 5.1 tonf/m^2 for Section B and 3.9 tonf/m^2 for Section C, are reached at the completion of the breakwater construction, they are almost entirely dissipated by a year after the completion of the breakwater construction. Judging from the excess pore water pressure distribution, the primary consolidation of the marine foundation is nearly finished a year after the completion of the breakwater construction. And, as can be observed from the boring logs shown in *Fig. 4*, the foundation ground consists of thick silt deposits. Compared with

clay, silt is characterized by having a larger permeability and a smaller secondary compression. For these reasons, deformations of the marine foundation ground for both sections are almost completed by a year after finishing the breakwater construction, and a large, long-term settlement can be ruled out for the South Breakwater.

9-4-4. Lateral Displacement Profiles

Lateral displacement profiles are investigated at points *P* and *Q* in Section B, as shown in *Fig. 15 (a)*, and at points *X*, *Y* and *Z* for Section C, as shown in *Fig. 15 (b)*. The places selected here for the investigation of the calculated performance correspond to those where the inclinometers were installed to monitor the *in situ* lateral displacement. The monitored data will be compared with the calculated performance and discussed later.

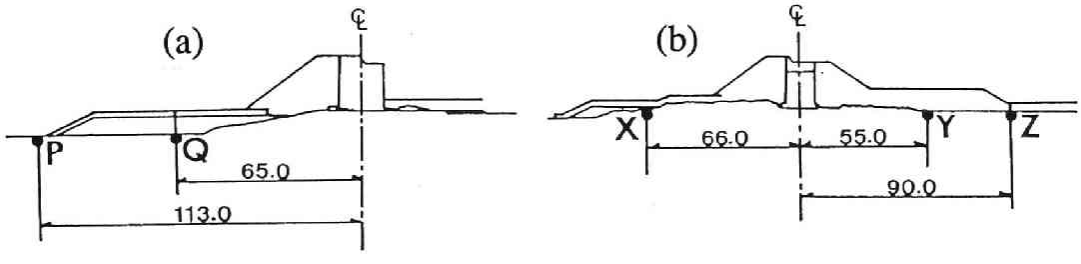

Fig. 15 Investigated Point for Lateral Displacement; (a) : Section B, (b) : Section C

Lateral displacement profiles with depth for Section B are shown in *Figs. 16 (a)* and *(b)*. In these figures, the solid curves show the lateral displacement profiles due to a rubble mound constructed 12 years ago. Thus, they represent the shape of the foundation ground just before the initiation of the breakwater restoration. The hatched lines represent the completion of the pavement, the chain-dotted lines are for the completion of the breakwater construction and the chain double-dotted lines show the profiles a year after the breakwater construction. Lateral ground movement in a seaward direction takes place as the caisson is set and the armor units (wave dissipation blocks) are constructed on the sea side. The profiles peak at the boundary between the alluvial silt deposit and the sand layer on the seabed, and deformation is restrained in the sand layer by the

restriction effect of the sand layer. The calculated total maximum lateral displacement a year after the completion of the breakwater construction is 0.23 meters.

At the point, *Q* in *Fig. 16 (b)*, a larger lateral displacement occurs at the completion of the breakwater construction than at point *Q* in *Fig. 16 (a)*, because the effect of the armor units (wave dissipating blocks) construction is severer and the deformation in the direction of the caisson is suppressed by the *SCP* reinforced foundation. The calculated total maximum lateral displacement a year after the completion of the breakwater construction is 0.34 meters at the boundary between the alluvial silt deposit and the sand layer of the seabed, which is the same as point *P* shown in *Fig. 16 (a)*.

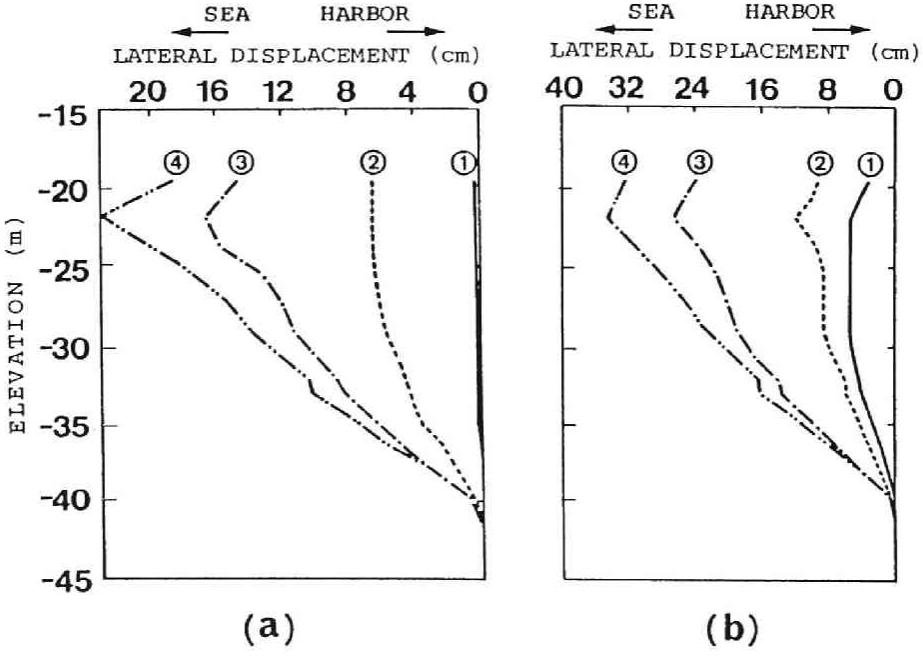

Fig. 16 Calculated Profiles of Lateral Displacement with Depth (Section B); (a) : at the Toe of the Covering, (b) : beneath the Rubble Mound, (1 : Existing Rubble Mound, 2 : Pavement, 3 : Completion of Construction, 4 : A Year after Completion of Construction)

Next, for Section C, lateral displacement profiles with depth are shown in *Figs. 17 (a),(b)* and *(c)*. In these figures, the solid, chain-dotted and chain double-dotted lines denote the lateral displacement profiles for the same points as those in *Fig. 16*. The hatched lines show the profile at the completion of the covering on the sea side. Large lateral displacements take place due to the rubble mound formation and armor units (wave dissipating blocks) construction at point *X*, as shown in *Fig. 17 (a)*. The lateral movement of the marine foundation is also restrained by the sand layer of the seabed, and the maximum lateral displacement occurs at the boundary between the alluvial deposit and the sand layer of the seabed with a value of 0.31 meters a year after the completion of the breakwater construction.

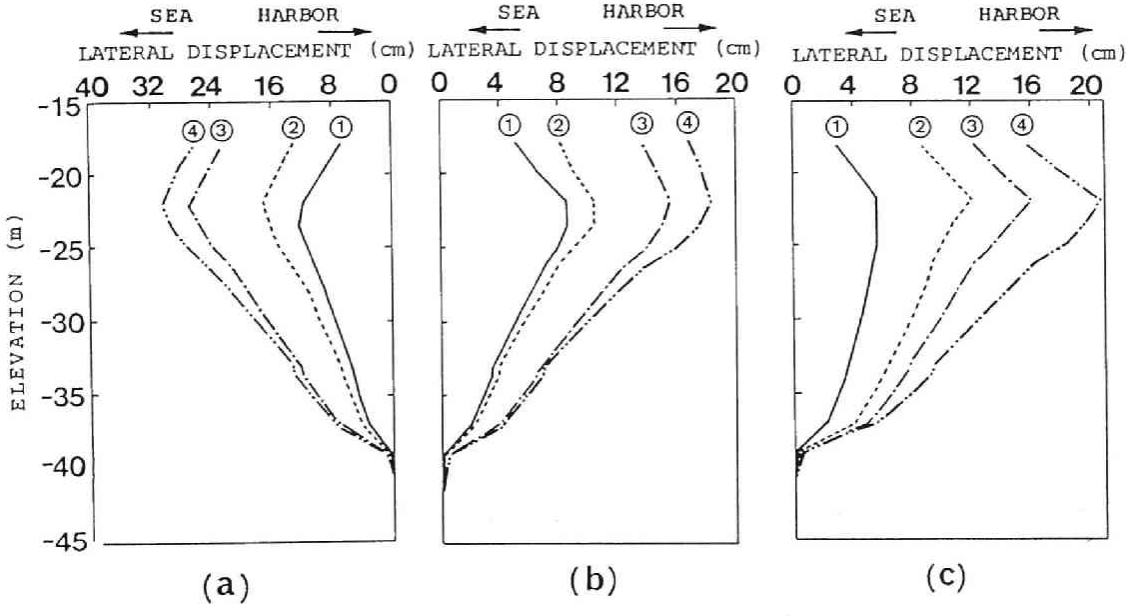

Fig. 17 Calculated Profiles of Lateral Displacement with Depth (section C); (a) : beneath the Rubble Mound on the Sea Side, (b) : beneath the Rubble Mound on the Harbor Side, (c) : beneath the Rubble Mound on the Harbor Side, (1 : Existing Rubble Mound, 2 : Pavement, 3 : Completion of Construction, 4 : A Year after Completion of Construction)

In *Figs. 17 (b)* and *(c)*, the shapes of the lateral displacement profiles with depth for points *Y* and *Z* show a close resemblance and are restrained by the sand layers with peaks at the boundary between the alluvial silt deposits and the sand layers of the seabed. The maximum values are 0.18 meters for point *Y* and 0.21 meters for point *Z*.

9-4-5. Effective Stress Path

The stability of the marine foundation ground during the breakwater construction is investigated by pursuing the transition of effective stress of the foundation due to the breakwater construction in this section. For Section B, the selected elements are located in the middle of the silt deposits at a depth of *C.D.L.* -25.4 to -27.1 meters. The effective stress paths are shown in *Fig. 18; (a)* 70 meters seaward from the center line of the breakwater, *(b)* 36 meters harbor side from the center line of the breakwater, *(c)* beneath the caisson. In these figures, numbers *1* through *5* represent the construction stages; that is, *1* : rubble mound formation on the sea side, *2* : caisson setting, *3* : armor units (wave dissipating blocks) construction, *4* : covering and *5* : completion of the construction. In *Fig. 18 (a)*, the effective stress path approaches the failure line by dropping a large amount of rubble onto the marine foundation to form a rubble mound, as shown by *1*. Careful attention must be paid to this undrained response because it often leads directly to failure. The stress state becomes stable, however, by means of subsequent consolidation. A temporary reduction in the effective stress can be seen again when the armor units (wave dissipating blocks) are constructed *4*, but in general, the effective stress path moves along the K_0 line stably. The variation in stress is not so remarkable in *Fig. 18 (b)* although the lateral stress once increases due to the setting and filling of the caisson *2* for the element on the harbor side.

The marine foundation ground beneath the caisson has been reinforced by *SCP*. The rigidity of this treated area has increased. In *Fig. 18 (c)*, both effective stress and shear stress grow larger due to a concentration of stress induced by this increase in rigidity of the foundation ground. The breakwater has been stably constructed *5*, however, and there are no indications of failure.

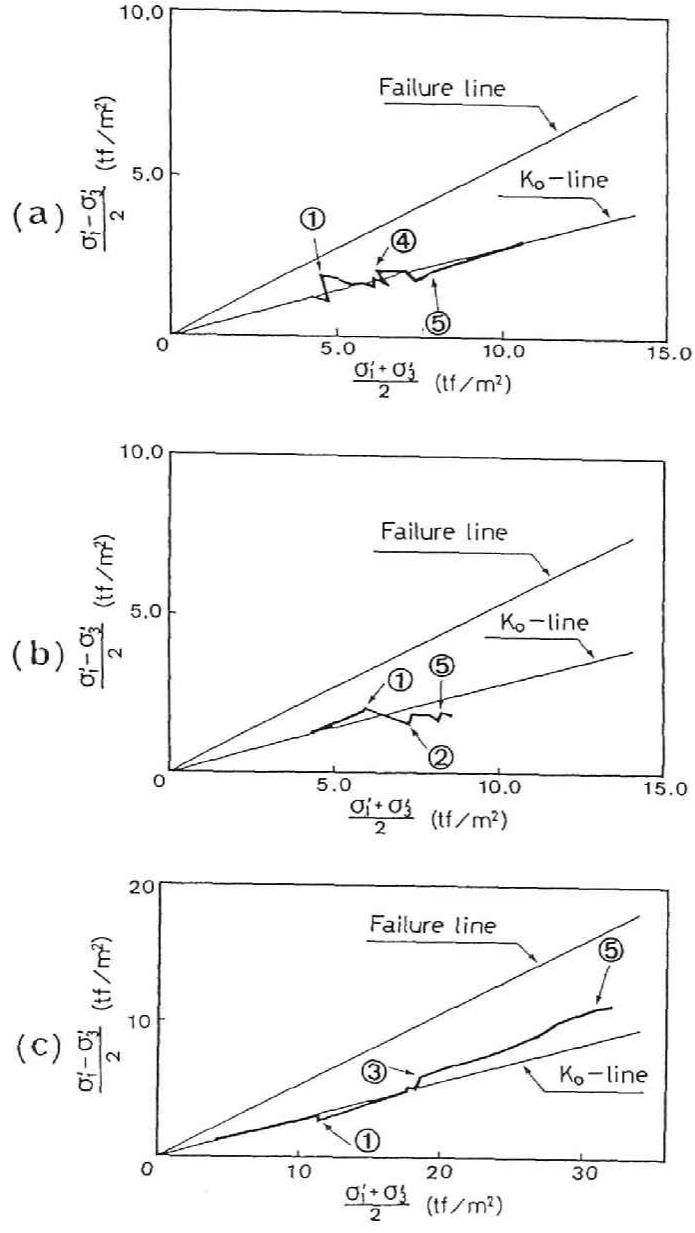

Fig. 18 Effective Stress Paths for Silt Layer at Section B ;
(a) : beneath the Rubble Mound on the Sea Side,
(b) : beneath the Rubble Mound on the Harbor Side,
(c) : beneath the Caisson Wall,
(1 : Existing Rubble Mound, 2 : Caisson Setting, 3 : Armor Construction, 4 : Covering, 5 : Completion of Construction)

With these results from the effective stress paths for Section B, it is concluded that the breakwater foundation has deformed stably during the whole process of restoration.

For Section C, the selected elements are located at a depth of *C.D.L.* -25.0 to -26.5 meters and are also in the middle of the silt deposits. The effective stress paths are shown in *Fig. 19*, namely, *(a)* 50 meters seaward from the center line of the breakwater, *(b)* 60 meters harbor side from the center line of the breakwater and *(c)* beneath the caisson. In these figures, numbers *1* through *3* represent the construction stages, that is, *1* : rubble mound formation on the sea side, *2* : caisson setting and *3* : completion of construction. Stress states are stable on both the sea side and the harbor side (*Figs. 19 (a)* and *(b)*), while a slight increase in lateral stress due to the caisson setting *2* is seen on the harbor side (*Fig. 19 (a)*). In *Fig. 19 (c)*, the stability of the foundation ground beneath the caisson, which is reinforced by *SCP*, is also confirmed with relatively larger effective and shear stresses produced by an increase in rigidity by the *SCP*. Construction progressed stably and the breakwater was completed *3* under a safe condition of stress.

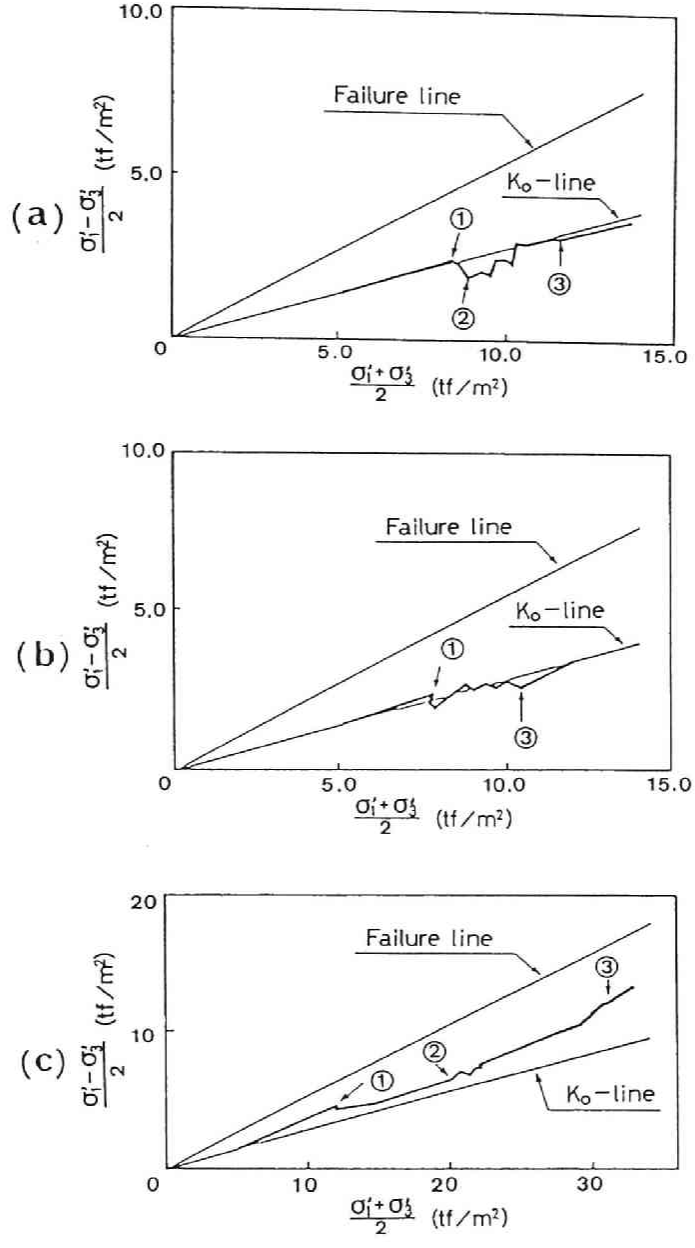

Fig. 19 Effective Stress Paths for Silt Layer at Section C ;
(a) : beneath the Rubble Mound on the Sea Side,
(b) : beneath the Rubble Mound on the Harbor Side,
(c) : beneath the Caisson Wall,
(1 : Existing Rubble Mound, 2 : Caisson Setting,
3 : Completion of Construction)

9-5. Comparison of the Calculated and Monitored Performance

The settlement of the seabed and the lateral displacement with depth have been monitored for the South Breakwater by the settlement plates and inclinometers equipped in March of 1988 when the restoration of this breakwater was initiated. In this section, the calculated performances are compared with the monitored settlement and lateral displacement. The locations of the settlement plates and inclinometers are shown in *Fig. 20* for Section B and in *Fig. 21* for Section C.

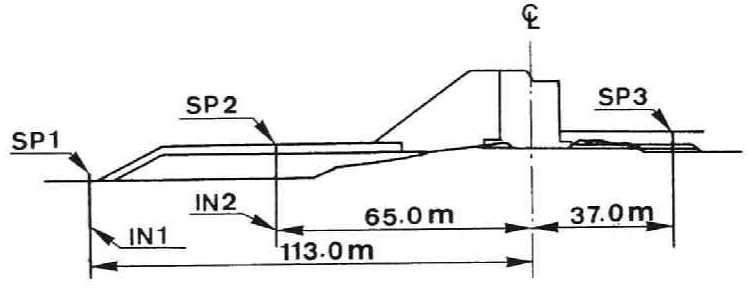

Fig. 20 Layout of Instruments in Section B

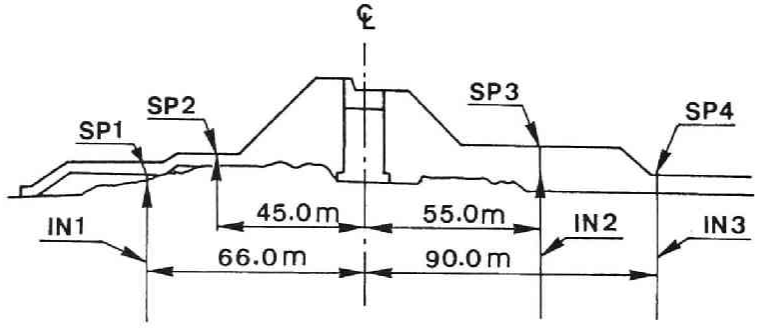

Fig. 21 Layout of Instruments in Section C

For Section B, *SP1* (Settlement plate No.1) and *IN1* (Inclinometer No.1) have been equipped at the toe of the covering, 113 meters seaward from the the center line of the breakwater, *SP2* and *IN2* have been installed beneath the rubble mound, 65 meters seaward and *SP3* has been set 37 meters harbor side from the center line of the breakwater, as shown in *Fig. 20*. For Section C, *SP1* and *IN1* have been equipped beneath the rubble mound, 66 meters seaward from the center line of the breakwater, *SP2* has been set beneath the covering, 45 meters sea ward, *SP3* and *IN2* have been

installed 37 meters harbor side and *SP4* and *IN3* have been equipped 90 meters harbor side from the center line of the breakwater, as shown in *Fig. 21*.

9-5-1. Time-Settlement Relations

A series of comparisons of the time-settlement relations for Section B are shown in *Figs.22 (a), (b)* and *(c)*. In *Fig. 22 (a)*, the immediate settlement was monitored for *SP1*, although no load was applied here. The calculated performance shows no settlement reflecting this construction sequence. Also in *Fig. 22 (b)*, a much larger settlement was monitored for *SP2*, and the calculated performance shows a completely different time-settlement relation. Immediate settlements due to a rubble mound formation or covering can be described by *FEM*, as indicated in this figure. However, the large settlements which were monitored take place in the primary stage and cannot be rationally explained. The reasons for this discrepancy will be discussed later. In *Fig. 22 (c)*, there is little settlement on the harbor side of the breakwater because no structures were built on the marine foundation there. Thus the calculated and monitored performances are in good agreement.

A series of comparisons of time-settlement relations for Section C are shown in *Fig. 23*. Firstly, we investigate the performance on the sea side (see *Figs.23 (a)* and *(b)*). The calculated performances show a remarkable subsidence due to the rubble mound formation, covering equipment and armor units (wave dissipating blocks) construction. The monitored relations show a larger deformation than those calculated in the primary stage, before the armor units (wave dissipation blocks) construction, but a good agreement can be seen in the subsequent construction process. On the other hand, a much larger settlement takes place on the harbor side as compared with the calculated performance, as shown in *Figs. 23 (c)* and *(d)*.

Let us discuss the reasons for this discrepancy which are the same as those which also appear for Section B (*Fig. 22 (b)*). The settlement plates have been fixed by the dropping of rubble onto the seabed in order to

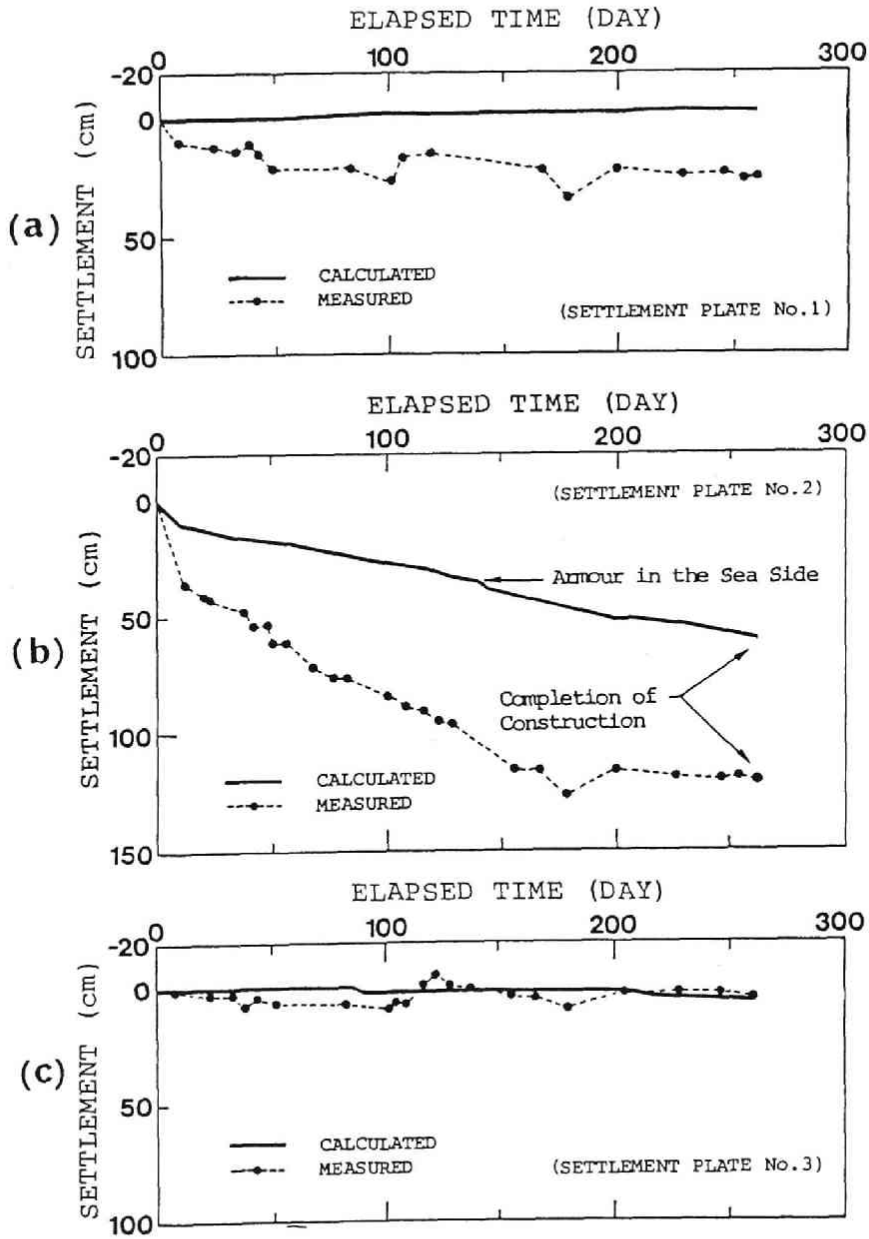

Fig. 22 Time Settlement Performance (Section B); (a) : Settlement Plate No. 1, (b) Settlement Plate No. 2, (c) Settlement Plate No. 3

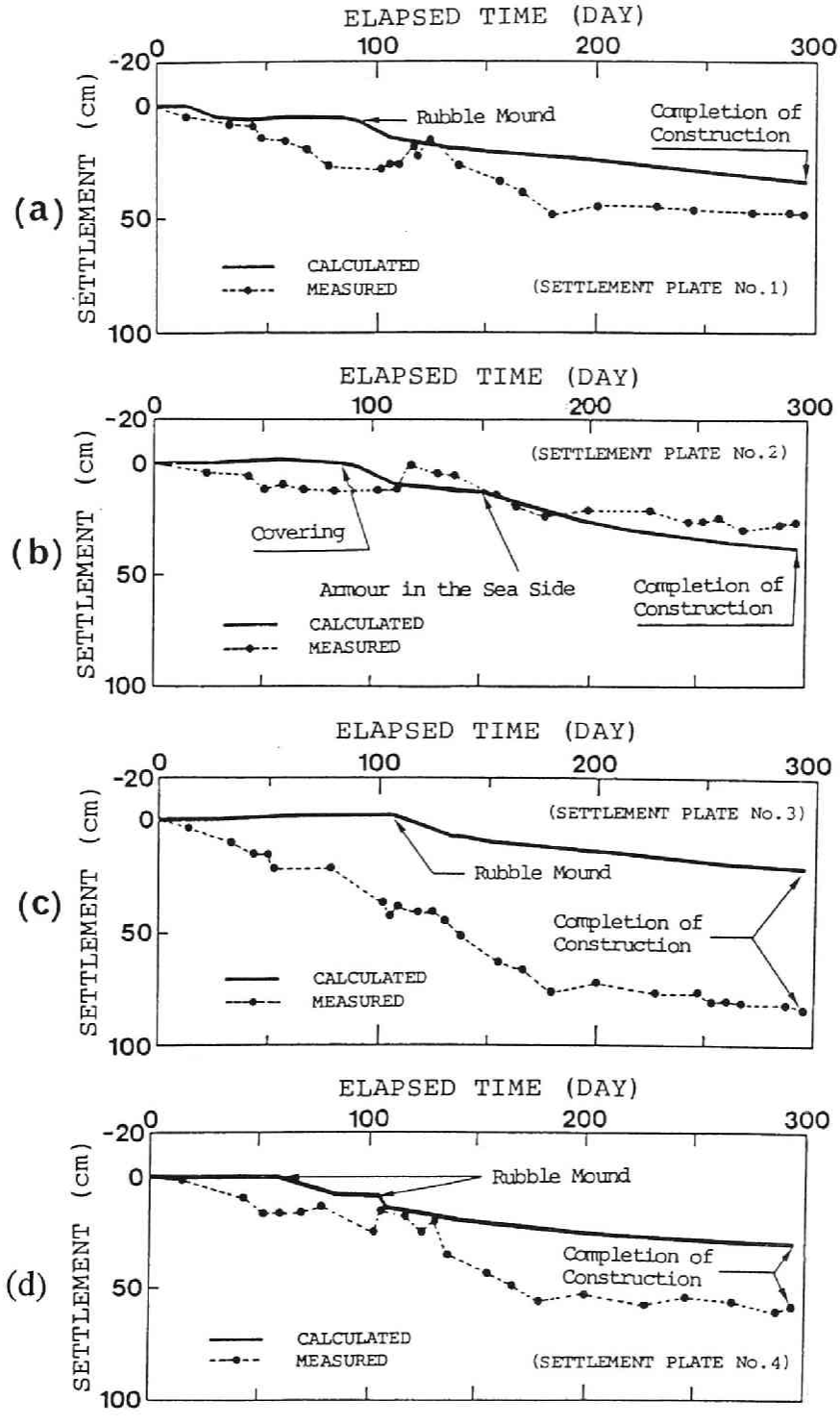

Fig. 23 Time Settlement Performance (Section C); (a) : Settlement Plate No. 1, (b) Settlement Plate No. 2, (c) Settlement Plate No. 3 (d) :Settlement Plate No. 4

avoid being badly affected by waves or tides. Immediate and subsequent settlement occurs due to this localized loading and induced disturbance of the seabed materials, which are almost impossible to evaluate quantitatively by the numerical analysis performed here. According to private communication with the engineer who dealt with the actual construction of the breakwater (Hamada, 1989), some settlement plates were set by excavating the original marine foundation ground and redumping rubble on the seabed to fix them, and others were fixed by dropping rubble after setting them onto the original marine foundation ground without any excavation. Considering these facts and the effects of waves and tides, it is conclude that the calculated performance can well evaluate the actual deformation of a marine foundation subjected to breakwater construction.

9-5-2. Lateral Displacement Profiles with Depth

A comparison of the calculated and monitored lateral displacement profiles with depth for Section B are shown in *Figs. 24 (a)* and *(b)*. In these

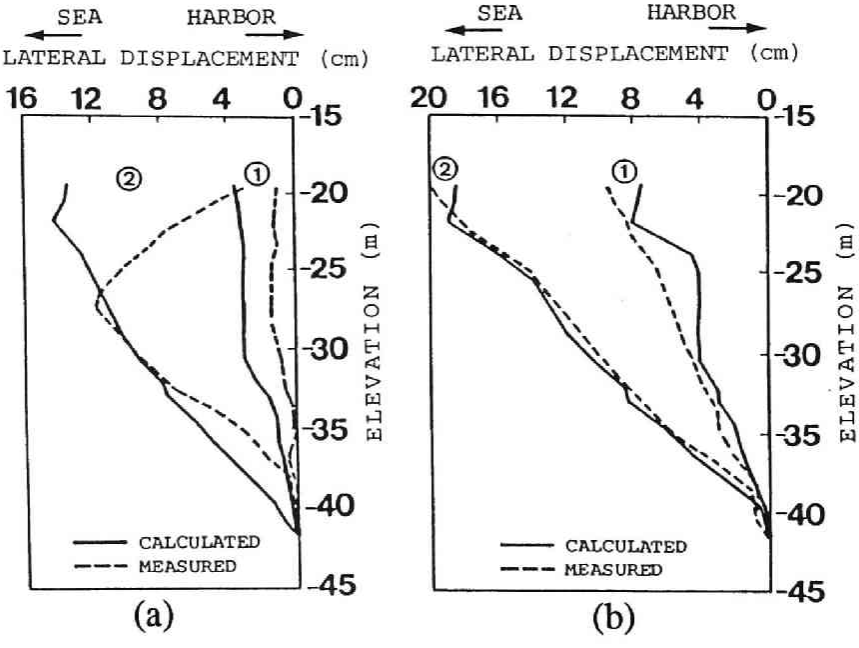

Fig. 24 Profiles of Lateral Displacement with Depth (Section B);
(a) : Inclinometer No. 1, (b) : Inclinometer No. 2,
(1 : Covering, 2 : Completion of Construction)

figures, *1* indicates the time during which the covering on the sea side was constructed and *2* indicates the time when the breakwater construction was completed. The monitored lateral displacement profile measured by *IN1*, 113 meters seaward from the center line of the breakwater, is shown in *Fig. 24 (a)* together with the calculated performance. The calculated performance can evaluate the monitored results at the time the covering was equipped to some extent. However, the shape of the profiles is completely different at the completion of the breakwater construction; that is, the monitored lateral displacement is restrained at the seabed peaking at a depth of *C.D.L.* -27.3 meters, whereas the calculated performance shows a comparatively large lateral displacement at the seabed. In *Fig. 24 (b)*, the calculated and monitored lateral displacement profiles for *IN2*, 55 meters seaward from the center line of the breakwater, both show a good agreement for when the covering was equipped and at the completion of the breakwater construction. A comparison of the calculated and monitored lateral displacement profiles with depth for Section C are show in *Figs. 25 (a), (b)* and *(c)*. In these figures, *1* indicates the time when the rubble

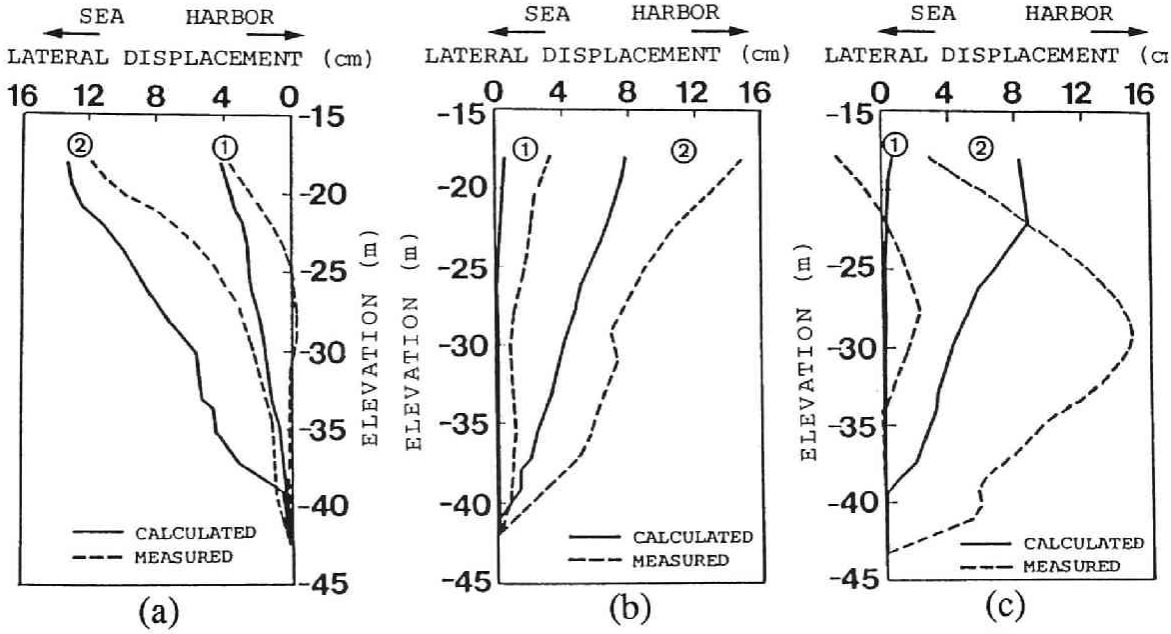

Fig. 25 Profiles of Lateral Displacement with Depth (Section C);
(a) : Inclinometer No. 1, (b) : Inclinometer No. 2,
(c) : Inclinometer No. 3, (1 : Rubble Mound Formation on the Harbor Side, 2 : Completion of Construction)

mound was formed on the harbor side and *2* indicates the time the breakwater construction was completed. As shown in *Figs. 25 (a)* and *(b)*, the calculated performance can qualitatively predict the monitored profiles with a slight overestimation of *IN1* on the sea side, and in contrast, with a slight underestimation of *IN2* on the harbor side. The monitored lateral displacement profile here differs from that of the calculation for *IN3*, 90 meters harbor side from the center line of the breakwater. According to the monitored results, the restriction effect of the rubble mound on the lateral ground movement is stronger than that evaluated by *FEM*. Further studies should be conducted on this restriction effect which also appears in the results for Section B (*Fig. 24 (a)*) in order to clarify the mechanism of lateral ground movement due to offshore construction.

9-5-3. Maximum Settlement - Lateral Displacement Relations

The stability of the marine foundation is investigated in this section, in terms of the maximum settlement-lateral displacement relations proposed by Tominaga and Hashimoto (1974). The maximum settlement measured by *SP2* and the maximum lateral displacement measured by *IN2* in Section B are plotted with the corresponding calculated performance in *Fig. 26*. Firstly, the settlement took place without any lateral displacement. Then, lateral displacement began to occur with subsequent advancement of the settlement, and the degree of settlement to lateral displacement increased as the breakwater construction advanced. This means that the

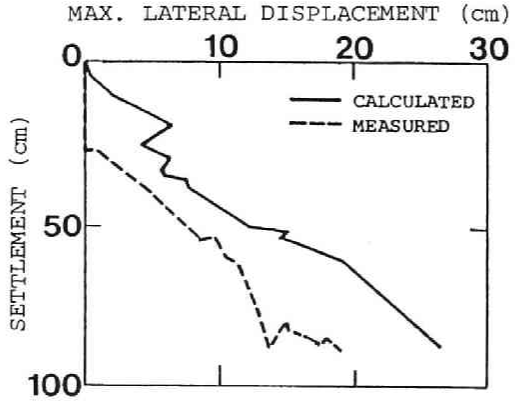

Fig. 26 Settlement Lateral Displacement Performance (Section B)

marine foundation became stable. With these monitored results, we can conclude that the marine foundation ground has safely deformed during the breakwater construction.

Comparing the monitored results with the corresponding calculated performance, the monitored and calculated ratios of the maximum lateral displacement to settlement have come to a good agreement, except in the primary stage when the monitored settlement occurred without any monitored lateral displacement. As explained in a previous section (4-5), the calculated performance confirms the fact that the breakwater foundation has stably deformed without any indication of failure, according to the effective stress paths for the elements of the marine foundation. In *Fig. 26*, the monitored relations show a safer deformation than the calculated ones; that is, the monitored settlement to lateral displacement ratio exceeds that of the calculation. Therefore, the stability of the marine foundation during the breakwater restoration has been confirmed by the strong support the calculated performance provides.

For Section C, the maximum settlement measured by *SP2* and the maximum lateral displacement measured by *IN1* on the sea side are plotted in *Fig. 27 (a)* with the corresponding calculated performance, and the maximum settlement measured by *SP3* and the maximum lateral displacement measured by *IN3* on the harbor side are plotted in *Fig. 27*

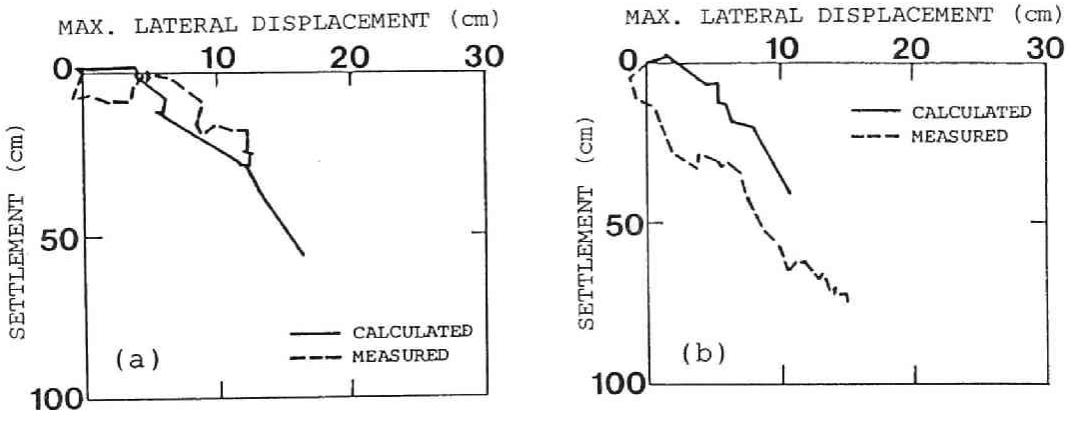

Fig. 27 Settlement Lateral Displacement Performance (Section C);
(a) : Sea Side, (b) : Harbor Side

(b), also with the corresponding calculated performance. In these figures, the stability of the marine foundation in Section C is also confirmed by the calculated performance, in the same way as that for Section B explained above.

9-6. Conclusions

Coupled stress-flow analyses in terms of the elasto-viscoplastic finite element method are performed. The deformation of a marine foundation ground subjected to breakwater construction is numerically investigated, and the calculated results are compared with the monitored settlement and lateral displacements. The following conclusions can then be made:

(1) The calculated settlement of the foundation beneath the caisson due to breakwater construction is controlled by the reinforcement effect of *SCP*, whereas a predominant settlement takes place at the boundary between the reinforced and unreinforced areas.

(2) According to the calculated performance, the excess pore water pressure is almost fully dissipated by a year after the completion of the breakwater construction because of the high permeability of the silt layers. In addition to these results, since the secondary consolidation of silt is not so remarkable, the long-term settlement of this marine foundation will not become a serious issue.

(3) Lateral ground movement mainly occurs due to the setting and filling of the caisson, and to the construction of the armor units with a peak value at the boundary between the sand layer of the seabed and the alluvial silt deposit.

(4) The stability of the marine foundation ground is numerically investigated by the effective stress paths of the silt layers. The stress state of the foundation ground during the breakwater construction is stable and shows no indications of failure.

(5) The calculated performance of the settlement can predict the monitored settlement with a slight tendency toward underestimation, considering the difficulty of measurement. In regards to the lateral ground movement, a difference can be seen in the restriction effect of the sand layers. However, the calculated and monitored results are qualitatively in good agreement.

(6) The monitored maximum settlement-lateral displacement relations confirm the stability of the marine foundation ground during breakwater construction with significant support from the calculated performance.

REFERENCES

(1) Adachi. T., F. Oka and M. Mimura (1985) : Descriptive Accuracy of Several existing Constitutive Models for Normally Consolidated Clays., Proc. 5th ICONMIG, Vol. 1, pp.259-266.

(2) Brunn, P (1985) : Design and Construction of Mounds for Breakwater and Coastal Protection, Elsevier, New York, pp.714-726.

(3) Hamada, T. (1989) : Private Communication.

(4) Ishii. I., F. Ogawa and K. Zen (1984) : Engineering Properties of Marine Clays in Osaka Bay (Part 2) Physical Properties., Consolidation Characteristics and Permeability, Technical Note of the Port and Harbour Research Institute, Ministry of Transport, No. 498, pp.47-86 (in Japanese).

(5) Kitajima, S., T. Nakano, O. Horii, S. Kakizaki, K. Furuhata and Y. Hanaki (1968) : Disasters of Breakwaters by Wave Action, Technical Note of Port and Harbour Research Institute, Ministry of Transport, Japan, No. 58.

(6) Mimura. M. and H. Sekiguchi (1986) : Bearing Capacity and Plastic Flow of Rate-Sensitive Clay under Strip Loading., Bull. of D.P.R.I., Kyoto Univ., Vol. 36, Part 2, pp.99-111.

(7) Sekiguchi. H. (1977) : Rheological Characteristics of Clays., Proc. 9th ICSMFE, Tokyo, Vol. 1, 1977, pp.289-292.

(8) Sekiguchi. H., Y. Nishida and F. Kanai (1982) : A Plane-Strain Viscoplastic Constitutive Model for Clay., Proc. 37th National Conf., JSCE, pp.181-182 (in Japanese).

(9) Sekiguchi. H. (1983) : Application of Plane-Strain Viscoplastic Constitutive Model for Clay., Proc. Annual Conf., Chubu Branch, JSCE, pp.342-343 (in Japanese).

(10) Sekiguchi H., T. Shibata, A. Fujimoto and H. Yamaguchi (1986) : A Macro-Element Approach to Analyzing the Plane-Strain Behaviour of Soft Foundation with Vertical Drains., Proc. 31th Symposium, ICSMFE, pp.111-120 (in Japanese).

(11) Sekiguchi, H., T. Shibata, M. Mimura and K. Sumikura (1988) : Behaviour of the Seawall and Bridge Abutment at the Edge of an Offshore Airport Fill., Annuals of the D.P.R.I., Kyoto Univ., No. 31 B-2, pp.123-145 (in Japanese).

(12) Tsuchida. T., Y. Kikuchi, K. Nakashima and M. Kobayashi (1984) : Engineering Properties of Marine Clays in Osaka Bay (Part 3), Static Characteristics of Shear., Technical Note of the Port and Harbour Research Institute, Ministry of Transport, No. 498, pp.87-114 (in Japanese).

(13) Yoshinaka, R. (1968) : Lateral Coefficient of Subgrade Reaction, Civil Engineering Journal, Vol. 10, No. 1, pp.32-37 (in Japanese).

CHAPTER 10

Conclusions

The major conclusions obtained in Part 2 are summarized as follows:

In chapter 7, a framework of assessing the lateral ground movement is proposed based on the elasto-viscoplastic finite element analysis. Firstly, degree of partial drainage is defined by time factor, in terms of the rate of loading and the rate of consolidation. Secondly, the ratio of the volume gained in lateral deformation to that lost in settlement, V_s/V_p is introduced. Thereafter, it has been shown that the lateral ground movement can be estimated by the time factor, V_s/V_p and the ratio of the width of loading to the thickness of deformed soft clay layer, B/H.

Based on the assessment proposed in this chapter, the load - lateral displacement performances data around the world are gathered for discussion. It is shown that the nature or stratification of the soft soil has clear impact on the deformation behavior, i.e.,that is, deterioration of foundation rigidity is significant for weak soft foundations, consisting of peat or organic clay, on the other hand, for stiff clay foundation, no reduction in the foundation rigidity occurs even during the loading period.

In chapter 8, deformation analysis of reclaimed marine foundation is performed. Koshien reclaimed land has been constructed in this 5 years by dumping sand and gravel. The process of deformation of the marine foundation subjected to this reclamation work is numerically investigated by the coupled stress flow analysis in terms of the elasto-viscoplastic finite element method. Emphasis is placed on the following three factors; (1) geometrical condition of the foundation; (2) material properties of the foundation; and (3) the exact modeling of the construction sequence. Reliable numerical analysis can be performed only when these three factors are satisfactorily modeled. In this chapter, after explaining in detail how to

determine the parameters constitutive model requires, the calculated performance is discussed and the observed settlement, lateral displacement profiles of the foundation and the generation/dissipation process of excess pore water pressure are compared with the calculated results.

The deformation of the marine foundation was calculated by taking into account the effective stress path of clay elements of the foundation. It has been shown that this calculated performance can predict the observed settlement profiles of the seabed and the crest of the diluvial layers and lateral displacement profiles with depth exactly. However, the characteristics of the diluvial clay which usually remains overconsolidated, that is, estimation of plastic yielding (p_c evaluation), secondary compression in overconsolidated region and the generation/dissipation process of excess pore water pressure, should be further investigated.

In chapter 9, deformation of the marine foundation subjected to the breakwater construction is analyzed by the elasto-viscoplastic finite element method. The calculated performance confirm that the stress state of the foundation keeps stable and the reinforcement effect of densely compacted sand (*SCP*) is effective on controlling the settlement of the breakwater foundation. Comparing the calculated performances with the observed settlement and lateral displacement profiles, both results are qualitatively in good agreement, considering the difficulty of direct measurement of deformation in the sea. Finally, it should be emphasized that the monitored maximum settlement - lateral displacement relations confirm the stability of the breakwater foundation at the construction site, with a strong support from the calculated performance.